Universit à degli Studi di Cagliari

DOTTORATO DI RICERCA IN FISICA

FIS/03 FISICA DELLA MATERIA

XXVII CICLO

Characterization and application of Pb-based organometal halide perovskite

PhD student: Feipeng Chen

Coordinator: Prof. Paolo Ruggerone

Tutor: Prof. Michele Saba

Esame finale anno accademico 2013 – 2014

REGIONE AUTONOMA DELLA SARDEGNA

Abstract

In the foreseeable future, the global energy consumption is expected to increase significantly. Solar energy, as an alternative form of energy, has gained popularity as a way to solve the greenhouse gas emission and sustainability problem of fossil fuels. This thesis mainly concerns a novel materials system, namely organometal trihalide perovskite, that is currently receiving considerable attention as light absorber in solar cells, due to the promise to obtain significant improvements in the efficiency of solar cells fabricated with very low cost, scalable techniques. The main idea of this thesis is to study the photophysical properties and the mechanisms affecting the performance of solar cells.

In chapter 1, the history of solar cell materials will be reviewed briefly.

The synthesis and basic characterization are described in chapter 2. In this chapter, it is explained how the methylammonium iodide was synthesized and purified. Perovskite films were fabricated by three different methods, resulting in very different film morphologies. Perovskite structure was confirmed by X-ray diffraction, and $CH_3NH_3PbI_3$ shows a tetragonal phase with lattice parameters a=b=8.872 Å and c =12.637 Å. The morphology investigation shows that solution spin-casting method produces needle-shaped crystals, leading to a partial surface coverage and limited conductivity. The two-step from solution method was based on spin-casting PbI_2 and CH_3NH_3I solution gradually, creating the perovskite upon reaction of the two compounds. The result is a film with smaller grains and more uniform coverage. Finally, the vapour assisted method, where a PbI_2 film is first obtained by spin-casting from solution, then evaporation of CH_3NH_3I occurs for several hours in N_2 atmosphere. A uniform film was achieved by this method with RMS roughness around 38 nm.

The optical properties of the $CH_3NH_3PbI_3$ are investigated in chapter 3. The optical bandgap of it is 1.64 eV, as extracted from the absorption edge, which is higher than the theoretical 1.55 eV. The absorption coefficient exceeds ~10^5 cm^{-1} for incident light wavelength shorter than 500 nm. The transient photoluminescence

spectroscopy analysis shows that the lifetime of the excitons could be as high as τ = 80 ns under low excitation conditions. As long as the film is processed in such a way that the mean PL lifetime exceeds several nanoseconds at sun illumination, carrier mobility is sufficiently high to guarantee efficient charge collection in the photovoltaic device.

In chapter 4, simple planar solar cells are described, which have been fabricated with compact TiO_2 as electron transport layer, covered with perovskite as light harvester; poly (3-hexylthiophene- 2,5-diyl) (P3HT) was spin-casted as hole transport layer; at last, transition metal oxide MoO_3 or LiF was evaporated onto P3HT as interfacial modifying material, final electrode was a thin layer of Ag. The relationship between TiO_2 morphology and the solar cell performance is discussed. The morphology of compact TiO_2 appears to be an important factor to influence the photovoltaic, which still needs further understanding in order to obtain better performing devices.

The investigation on perovskite morphology indicates that the vapour assisted two-step deposition technique is useful for preparing perovskite films. We rationalize the crystal growth process with the conjecture that the organic and inorganic components have an efficient reaction by vapour intercalation into the PbI_2 film. The resulting film has full surface coverage, microscale grain size and uniform grain structure.

The investigation on interfacial modification shows that the solar cell with MoO_3 as modification material has excellent performance with a PCE of 7.95%. And the solar cell with LiF as modification material has good performance with a J_{sc} of 21.73 mA/cm^2. Both of the two materials have positive affection to the solar cell. The MoO_3 is a proper material for modifying the interface between the electrode and hole transporting layer, which could replace the ITO in a heterojunction solar cell. And the LiF could decrease the work function of the metal contact, which may increase the transporting ability and increase the compatibility of the metal electrode. The investigation implies that the interface engineering is very important to the device science.

Keywords: Perovskite, $CH_3NH_3PbI_3$, organometal halide perovskite, planar solar cells, surface modification

Contents

Acknowledgement

CHAPTER 1
Introduction

The organometal trihalide perovskite as light absorber in solar cells has amazed everyone by obtaining in a short time span significant improvements in power conversion efficiency (PCE). It receives special attention in the scientific community and industry because of the low-cost, it is easy to fabricate and has high PCE. Since the first trying on a sensitized solar cell based on perovskite nanocrystalline particles self-organized on TiO_2 as n-type semiconductors in 2009, the PCE of perovskite-based solar cells has rapidly improved from 3.8% to 20.1% (certified by NREL) over the past 6 years. Few solar technologies have ever improved so much, and none has done it so fast.

In this thesis, the history of the perovskites for application and the landmark achievements are mentioned briefly. I will focus on my efforts to engineer the fabrication process for organo-lead trihalide perovskites as light harvesters in solar cells, and the measurement of their basic properties, including crystal structure, photophysical properties and morphology modifications. Concerning requirements for high-efficiency photovoltaics, the electron and hole transport materials are discussed, as well as some questions and challenges facing the further development and commercialization.

1.1 Basic materials

The world's growing population and industrialization result in a continuously increasing demand for energy. Taking into account the consequences of climate change linked to the consumption of fossil fuels to meet our energy demand, it is difficult to accept the current portfolio of energy sources. On the other hand, the fossil fuels on earth cannot satisfy the demand for energy in some years later. This poses us with a critical question, how could we solve the challenging problem of developing alternative sources of energy which could replace fossil fuels. Among renewable energy resources, solar energy is by far the secure, clean, sustainable and the most abundant energy resource; harvesting just a small fraction of available solar energy would be enough to indefinitely satisfy the world's entire energy demand [1].

If solar energy is to be a major primary energy source, it must be collected and converted to an easy and widely using energy style to meet the demands for the daily life or the manufacturing industry. Photovoltaics could be chosen to meet the need for abundant electricity, generating at competitive costs, whilst conserving resources for future generations, and having environmental impacts lower than those of alternative future energy options.

1.1.1 Inorganic materials used for photovoltaics

Organic materials offer strong potential for cost reduction with respect to conventional solar cells, but their spectrally limited absorption and low carrier mobilities limit their application on achieving commercially viable device efficiencies [2]. However, not only the organic material could realize the cost reductions, but also some new inorganic materials for photovoltaic devices could compete with traditionally generated power with lower production cost.

There are a large number of inorganic materials used as solar absorber and device architectures, but at this time crystalline and multicrystalline silicon solar cells dominate the market. The thin-film devices based on amorphous silicon (a-Si), $Cu(In,Ga)Se_{2-x}S_x$ (CIGS), or cadmium telluride (CdTe) are beginning to emerge in the

market [3]. Colloidal inorganic nanocrystals based on the new or conventional materials are emerging in the past decade, which share all of the primary advantages of inorganic materials, at the same time, providing controlled synthesis, an ability to be processed in solution, and a decreased sensitivity to substitutional doping, while retaining the broadband absorption and superior transport properties of traditional photovoltaic (PV) semiconductors [4-6].

1.1.1.1 Silicon based materials

Single crystal silicon

Currently most of the commercial solar cells are made from silicon. The advantage of silicon is the mature fabricating technology, the large abundance in the earth, and the non-toxicity that is an important consideration from the environmental perspective. Silicon based solar cell is one of the earliest solar cells. The band gap of Si is 1.11 eV, which is close to the optimal bandgap of ~1.3 eV for maximum photoconversion efficiency of 33% in a single-junction solar cell, as set forth by Shockley and Queisser [7, 8]. The first silicon solar cell was reported in 1941 and had less than 1% energy conversion efficiency [9]. And then cell efficiency increased rapidly with a structure of diffused junctions. Bell Laboratories fabricated a cell with 4.5% efficiency in 1953 [10] and 6% in 1954 [11]. The 10% efficiency mark was exceeded within 18 months. Since the first silicon solar cell was reported in 1941 [9], there have been substantial improvements in silicon cell performance, obtaining the highest PCE of the 25 % certified in the last year by NREL. In the recent years, the improvement of the single crystal silicon solar cell is slow, as the performance of the solar cell was already 24% in 1996 [12]. The best performing research cell was based upon high efficiency passivated emitter, rear locally-diffused (PERL) cells, and resulted in a considerable improvement in the energy conversion efficiencies of silicon solar cells up to 24.0% under the standard global solar spectrum. Figure 1.1 shows the PERL solar cell with a double layer antireflection (DLAR) coating.

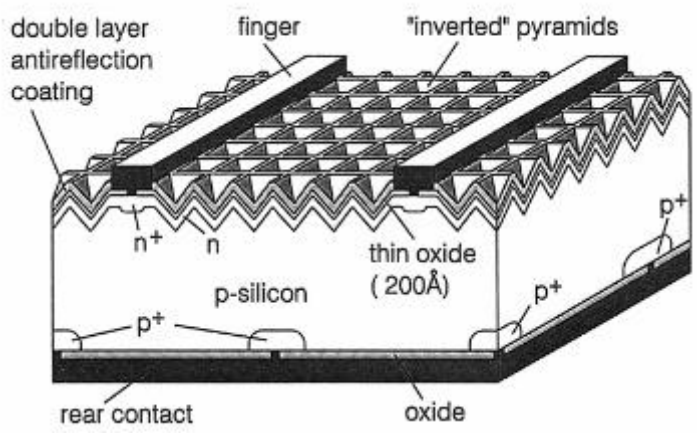

Figure 1.1| *The passivated emitter, rear locally-diffused (PERL) cell with a double layer antireflection coating [12].*

The ZnS and MgF_2 DLAR coating evaporated onto the cells processed with the "annealed" thin oxide improved the PCE to 24.0% from 23.5% which was without DLAR.

In the later 10 years, the performance of a silicon solar cell was kept on the same level that was around 24.5%. The new certified PCE of 25.0% was reported by NREL last year; with the solar cell structure the same as 10 years ago.

Multicrystalline silicon

Although the efficiency of the single crystal is high, the cost of it is too significant to realize widespread application; multicrystalline silicon (mc-silicon) has instead a wider use than single crystal silicon because of cost reduction potential [13]. The solar conversion efficiencies of commercial mc-cells were typically in the range of 12–15% and up to 17% had been obtained by more sophisticated solar cell designs [14]. The potential of mc-silicon was even higher; about 19.8% had been demonstrated for laboratory cells in 1998 [15]. And then, a higher efficiency of 20.4% was certificated by NREL in 2004. Such an improvement of the efficiency greatly increased the commercial viability of multicrystalline silicon.

Amorphous silicon

To decrease the cost of the silicon industry even more and realize the application of the silicon devices, scientists never gave up the research on silicon. Amorphous silicon based solar cell which is the non-crystalline form of silicon, is another way to utilize silicon in electronic devices. It can be deposited in thin films at low temperature onto a variety of substrates and offers some unique properties of silicon. 30% of the cost of the conventional silicon device is about the sawing process because of the special and expensive saw material. The solution processes for the fabrication of electronic devices have received considerable attention for a wide range of applications. Comparing to the conventional vacuum processes and vapour-phase deposition, solution techniques will reduce a big amount of processing costs.

In the early stage, amorphous Si solar cells were generally produced by vacuum deposition methods using silane as a precursor [16]. Later research works, the solution-phase analogue generating methods replaced the vacuum deposition techniques. Hydrogenated polysilanes, including straight- chain Si_nH_{2n+2} or cyclic Si_nH_{2n} forms, are used as the precursor. These materials are difficult to work with because of oxygen sensitivity. The hydrogen-rich polysilanes were synthesized with organic functional groups protecting, which can impart solubility or facilitate polymerization, leading to higher-order molecular substructures of crystalline Si [17]. Spin-coated films from liquid Si ink were prepared at various temperatures, by which the amount of hydrogen in a final layer could be controlled. Masahiro Furusawa et al. demonstrated the solution processing of silicon thin film transistors (TFTs) using a silane-based liquid precursor. Using this precursor, they have prepared polycrystalline silicon (poly-Si) films at 300 Celsius, by both spin-coating and ink-jet printing. The polycrystalline Si film prepared by this method had 300 μm grains in size and mobility as high as 108 cm^2/Vs [18]. Cyclohexasilane was also utilized as a precursor for liquid-Si ink for the fabrication of p-n junction diodes and field effect transistors. The films were treated at 350 ℃ to form a polycrystalline Si and shown a low turn-on voltage FET [19].

In addition to the silicon based solar cells, new inorganic materials as light

harvesters are emerging in the recent years.

1.1.1.2 Non-silicon based materials

Among newly adopted inorganic materials for solar cells, GaAs, CdTe and CIGS have attracted more attention than other materials, such as ZnTe, PbSe, InP, ZnSe, WSe_2, Bi_2S_3, Ag_2S, and FeS_2 et al. Some of these materials are environmentally friendly, and some are not. The need for panchromatic absorption, covering at least all visible part of solar spectrum, puts strict requirements on the upper bound for bandgap energy. On the other side, too low of a bandgap sacrifices the open circuit voltage, with the best compromise to be found around ~1.3 eV. On the other hand, other main standards to evaluate the materials are environmentally “green” and “abundant” in the earth, such as Cu_2ZnSnS_4 and FeS_2, which would go a long way toward diminishing concerns about the long-term fate of solar modules.

It is clear that more materials would come out adding to the inorganic material family for solar energy.

Copper Indium (Gallium) Sulfide and Selenide

Cu(In, GA)$Se_{2-x}S_x$ (CIGS) has one of the highest confirmed efficiencies for single-junction polycrystalline devices. Vacuum-based deposition technique is necessary for preparing high efficiency devices. The typically devices are achieved by either co-evaporation of the constituent elements [20, 21] or sequential processes employing stacked combinations of metal, chalcogenide, and chalcogen precursors deposited by sputtering or thermal evaporation [22, 23].

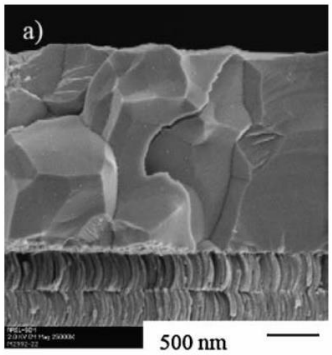

Figure 1.2| *The SEM cross section of the CIGS solar cell [22].*

$Cu(In_{1-x}Ga_x)Se_2$ (CIGS)-based solar cells were prepared by Repins et al. [20], and efficiencies as high as 19.9% have been reported, which is comparable to those in crystalline Si solar cells. The device structure is: soda-lime glass (SLG) substrate, sputtered Mo back contact, three-stage co-evaporated CIGS, chemical-bath-deposited (CBD) CdS, sputtered resistive/conductive ZnO bi-layer, e-beam- evaporated Ni/Al grids, MgF_2 anti-reflective coating, and photolithographic device isolation. Figure 1.2 shows the SEM cross section of the CIGS crystal. It indicates the CIGS crystal has a big grain shape. The authors believed that the high efficiency was from an effective surface modification. It is not difficult to understand why the CIGS based photovoltaic is charming for manufacturers and researchers. The good stability and the promise high efficiencies for thin-film solar modules make CIGS very appealing.

Now the efficiency of the CIGS was certified to be 21.7% by NREL last year, which makes the CIGS more attractive for the commercial industry.

Cadmium Telluride

CdTe photovoltaic is a technology based on CdTe thin film as light absorber and converting solar energy to electricity. Thin film CdTe is generally a p-type absorber, with a direct bandgap of 1.45 eV which is closer to the optimal 1.3 eV than Si; and its absorption coefficient is $>10^5$ cm^{-1}, much better than Si (in Si solar cell more than 100 m of active material thickness is required to absorb all the light from the sun) [24]. CdTe PV is the only thin film technology with lower costs than conventional solar

cells made of crystalline silicon.

In 1997, T. Aramoto et al. [25] reported a CdTe solar cell with ultrathin CdS and thin CdTe film with 16.0% efficiency. They report a new technique to prepare the solar cell: CdS was deposited by metal organic chemical vapour deposition (MOCVD), while CdTe was deposited by close-spaced sublimation (CSS), which is a low-temperature, low-cost technique. This work took a perspective to the manufactures that provide a low-cost fabricating method but high efficiency. Commonly, the performance of CdTe thin-film devices is enhanced by treating the CdTe layer with $CdCl_2$ followed by annealing at 400 ℃ in air. The results show that $CdCl_2$ treatment enhances the recrystallization and diffusion processes, leading to a compositional variation within the CdTe layer due to diffusion of sulphur from the CdS. The highest sulphur concentrations observed after 30 min treatments with $CdCl_2$ at 415 ℃ are near the solubility limit for sulphur in CdTe [26].

In the later years, First Solar and GE Global Research were devoting efforts to increase the CdTe solar cells and reduce the cost of the fabrication. A 21.5% high efficiency was achieved by First Solar Company from a CdTe solar cell.

CdSe as a relative of CdTe was famous in the CdSe nanoparticles with sizes below 100 nm exhibit a property known as quantum confinement. CdSe quantum dot is a promising semiconductor material for electronics. Although the CdSe quantum dot based solar cell is bad in efficiency (~2%) [27, 28], but the light absorption in 400-800 nm is around 90%, which means that it has a potential to apply in tandem solar cell.

Iron disulphide

Pyrite FeS_2 is composed of earth abundant Fe and S. And its band gap is only 0.95 eV and absorption coefficient is 10^5 cm^{-1}, meaning it should absorb the light effectively. The absorption coefficient of FeS_2 is particularly outstanding because only 40 nm of pyrite could absorb 90% of incident light. In spite of intricate problems existing within material, high quantum efficiencies for photo current generation (> 90%) and photovoltages (V_{oc}= 500 mV) have been observed with single crystal

electrodes and thin layers respectively. With the electrolyte 4 M HI/0.05 M I_2/2 M CaI_2, a PCE measurement produced a slightly higher efficiency of 2.8%. The low reported efficiencies may be due to the fact that high quality thin films of FeS_2 pyrite have been difficult to produce regardless of the deposition method selected [29]. Significant research challenges are discussed in the hope of attracting interest in the development of solar cells from this abundant material.

Song et al. [30] reported a FeS_2 nanowire by thermal evaporating the pyrite on a steel foil. The pyrite nanowires have lengths greater than 2 μm and diameters of 4-10 nm. These crystals show a highly p-doped property with carrier concentrations on the order of 10^{21} cm^{-3}. This report show a new way to utilize the FeS_2 towards solar energy conversion.

Gallium arsenide

Gallium arsenide (GaAs) is a widely known semiconductor used in the manufacturing of electronic devices, such as infrared light-emitting diodes, laser diodes and solar cells. The bandgap of the GaAs is 1.42 eV, which is suitable for an absorber in solar cells. The absorption coefficient of GaAs is much higher than Si, leading to only a few micrometres of thickness needed to absorb all of the light. On the other hand, the mobility of GaAs is comparable to Si, which allows the charge carriers transporting in the GaAs film/crystal.

Stirn and Yeh [31] reported a 15% solar cell with Au on top of GaAs as light absorber in 1975. The processing steps were amenable to the use of low-cost polycrystalline films of GaAs, whilst the single crystal was used in this solar cell. More than 30 years later, Bauhuis et al. [32] reported a thin film GaAs solar cell with 26.1% efficiency. A low-temperature annealing front contact and the thin film metal mirror on backside are optimized. In addition to an improved active layer material quality, grid mask and anti-reflection coating this leads to thin-film cells as good as cells on a substrate, with record efficiencies for single junction GaAs solar cells of 26.1% for both cell types.

In 2010, FhG-ISE reported an efficiency of 26.4% solar cell with single crystal

GaAs and 2012 Alta Devices reported a 28.8% solar cell with thin film technique, which are certified by NREL. All the reports show that GaAs is an important material in solar energy applications.

Besides the CdTe, FeS_2 ,CIGS and GaAs, there are lots of other solar energy conversion materials, such as Cu_2S [33], with a PCE higher than 9%; Cu_2O with a Schottky device PCE of 1.76% [34]; Copper Zinc Tin Sulphide and Selenide (CZTS) with a high absorption coefficient greater than 10^4 cm^{-3} and PCE of 6.7% for the S analogues [35]. Colloidal CZTS nanocrystals were designed by Korgel et al. [36] for a solar cell realized with solution deposition. Although the efficiency is only 3.1%, they show us a new, promising technology.

1.1.2 Organic materials used for photovoltaics

Attempting to harness solar energy as a source to produce electricity is one of the most promising ways among the solar energy applications. Although the present dominant photovoltaic (PV) technology is based on inorganic materials, (for instance, Si, GaAs, CIGS, CdTe et al.), the cost of these conventional devices is too high for the technology to be scaled up quickly. Intensive research has been done towards obtaining a high performance with low-cost photovoltaic technologies. Among the numerous topics investigated, organic photovoltaic (OPV) devices are one of the most promising. OPV devices are based on organic semiconductors - carbon-based materials whose backbones are comprised mainly of alternating C-C and C=C bonds. Electron delocalization along the conjugated backbone is responsible for the semiconducting properties of OPV devices [37]. One of the major differences between organic semiconductors and inorganic semiconductors is the presence of tightly bound excitons (electron-hole pairs) resulting from their low dielectric constant ($\varepsilon_r \approx 2$-4) and large effective masses. The binding energy of the Frenkel exciton is in the range of 0.3-1 eV [38]. The weak intermolecular van de Waals interaction enables the realization of low-cost, large-area deposition technologies such as roll-to-roll printing. In recent years, organic electronic devices such as organic

light-emitting diodes (OLEDs), organic thin film transistors, OPVs and organic memory devices have attracted considerable attention, owing to their potential low cost and high performance characteristics. OLED displays have gained a considerable share in the portable electronics market, or use in devices such as smart phones.

Organic semiconductors could be divided into two different categories according to the molecule unit size, which we can call them small molecules and polymers. These two types of materials are different in terms of the synthesis, and device processing techniques.

1.1.2.1 Polymers

The polymer technology for solar energy is improving slowly. Figure 1.3 shows some famous representative polymer materials. One of the earliest famous material is poly[2-methoxy-5- (2'-ethylhexyloxy)-p-phenylene vinylene] (MEH-PPV), which was designed by Wudl et al. [39]. Wudl also designed one of the most important fullerene derivatives, PCBM [40], which is employed as an acceptor in organic solar cells. The MEH-PPV based solar cells reach a PCE higher than 3.0% after significant optimization with a $PC_{70}BM$ [41]. However, the low hole mobility and narrow light absorption range limited the improvement in solar cell. At that time, polythiophenes were considered promising towards solving the problem about the hole mobility. Especially, poly(3-hexylthiphene) (P3HT) is the most widely used among polythiophenes [42]. After morphology optimization and phase separation between P3HT and PCBM, high PCEs of 4.4% [43] and 5% [44] were achieved. The good performance is due to the broader spectrum coverage and high hole mobility of the P3HT. after the designing of P3HT, poly[2,6-(4,4-bis-(2-ethylhexyl)-4H-cyclopenta[2, 1-b;3,4-b']dithiophene)-alt-4,7-(2,1,3-benzothi-adiazole)] (PCPDTBT) with low-bandgap was found. The low-bandgap polymer is a desirable feature, as it ensures better absorption of solar light. The solar cells based on PCPDTBT obtained a PCE of 3% [45]. In 2009, researchers fabricated a solar cell with poly[N-9''-hepta-decanyl-2,7-carbazole-alt-5,5-(4',7'-di-2-thienyl-2',1',3'-benzothiadiazole)] (PCDTBT) as light absorber, incorporating a titanium oxide (TiO_x) layer as an optical spacer,

realized a PCE of 6.1% [46].

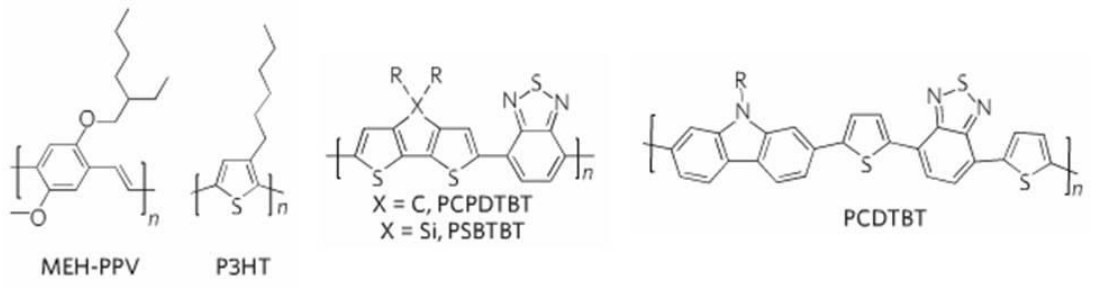

Figure 1.3| *Chemical structures of polymer used in solar cells.*

1.1.2.2 Small molecules

The solar cells based on small molecules have been investigated for a long time. But the landmark work on organic photovoltaics took a major step forward with the results of Tang at Kodak [47].

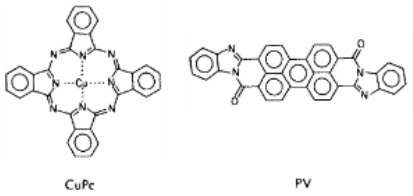

Figure 1.4| *CuPc and PV in Tang's solar cell. [47]*

Figure 1.4 shows the two materials in Tang's solar cell. He designed a solar cell with two organic materials with dissimilar electronic properties, named donor and acceptor. Using this structure, the photogenerated excitons could be separated easily at the interface between two organic materials. The solar cell achieved an efficiency of 1% at AM2 (75mW cm^{-2}) illumination. After his enlightening work on the small molecule solar cell, the donor-acceptor (D-A) heterojunction has become an important structure in organic solar cells. With this structure, only excitons generated close to the interface between both materials were generating free charge carriers. It means that increasing the thickness of the active layer will not increase PCE but lead to a reduction.

A small molecule named phthalocyanine (H_2Pc) was synthesized in 1991 by

Hiramoto et al. [48]. They designed a three layers solar cell with H_2Pc as donor and perylene tetracarboxylic derivative (Me-PTC) as acceptor, in which they co-evaporated a mixed layer of donor and acceptor between the pure H_2Pc and me-PTC layers. The PCE of this solar cell only got 0.7% under 100 mw cm^{-2} illumination.

After this work, the improvement on small molecule solar cell goes slowly. An important improvement about the device structure was the addition of an exciton blocking layer (EBL) between the electron acceptor and electrode. At first, this layer was bathocuproine (BCP) [49]. The EBL concept took the hole- and electron-blocking layers in the later solar cells.

Most of the small molecule solar cells are based on evaporation techniques, because the crystalline property of the small molecules, which always produces a non-homogeneous morphology. Liu et al. [50] reported a conjugated small molecule (SMPV1, shown in figure 1.5) for high performance solution processed organic solar cells. They realized a single junction solar cell based on SMPV1 exhibited a PCE of 8.02% under AM 1.5G irradiation. And a homo-tandem solar cell was constructed with a novel interlayer, reaching an unprecedented PCE of 10.1%. This indicates small molecule materials could be effective candidates for solar energy.

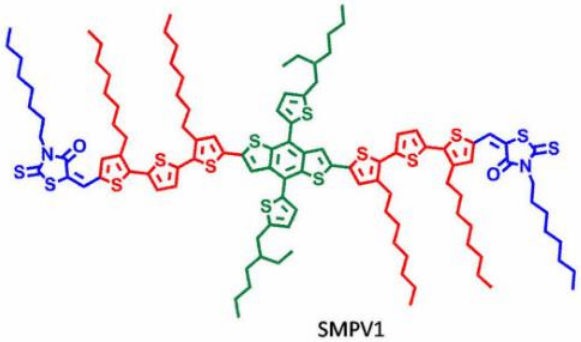

Figure 1.5| *Molecular structure of SMPV1* [50].

1.1.3 Hybrid materials solar cell

To combine the advantages of the inorganic and organic materials, the hybrid

structure was designed for solar cells. The main principle of the combination is taking advantage of one material to compensate the disadvantage of another one. For example, hybrid solar cells based on inorganic NCs and conjugated polymers have the advantages of being morphologically more stable and being able to utilize the high electron mobility of the inorganic phase to overcome charge-transport limitations associated with the organic materials.

Lin et al. [51] reported a hybrid solar cell based on Si nanowires (SiNWs) and poly(3,4-ethylenedioxythio-phene):poly(styrenesulfonate) (PEDOT:PSS), with efficiency of 8.4%. The Silicon nanowire has an anti-reflection property, which could be used in solar cell without needing a coating. And it is easy to realize Si-nanowire-array core-sheath p–n junction solar cells, although with resulting low efficiency. The low efficiency may be from the surface defects made by wet etching and later sandwiched inside the p–n junction, leading to most of the carriers are trapped by depletion defects and cannot be transported out of the device [52]. The hybrid structure composed of Si nanowire and PEDOT:PSS was solved this problem: PEDOT:PSS water solution can infiltrate into the space between SiNWs; the defects made by etching can then be passivated in this way, so the carriers will recombine less at the junction.

There are more hybrid solar cell in recent years, such as the hybrid solar cell with nanocrystalline ZnO and poly[2-methoxy-5-(3’,7’-dimethyloctyloxy)-1,4-phenylenevinylene] (MDMO-PPV) [53] shows the efficiency of 1.6%; mono-aniline-capped poly[(4,4′-bis(2-ethylhexyl)-dithieno[3,2-b:2′,3′-d]silole)-2,6-diyl-alt-(2,1,3-benzothiadiazole)-4,7-diyl] (PSBTBT-NH2) as a donor (D) and cadmium telluride (CdTe) NCs comprising a tetrapod or nanorod-shape as an acceptor, shows PCE of 3.2% [54].

In general, there are lots of papers about the hybrid solar cells. Although the efficiencies are still low until now, the future of the hybrid solar cell is full of hope.

1.2 Organometal perovskite:

1.2.1 Perovskite structure

Perovskite has first used as a name of a mineral composed of calcium titanate, with the chemical formula of $CaTiO_3$. The calcium titanium oxide mineral was discovered in the Ural Mountains of Russia by Gustav Rose in 1839 and is named after the Russian mineralogist Lev Perovski [55]. And then, the mineralogist use perovskite to describe the crystals with the same structure as $CaTiO_3$. To express this kind of structure in a general way, the formula ABX_3 is deployed. In this structure, A and B are cations; X is the anion. And they have the valence value ratio as 1:2:1. Figure 1.6 shows a cubic structure of a conventional perovskite with ABO_3 (cation A is larger than B) composition. In these perovskites which are always used for ferromagnetic application, the A-site is a divalent metal A^{2+} cation (such as Mg^{2+}, Ca^{2+}, Sr^{2+}, Ba^{2+}, Pb^{2+}) in the centre of the lattice unit, the B-site is a B^{4+} cation (such as Ti^{4+}, Si^{4+}, Mn^{4+}, Fe^{4+}) around the A cations, and locates in the centre of oxygen anions O^{2-}. In addition, some carbides, nitrides, halides, and hydrides also crystallize in this structure.

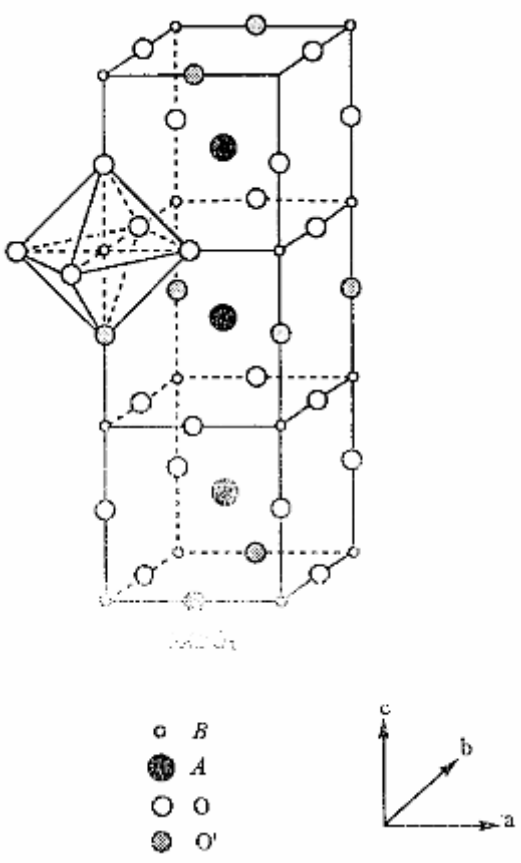

Figure 1.6| *ABO_3 ideal perovskite structure shows oxygen octahedron containing the B ion linked through corners to form a tridimensional cubic lattice. [56]*

To keep the perovskite cubic structure stable, the size of the three ions is strictly confined by the tolerance factor [57] (Formula 1.1):

$$t = \frac{R_B + R_X}{\sqrt{2}(R_A + R_X)} \quad (1.1)$$

where R_A, R_B and R_X are the ionic radii of A, B and X site elements, respectively. The formula is applicable at room temperature to the empirical ionic radii. The ideal cubic perovskite structure appears in a few cases for *t*-value very close to unity 1, in most cases, different distortions of the perovskite structure appear (0.75<t<1). The physical properties of the perovskites depend crucially on the details of these distortions, particularly the electronic, magnetic and dielectric properties, which are very

important for many of the applications of perovskite material.

1.2.2 Pb-, Sn- based trihalide perovskite

The first reports of halide perovskite were $CsPbCl_3$ and $CsPbBr_3$ by Wells in 1893 [58]. At the same time, $KPbCl_3$ and$KPbBr_3$ were synthesized, together with some similar variations, but with few published characterization data. C. K. Moller found $CsPbCl_3$ and $CsPbBr_3$ had the perovskite structure [59]. And he found the $CsPCl_3$ had a maximum spectral sensitivity in the violet, $CsPbBr_3$ in the blue to green region and $CsPbI_3$ in the red region [60]. Recently, Kovalenko et al. reported nanocrystals of $CsPbX_3$ perovskite showed bright emission with wide colour gamut [61].

After the $CsPbX_3$ reported, $CsSnX_3$ (X=Cl, Br and I) was reported in 1920s [62]. But the structural and phase equilibria studies were held in late 1950s [63]. Scaife et al. [64] reported synthesis methods for caesium tin trihalides via aqueous solution and from the melts of anhydrous halides, which ensure freedom from oxidation and effects of traces of water. The $CsSbBr_3$ showed a tetragonally distorted structure at low temperature (12 ℃), and $CsSnI_3$ presents an orthorhombic form in the low temperature. Only the $CsSnBr_3$ showed a 20 ohm-cm room temperature resistivity as a p-type conductor.

Weber reported the organic group methylammonium ($CH_3NH_3^+$) as the A site cation, and Sn based trihalide perovskites [65]. He reported that the $CH_3NH_3SnBr_xI_{3-x}$ (x=0-3) had cubic structure with the unit cell parameters a= 5.89Å (x=3), a= 6.01 Å (x=2) and a = 6.24 Å (x=0). The perovskites showed intense colour and conducting properties. Very soon later, he reported the organic Pb-based trihalide perovskites [66], which have gained spectacular success in solar cell applications since. The structure information were detailed investigated on $CH_3NH_3PbX_3$ (X=Cl, Br and I), which were a=5.68 Å (X=Cl), a=5.92 Å (X=Br) and a=6.27 Å (X=I).

According to the recent research, halide perovskite (AMX_3) can easily tune the bandgap by varying the combination of all the three cationic and anionic components

[67, 68].

1.2.3 New organic group perovskite

Borriello et al. [69] reported that the A cation does not play a major role in determining the band structure but acts to make charge compensation within the lattice. But the calculation results showed that the stability against the distortion of the perovskite cage strongly depends on the embedded cation. The electronic properties can be tuned by affecting the B-X bond length which has been demonstrated to be important to determine the bandgap [70].

Besides the methylammonium, the simplest organic cation used at A site may be CH_4^+. The CH_4CdCl_3 was report by Wyckoff in 1960s. Then the formamidinium ($NH_2CH=NH_2^+$) [71] and tris(dimethylammonium) $(NH_2(CH_3)_2)^+$ cations [72] are used as perovskite elements at A site. $NH_2C(I)=NH_2$ was used to synthesize organic-inorganic compound which was not a perovskite but with a crystal structure[73].

In addition, the BH_4^- can be used to replace the halide element in the perovskite. The $CsMg(BH_4)_3$, $RbCa(BH_4)_3$, $KYb(BH_4)_3$ and $CsEu(BH_4)_3$ were investigated. [68].

1.3 Perovskite solar cells

1.3.1 Basic device structures and performance

There was no report relating halide perovskite materials to solar absorbers until 1980 [74], when Salau reported a new alloy PbI_2: KI ($KPbI_3$, potassium lead iodate) having a direct band gap (between 1.4 and 2.2 eV) that matches the solar spectrum. Assuming Schoiject's proposition [75] on the requirements of new materials for solar cells, the potential use of $KPbI_3$ as a new solar cell material with an optimum theoretical efficiency and operating temperature are 36% and 220, respectively [76].

Liquid dye sensitized solar cell

In the early of 2009, organometal halide perovskites were first applied on

visible-light sensitizers in photoelectrochemical cells [77]. In this report, Miyasaka et al. performed the solar cells based on mesoporous TiO_2 photoanodes that were sensitized with $CH_3NH_3PbX_3$ (X=I, Br) nanocrystalline particles. However, the resulting power conversion efficiencies (PCEs) were not brilliant (η=3.81% for the triiodide and 3.13% for the tribromide), and the cell stabilities were poor in a liquid electrolyte conjurations. Subsequently, in 2011 Park et al. fabricated again liquid dye sensitized solar cells (DSSCs) using 2–3 nm $CH_3NH_3PbI_3$ ($MAPbI_3$) nanocrystals with iodide redox shuttle and bumped up the conversion efficiency of the triiodide cell to 6.54% at 1 sun illumination [78].

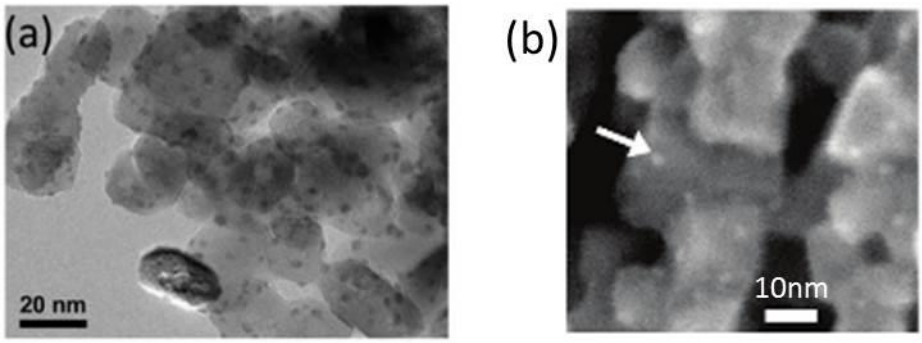

Figure 1.7| The perovskite quantum dot in liquid dye sensitized solar cells. *(a) TEM image of $CH_3NH_3PbI_3$ deposited on TiO_2 by Park et al. [78] (b) SEM image of $CH_3NH_3PbBr_3$ nanocrystalline particles on the TiO_2 surface by Miyasaka et al. [77]*

In both cases the perovskite absorbers were applied in quantum dots (QDs) deposited on TiO_2, although the absorbers dissolved or decomposed in the liquid electrolyte and the cells rapidly degraded within a few minutes.

Solid-state sensitized solar cell based on mesoporous scaffold

The breakthrough came in 2012, when Grätzel and co-workers collaborated with Park et al. They used $MAPbI_3$ as a light harvester in combination with the solid hole conductor 2,20,7,7,0-tetrakis-(N,N-dimethoxyphenyl-amine)-9,90-spirobi-fluorene (spiro-MeOTAD) on mesoporous TiO_2 (m-TiO_2) (figure 1.8 panel A), leading to a PCE of 9.7% [79]. At the same time, Snaith in collaboration with Miyasaka revealed

solar cells based on “meso-superstructured” scaffold, and the n-type mesoporous oxide can be replaced by an inert scaffold, such as Al_2O_3, onto which $CH_3NH_3PbI_{3-x}Cl_x$ and spiro-MeOTAD were coated [80]. The authors said that compared with the cells with m-TiO_2, the use of the Al_2O_3 scaffold (figure 1.8 panel B) avoids the voltage drop associated with the occupation of the TiO_2 band-tails and generates increased open circuit voltage (V_{OC}) values as high as 1.13 V and an efficiency of 10.9%. This result established that the perovskite materials can also behave as n-type semiconductors. But it seems that in the absence of an m-TiO_2 layer, a qualified compact TiO_2 (c-TiO_2) can still be detrimental in a well-performing device.

After these two publications, several works were reported in the past two years. A sequential deposition method (SDM) for the fabrication of perovskite on the m-TiO_2 film was introduced by Grätzel group [81], which gave a PCE of 15% and a certified value of 14.1% with high reproducibility. Snaith et al. reported a low temperature processed meso-superstructured solar cell with efficiency of 15.9% [82]. Subsequently, Park and Grätzel et al. reported perovskite solar cells based on mesoporous TiO_2 and controlled size $CH_3NH_3PbI_3$ cuboids, which achieved a best PCE of 17% [83]. And rapid and continuous improvements are obtained in the following works [84].

Park et al. also tried to prepare the solid-state solar cell based on submicrometer rutile TiO_2 nanorod with $MAPbI_3$ deposited on top. The device performance showed a PCE of 9.4% [85].

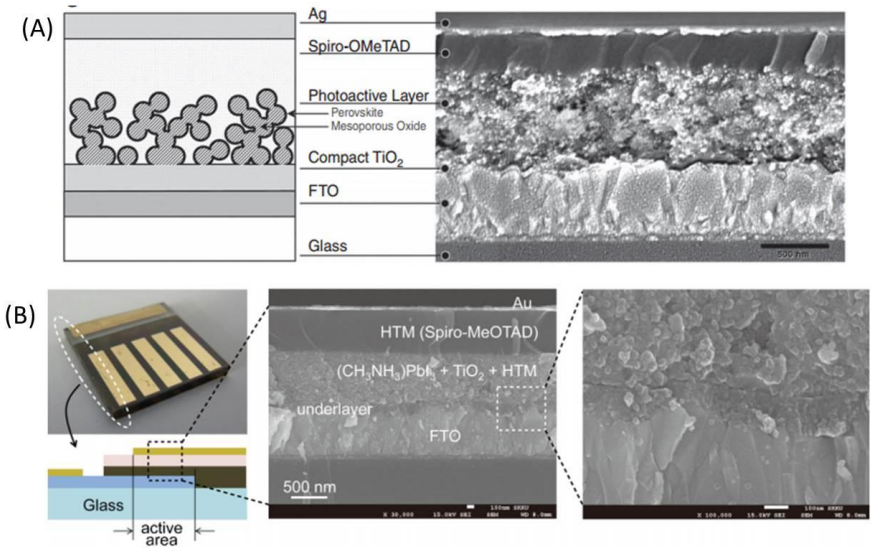

Figure 1.8 | The device architecture of Solid-state solar cell. *(A) shows the device structure of H. Snaith's report. [80] (B) shows the device structure of Grätzel and Park's report.[79]*

Planar heterojunction solar cell

The highest efficiencies in solution-processable perovskite-based solar cells have been achieved using an electron collection layer that requires sintering at 500 ℃. This is unfavourable for low-cost production, applications on plastic substrates, and multijunction device architectures. On the other hand, the dynamics of the high efficiency are not completely understanding in mesoporous structure based solar cell. Then came the planar heterojunction perovskite solar cell fabricated by vapour deposition which demonstrated 15.4% PCE, matched the 15% efficiency record of the mesoporous cell [86]. Subsequently, Nicholas and Snaith et al. reported a low-cost, solution-based deposition procedure utilizing nanocomposites of graphene and TiO_2 nanoparticles as the electron collection layers in meso-superstructured perovskite solar cells, these solar cells show remarkable photovoltaic performance with a power conversion efficiency up to 15.6% [87]. Kelly and Liu reported planar structure perovskite solar cells based on room temperature processed ZnO layer, which showed a PCE of 15.7% [88]. At the end of 2014, Yang et al. reported a planar solar cell with highest efficiency of 19.3% and 16.6% on average [89].

The remarkable achievements on devices performance from both materials science and device engineering promise further breakthroughs in this field of study [67, 90-93]. However, the understanding of the mechanisms underlying such exceptional performance has not grown at the same pace. Recent research results show that electron and hole diffusion lengths can exceed 100 nm in $CH_3NH_3PbI_3$ layers [94, 95], which is comparable or larger than the light propagation depth, indicating that the absorber thickness requirement to achieve complete absorption of solar irradiation is satisfied. Further investigation needs to be done to understand the mechanisms and to realize stable great performance.

1.3.2 Central questions

One year ago, the meeting held in San Francisco said the 20% PCE seemed a realistic goal to introduce the perovskite solar cell into industry. At the end of last year, NREL certified a high PCE of 20.1% solar cell based on perovskite. Does that mean the perovskite solar cell industry fabrication comes soon? The answer should be given with caution. In addition to PCE requirement for perovskite solar cell, commercialization is still challenging because of (a) the toxicity of Pb atoms, (b) long term stability, and (c) cost-effectiveness.

Up to now, the best performance of perovskite solar cell was based on Pb atom, whose commercialization is restricted because of toxicity. The lifetime of the solar cell modules is important as well, which is for Si cells more than 20 years. The cost-effectiveness may be the fatal factor to affect if it could be utilized to commercialization.

1.4 Objectives of this work and the organization

To realize a cheap perovskite solar cell to meet the energy problem, more investigations need to be done. Maximum efficiencies for perovskite solar cells are reported by Yan et al. with theoretically calculation [96]. Considering the optical absorption coefficient and bandgap of the light absorber, the theoretical maximum

efficiency for a 1 μm-thick perovskite solar cell composed of $CH_3NH_3PbI_3$ is 26%. Compared with the 20.1% PCE obtained to date, these results undoubtedly push researchers to devote to investigate the device engineering. Simultaneously, devoting to find some new other inorganic or organic pigments is an important way to go to solve the Pb toxic problem.

In this thesis, we shall to work on the basic property research with perovskite solar cell to understand the dynamics of the good performance, including photophysical properties and device investigation on $CH_3NH_3PbI_3$. The synthesis route and simple characterization are introduced in chapter 2. Photophysical properties upon light absorption and luminescence are discussed in chapter 3. The perovskite-based solar cell fabrication is discussed in chapter 4, especially on the morphology and interfacial modification.

References:

[1]. N. S. Lewis, D. G. Nocera, "Powering the Planet: Chemical Challenges in Solar Energy Utilization", ***Proc. Natl. Acad. Sci.*** 2006, 103, 15729.

[2]. S. E. Shaheen, G. E. Jabbour, M. M. Morrell, "Bright Blue Organic Light-Emitting Diode with Improved Color Purity Using a LiF/Al Cathode", ***J. Appl. Phys.*** 1998, 84, 2324.

[3]. D. Ginley, M. A. Green, R. Collins, ***MRS Bull.*** 2008, 33, 355.

[4]. P. A. Alivisatos, "Perspectives on the Physical Chemistry of Semiconductor Nanocrystals" , ***J. Phys. Chem.*** 1996, 100, 13226.

[5]. C. B. Murray, C. R. Kagan and M. G. Bawendi "Synthesis and Characterization of Monodisperse Nanocrystals and Close-Packed Nanocrystal Assemblies", ***Annu. Rev. Mater. Sci.*** 2000. 30, 545.

[6]. M. Shim, C. J. Wang, D. J. Norris, P. Guyot-Sionnest, MRS Bull. 2001, 26, 1005.

[7]. C. Wadia, A. P. Alivisatos, D. M. Kammen, "Materials Availability Expands the Opportunity for Large-Scale Photovoltaics Deployment.", ***Environ. Sci. Technol.*** 2009, 43, 2072.

[8]. W. Shockley, H. Queisser, "Detailed Balance Limit of Efficiency of P-N Junction Solar Cells", ***J. Appl. Phys.***, 1961, 32, 510.

[9]. Light sensitive electric device. US Patent 240252, filed 27 March 1941.

[10]. G. L. Pearson. "PV founders award luncheon". Conference Record, 18th IEEE Photovoltaic Specialists Conference, Las Vegas, IEEE, New York, 1985.

[11]. D. Chapin, C. Fuller, G. Pearson, "A New Silicon P-N Junction Photocell for Converting Solar Radiation into Electrical Power", ***J. Appl. Phys.*** 1954, 25, 676.

[12]. J. Zhao, A. Wang, P. P. Altermatt, S. R. Wenham, "24% Efficient Perl Silicon Solar Cell: Recent Improvements in High Efficiency Silicon Cell Research", ***Sol. Energy Mater. Sol. Cells,*** 1996, 41, 87.

[13]. Arnulf Jäger-Waldau, "European Research Roadmap For Photovoltaics",

Preprint World Renewable Energy Congress VIII, Denver, 2004

[14]. J. M. Gee, R. R. King, K. W. Mitchell, in Proc. IEEE 25th Photovolt. Specialist connference, ed. by P. Basore (IEEE, New York, 1996), p. 409.

[15]. J. Zhao, A. Wang, M. A. Green, F. Ferrazza, "19.8% Efficient 'honeycomb' Textured Multicrystalline and 24.4% Monocrystalline Silicon Solar Cells", ***Appl. Phys. Lett.*** 1998, 73, 1991.

[16]. D. E. Carlson, "Amorphous-Silicon Solar Cells", ***IEEE Transactions on Electron Devices.*** 1989, 36, 12.

[17]. C. Marschner, J. Baumgartner, A. Wallner, "Structurally and Conformationally Defined Small Methyl Polysilanes", ***Dalton Trans***. 2006, 5667.

[18]. T. Shimoda, Y. Matsuki, M. Furusawa, T. Aoki, I. Yudasaka, H. Tanaka, H. Iwasawa, D. Wang, M. Miyasaka, Y. Takeuchi, "Solution-Processed Silicon Films and Transistors", ***Nature***. 2006, 440, 783.

[19]. S. Han, X. Dai, P. Loy, J. Lovaasen, J. Huether, J. Hoey, A. Wagner, J. Sandstrom, D. Bunzow, O. Swenson, I. Akhatov, D. Schulz, "Printed Silicon as Diode and FET Materials – Preliminary Results", ***Journal of Non-Crystalline Solids***. 2008, 354, 2623.

[20]. I. Repins, M. Contreras, B. Egaas, C. DeHart, J. Scharf, C. Perkins, B. To, R. Noufi, "19.9%-Efficient ZnO/CdS/$CuInGaSe_2$ Solar Cell with 81.2% Fill Factor", ***Prog. Photovolt: Res. Appl.*** 2008; 16, 235.

[21]. M. Lammer, U. Klemm, M. Powalla,"Sodium Co-Evaporation for Low Temperature Cu (In, Ga) Se_2 Deposition" , ***Thin Solid Films***. 2001, 387, 33.

[22]. M.G. Panthani, V. Akhavan, B. Goodfellow, "Synthesis of $CuInS_2$, $CuInSe_2$, and $Cu(In_xGa_{1-x})$ Se_2 (CIGS) Nanocrystal 'Inks' for Printable Photovoltaics" , ***J. Am. Chem. Soc.*** 2008, 130, 16770.

[23]. R. Caballero, C. A. Kaufmann, T. Eisenbarth, M. Cancela, "The Influence of Na on Low Temperature Growth of CIGS Thin Film Solar Cells on Polyimide Substrates" , ***Thin Solid Films***. 2009, 517, 2187.

[24]. M. A. Green, "Self-consistent optical parameters of intrinsic silicon at 300K including temperature coefficients", ***Sol. Energy Mater. Sol. Cells***, 2008, 92,

1305.

[25]. T. Aramoto, S. Kumazawa, H. Higuchi, "16.0% Efficient Thin-Film CdS/CdTe Solar Cells", ***Jpn. J. Appl. Phys.*** 1997, 36, 6304.

[26]. B. E. McCandless, L. V. Moulton, "Recrystallization and Sulfur Diffusion in $CdCl_2$-treated CdTe/CdS Thin Films", ***Prog. Photovolt. Res. Appl.*** 1997**,** 5, 249.

[27]. Y. L. Lee, B. M. Huang, H. T. Chien, "Highly Efficient CdSe-Sensitized TiO_2 Photoelectrode for Quantum-Dot-Sensitized Solar Cell Applications" ***Chem. Mater.*** 2008, 20, 6903.

[28]. L. W. Chong, H. T. Chien, Y. L. Lee, "Assembly of CdSe onto Mesoporous TiO_2 Films Induced by a Self-Assembled Monolayer for Quantum Dot-Sensitized Solar Cell Applications", ***Journal of Power Sources***, 2010, 195, 5109.

[29]. A. Ennaoui, S. Fiechter, C. Pettenkofer, "Iron Disulfide for Solar Energy Conversion", ***Sol. Energy Mater. Sol. Cells***, 1993, 29, 289.

[30]. M. Cabán-Acevedo, M. S. Faber, Y. Tan, R. J. Hamers, "Synthesis and Properties of Semiconducting Iron Pyrite (FeS_2) Nanowires", ***Nano Lett.*** 2012, 12, 1977.

[31]. R. J. Stirn, Y. Yeh, "A 15% Efficient Antireflection coated Metal-oxide semiconductor Solar Cell", ***Appl. Phys.lett.*** 1975, 27, 95.

[32]. G. J. Bauhuis, P. Mulder, E. J. Haverkamp, J. Huijben,"26.1% Thin-Film GaAs Solar Cell Using Epitaxial Lift-Off", ***Sol. Energy Mater. Sol. Cells,*** 2009, 93, 1488.

[33]. K. BÖER, "The CdS/Cu_2S Solar Cell I. Minority Carrier Generation and Transport in the Cu_2S Emitter", ***Phys. Stat. Sol. (a)***. 1977, 40, 355.

[34]. L. C. Olsen, R. C. Bohara, M. W. Urie, "Explanation for Low−efficiency Cu_2O Schottky−barrier Solar Cells", ***Appl. Phys. Lett.*** 1979, 34, 47.

[35]. H. Katagiri, K. Jimbo, W. Maw, K. Oishi, M. Yamazaki, H. Araki, A. Takeuchi, "Development of CZTS-Based Thin Film Solar Cells", ***Thin Solid Films***. 2009, 517, 2455.

[36]. V. A. Akhavan, B. W. Goodfellow, M. G. Panthani, "Colloidal CIGS and CZTS

Nanocrystals: A Precursor Route to Printed Photovoltaics", ***Journal of Solid State Chemistry***, 2012, 189, 2.

[37]. J. M. Nunzi,"Organic Photovoltaic Materials and Devices", ***Comptes Rendus Physique***. 2002, 3, 523.

[38]. S. R. Forrest, "The Path to Ubiquitous and Low-Cost Organic Electronic Appliances on Plastic", ***Nature***. 2004, 428, 911.

[39]. S. R. Marder, J. E. Sohn, G. D. Stucky, Eds, "Materials for Non-linear Optics: Chemical Perspectives". F. Wudl, the American Chemical Society, Washington DC, 1991, 683.

[40]. J. Hummelen, B. Knight, F. LePeq, F. Wudl, J. Yao, C. Wilkins, "Preparation and Characterization of Fulleroid and Methanofullerene Derivatives", ***J. Org. Chem.*** 1995, 60, 532.

[41]. M. Wienk, J. Kroon, W. Verhees, J. Knol, J. Hummelen, P. Hal, R. Janssen, "Efficient Methano [70]fullerene/MDMO-PPV Bulk Heterojunction Photovoltaic Cells", ***Angew. Chem.*** 2003, 115, 3493.

[42]. F. Padinger, R. S. Rittberger, N. S. Sariciftci, "Effects of Postproduction Treatment on Plastic Solar Cells", ***Adv. Funct. Mater***. 2003, 13, 85.

[43]. G. Li, V. Shrotriya, J. Huang, Y. Yao, T. Moriarty, K. Emery, Y. Yang, "High-Efficiency Solution Processable Polymer Photovoltaic Cells by Self-Organization of Polymer Blends", ***Nature Materials***. 2005, 4, 864.

[44]. W. Ma, C. Yang, X. Gong, K. Lee, A. Heeger, "Thermally Stable, Efficient Polymer Solar Cells with Nanoscale Control of the Interpenetrating Network Morphology", ***Adv. Funct. Mater.*** 2005, 15, 1617.

[45]. D. Mühlbacher, M. Scharber, M. Morana, Z. Zhu, D. Waller, R. Gaudiana, C. Brabec, "High Photovoltaic Performance of a Low-Bandgap Polymer", ***Adv. Mater.*** 2006, 18, 2884.

[46]. S. Park, A. Roy, S. Beaupré, S. Cho, N. Coates, J. Moon, D. Moses, M. Leclerc, K. Lee, A. Heeger, "Bulk Heterojunction Solar Cells with Internal Quantum Efficiency Approaching 100%" , ***Nature Photonics***. 2009, 3, 297.

[47]. C. W. Tang, "Two-Layer Organic Photovoltaic Cell" ***Appl. Phys. Lett.*** 1986, 48,

183.

[48]. M. Hiramoto, H. Fujiwara, M. Yokoyama, "Three-layered organic solar-cell with a photoactive interlayer of codeposited pigments", ***Appl. Phys. Lett.*** 1991, 58, 1062.

[49]. P. Peumans, V. Bulović, S.R. Forrest, "Efficient Photon Harvesting at High Optical Intensities in Ultrathin Organic Double-Heterostructure Photovoltaic Diodes", ***Appl. Phys. Lett.*** 2000, 76, 2650.

[50]. Y. Liu, C. C. Chen, Z. Hong, J. Gao, Y. M. Yang, H. Zhou, "Solution-Processed Small-Molecule Solar Cells: Breaking the 10% Power Conversion Efficiency" , ***Sci. Rep.*** 2013,3:3356.

[51]. H. J. Syu, S. C. Shiu, C. F. Lin, "Silicon Nanowire/organic Hybrid Solar Cell with Efficiency of 8.40%", ***Sol. Energy Mater. Sol. Cells,*** 2012, 98, 267.

[52]. E. C. Garnett, P. Yang, "Silicon Nanowire Radial P− N Junction Solar Cells", ***J. Am. Chem. Soc.*** 2008, 130, 9224.

[53]. W.J.E. Beek, M.M. Wienk, R.A.J. Janssen, "Efficient Hybrid Solar Cells from Zinc Oxide Nanoparticles and a Conjugated Polymer", ***Adv. Mater.*** 2004, 16, 1009.

[54]. H. C. Chen, C. W. Lai, I. C. Wu, H. R. Pan, I. Chen, "Enhanced Performance and Air Stability of 3.2% Hybrid Solar Cells: How the Functional Polymer and CdTe Nanostructure Boost the Solar Cell Efficiency", ***Adv. Mater.*** 2011, 23, 5451.

[55]. http://webmineral.com/data/Perovskite.shtml#.VOanV9LF9hg.

[56]. M. A. Pena, J. Fierro, "Chemical Structures and Performance of Perovskite Oxides", ***Chem. Rev.*** 2001, 101, 1981.

[57]. V. M. Goldschmidt, "Geochemische Verteilungsgesetze der Elemente", ***Skrifter Norske Videnskaps-Akad. Oslo, (I) Mat. Natur.*** 1926, No. 8.

[58]. H. Wells, "Über Die Cäsium‐ Und Kalium‐Bleihalogenide", ***Z. Anorg. Chem.*** 1893, 3, 195.

[59]. C. Moller,"A phase transition in cæsium plumbochloride" ***Nature***. 1957, 180, 981.

[60]. C. Moller, "Crystal Structure and Photoconductivity of Cæsium Plumbohalides", ***Nature***. 1958, 182, 1436.

[61]. L. Protesescu, S. Yakunin, M.I. Bodnarchuk, F. Krieg, "Nanocrystals of Cesium Lead Halide Perovskites ($CsPbX_3$, X= Cl, Br, and I): Novel Optoelectronic Materials Showing Bright Emission with Wide Color Gamut", ***Nano Lett.*** 2015, **DOI:** 10.1021/nl5048779

[62]. (a).T. KARANTASSIS, ***Bull. Soc. Chim.*** 1926, 39, 43. (b).T. KARANTASSIS, ***Ann. Chim***. 1927, 8, 71.

[63]. L. Ch'ih-fa and I. S. Morozov, ***Russ. J. Inorg. Chem.*** 1963, 8, 359.

[64]. D.E. Scaife, P.F. Weller, W.G. Fisher, "Crystal Preparation and Properties of Cesium Tin (II) Trihalides", ***Journal Of Solid State Chemistry***, 1974, 9,308.

[65]. D. Weber, "$CH_3NH_3SnBrxI_{3-x}$ (x= 0-3), a Sn(II)-System with Cubic Perovskite Structure", ***Z. Naturforsch.*** 1978, 33 b, 862.

[66]. D. Weber, "$CH_3NH_3PbX_3$, a Pb(II)-System with Cubic Perovskite Structure", ***Z. Naturforsch.*** 1978, 33 b, 1443.

[67]. W. Zhang, M. Anaya, G. Lozano, M.E. Calvo, M.B. Johnston, H. Miguez, H.J. Snaith, "Highly Efficient Perovskite Solar Cells with Tuneable Structural Color.", ***Nano Lett.*** 2015, DOI: 10.1021/nl504349z.

[68]. P. Schouwink, M. Ley, A. Tissot, H. Hagemann, T. Jensen, Ľ. Smrčok, R. Černý, "Structure and Properties of Complex Hydride Perovskite Materials" , ***Nat. Comms***. 2014, 5:5706.

[69]. I. Borriello, G. Cantele, D. Ninno, "Ab Initio Investigation of Hybrid Organic-Inorganic Perovskites Based on Tin Halides", ***Phys. Rev. B***. 2008, 77, 235214.

[70]. J. Noh, S. Im, J. Heo, T. Mandal, S. Seok, "Chemical Management for Colorful, Efficient, and Stable Inorganic-Organic Hybrid Nanostructured Solar Cells", ***Nano Letters***. 2013, 13, 1764.

[71]. D.B. Mitzi, K. Liang, "Synthesis, Resistivity, and Thermal Properties of the Cubic Perovskite $NH_2CH{=}NH_2SnI_3$ and Related Systems", ***Journal Of Solid State Chemistry,*** 1997, 134, 376.

[72]. R. Jakubas, "Ferroelectric Phase Transition in Tris (dimethylammonium) Nonachlorodiantimonate(III) $[NH_2(CH_3)_2]_3Sb_2Cl_9$", ***Solid State Communications,*** 1986, 60, 389.

[73]. D.B. Mitzi, K. Liang, S. Wang, "Synthesis and Characterization of $[NH_2C(I)NH_2]_2ASnI_5$ with A=Iodoformamidinium or Formamidinium: The Chemistry of Cyanamide and Tin (II) Iodide in Concentrated Aqueous Hydriodic Acid Solutions", ***Inorg. Chem.*** 1998, 37, 321.

[74]. A.M. Salau, "Fundamental Absorption Edge in PbI_2: KI Alloys" , ***Sol. Energy Mater.*** 1980,2, 327.

[75]. M. Schoijet, "Possibilities of new materials for solar photovoltaic cells", ***Sol. Energy Mater.*** 1979, 1, 43.

[76]. A. H. Nethercot, "Prediction Of Fermi Energies And Photoelectric Thresholds Based On Electronegativity Concepts", ***Phys. Rev. Lett.*** 1974, 33.1088.

[77]. A. Kojima, K. Teshima, Y. Shirai, T. Miyasaka, "Organometal Halide Perovskites as Visible-Light Sensitizers for Photovoltaic Cells", ***J. Am. Chem. Soc.*** 2009, 131, 6050.

[78]. J.-H. Im, C.-R. Lee, J.-W. Lee, S.-W. Park, N.-G. Park, "6.5% Efficient Perovskite Quantum-Dot-Sensitized Solar Cell", ***Nanoscale***. 2011, 3, 4088.

[79]. H.-S. Kim, C.-R. Lee, J.-H. Im, K.-B. Lee, T. Moehl, A. Marchioro, S.-J. Moon, R. Humphry-Baker, J.-H. Yum, J. Moser, M. Grätzel, N.-G. Park, "Lead Iodide Perovskite Sensitized All-Solid-State Submicron Thin Film Mesoscopic Solar Cell with Efficiency Exceeding 9%", ***Sci. Rep***. 2012, 2, 591.

[80]. M. Lee, J. Teuscher, T. Miyasaka, T. Murakami, H. Snaith, "Efficient Hybrid Solar Cells Based on Meso-Superstructured Organometal Halide Perovskites" , ***Science***. 2012, 338, 643.

[81]. J. Burschka, N. Pellet, S.-J. J. Moon, R. Humphry-Baker, P. Gao, M.K. Nazeeruddin, M. Grätzel, "Sequential Deposition as a Route to High-Performance Perovskite-Sensitized Solar Cells", ***Nature***. 2013, 499, 316.

[82]. K. Wojciechowski, M. Saliba, T. Leijtens, A. Abate, H.J. Snaith, "Sub-150 C Processed Meso-Superstructured Perovskite Solar Cells with Enhanced

Efficiency", ***Energy Environ. Sci.*** 2014, 7, 1142.

[83]. J. H. Im, I. H. Jang, N. Pellet, M. Grätzel, N. G. Park, "Growth of $CH_3NH_3PbI_3$ Cuboids with Controlled Size for High-Efficiency Perovskite Solar Cells", ***Nat. Nanotechnol***. 2014, 9, 927.

[84]. J. Choi, X. Yang, Z. Norman, S. Billinge, J. Owen, "Structure of Methylammonium Lead Iodide within Mesoporous Titanium Dioxide: Active Material in High-Performance Perovskite Solar Cells", ***Nano Letters***. 2014, 14, 127.

[85]. H.S. Kim, J.W. Lee, N. Yantara, P.P. Boix, S.A. Kulkarni, S. Mhaisalkar, M. Grätzel, N.G. Park, "High Efficiency Solid-State Sensitized Solar Cell-Based on Submicrometer Rutile TiO_2 Nanorod and $CH_3NH_3PbI_3$ Perovskite Sensitizer", ***Nano Lett.*** 2013, 13, 2412.

[86]. M. Liu, M. Johnston, H. Snaith, "Efficient Planar Heterojunction Perovskite Solar Cells by Vapour Deposition", ***Nature***. 2013, 501, 395.

[87]. J. Wang, J. Ball, E. Barea, A. Abate, J. Alexander-Webber, J. Huang, M. Saliba, I. Mora-Sero, J. Bisquert, H. Snaith, R. Nicholas, "Low-Temperature Processed Electron Collection Layers of Graphene/TiO_2 Nanocomposites in Thin Film Perovskite Solar Cells", ***Nano Lett.*** 2014, 14, 724.

[88]. D. Liu, T. Kelly, "Perovskite Solar Cells with a Planar Heterojunction Structure Prepared Using Room-Temperature Solution Processing Techniques", ***Nature Photonics***. 2014, 8, 133.

[89]. H. Zhou, Q. Chen, G. Li, S. Luo, T. Song, H.S. Duan, Z. Hong, J. You, Y. Liu, Y. Yang "Interface Engineering of Highly Efficient Perovskite Solar Cells", ***Science***. 2014,345, 542.

[90]. Y. Y. Y. Sun, M. L. Agiorgousis, P. Zhang, S. Zhang, "Chalcogenide Perovskites for Photovoltaics", ***Nano Lett.*** 2015, 15, 581.

[91]. M. Zhang, M. Lyu, H. Yu, J.-H.H. Yun, Q. Wang, L. Wang, "Stable and Low-Cost Mesoscopic $CH_3NH_3PbI_2Br$ Perovskite Solar Cells by Using a Thin poly(3-Hexylthiophene) Layer as a Hole Transporter", ***Chem. Eur. J.*** 2015, 21, 434.

[92]. R. Sheng, A. Ho-Baillie, S. Huang, S. Chen, X. Wen, X. Hao, M. Green, "Methylammonium Lead Bromide Perovskite-Based Solar Cells by Vapor-Assisted Deposition", ***J. Phys. Chem. C***. 2015,DOI: 10.1021/jp512936z.

[93]. Z. Xiao, Y. Yuan, Y. Shao, Q. Wang, Q. Dong, C. Bi, P. Sharma, A. Gruverman, J. Huang, "Giant Switchable Photovoltaic Effect in Organometal Trihalide Perovskite Devices", ***Nat. Mater***. 2015, 14, 193.

[94]. G. Xing, N. Mathews, S. Sun, S.S. Lim, Y.M. Lam, M. Grätzel, S. Mhaisalkar, T.C. Sum, "Long-Range Balanced Electron- and Hole-Transport Lengths in Organic-Inorganic $CH_3NH_3PbI_3$", ***Science***. 2013, 342, 344.

[95]. S.D. Stranks, G.E. Eperon, G. Grancini, C. Menelaou, M.J. Alcocer, T. Leijtens, L.M. Herz, A. Petrozza, H.J. Snaith, "Electron-Hole Diffusion Lengths Exceeding 1 Micrometer in an Organometal Trihalide Perovskite Absorber", ***Science***. 2013, 342, 341.

[96]. W.J. Yin, T. Shi, Y. Yan, "Unique Properties of Halide Perovskites as Possible Origins of the Superior Solar Cell Performance", ***Adv. Mater.*** 2014, 26, 4653.

CHAPTER 2
Synthesis and characterization

2.1 Synthetic techniques

The synthesis of Perovskite is the primary and important procedure among perovskite studies. Compared with the methodology of traditional semiconductors, the fabrication of perovskite samples is relatively easy. Because no complicated equipment is needed, nor strict environment conditions are enforced, it is not difficult to design the perovskite as we want by working on the organic part. In general, there are two steps to produce metal-halide perovskites: (i) synthesis of organic salts and (ii) preparation of perovskite film. The precursors lead halide salts $PbCl_2$, $PbBr_2$ and PbI_2 are purchased from Sigma-Aldrich Company. For the organic part, we synthesized the molecules in our lab. In the synthesis, the methylamine solution 33wt% in ethanol (534102-250ml), hydriodic acid (HI) 57wt% in water (210013-50ml) and hydrobromic acid (HBr) 48wt% in water (244260-500ml) are from Sigma-Aldrich Company.

2.1.1 Organic group synthesis

The perovskites that we are interested in are Pb-based organic compounds. At first, we need to synthesize the ammonium salts from the amines we bought by reacting the amines with a halogen acid. The process could be described by formula (2.1):

$$R - NH_2 + HX \Rightarrow R - NH_2HX \tag{2.1}$$

which is a neutralization reaction, in which the salts are easy to obtain with a high yield (nearly 100%). In the formula 2.1, R is organic group (such as CH_3CH_2-,

$CH_3CH_2CH_2$-); X is halide element (such as Cl, I, Br). The hydrogen halides used to produce corresponding ammonium salts are HI 57 wt% or HBr 48 wt% aqueous solution respectively. The reaction setup is shown in Figure 2.1:

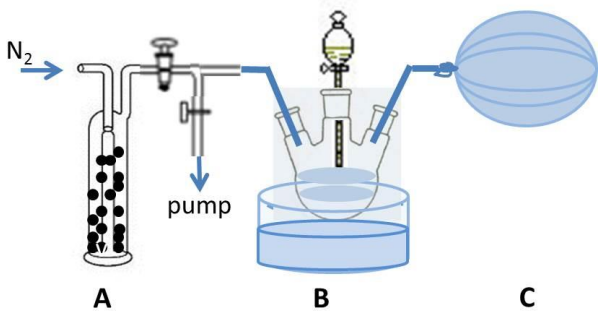

Figure 2.1 | *Reaction set-up to produce the ammonium salts.*

Before the reaction, it is necessary to check the leakage of the whole system to make sure that every part is well connected to each other. Vacuum grease is helpful for the joint position to ensure there is no leakage along the N_2 tube. The synthesis occurs under N_2 protection to avoid oxidation [1, 2].

The CH_3NH_3I Synthesis

At first, The N_2 (from SOL company, 99.9% purity) is passed through the drier bottle (Figure 2.1 part A), in which enough $CaCl_2$ is filled in as desiccant to remove the water. It is necessary to exchange the air in the system with N_2 by evacuating the air out and filling with N_2 three times. The three arms flask (in the B part of Figure 2.1) is filled with 50ml ethanol and 12ml methylamine (33wt% in ethanol). In order to keep the reaction temperature at 0 Celsius, the flask is put in a bath filled with ice and water. After the N_2 exchange, 5 ml hydriodic acid (57% in water) is added dropwise while stirring. The reaction is exothermic and goes on for 2 hours at 0 Celsius. To keep the reaction under stable pressure, the safety balloon is necessary in the system (Figure 2.1 part C).

The final product is dried with a rotary evaporator at a temperature below 50 Celsius in 30 minutes to eliminate the residual solvent, such as ethanol and water. The

color of the dry product is light yellow which means a small amount of residual reagents is still mixed with the ammonium salts. In order to purify the salt, we can wash the dry product with diethyl ether at room temperature to remove the residues, as the diethyl ether is a good solvent for amine and the acid but the salts have very low solubility in it. After washing the salts three times, a white powder (a little light yellow) could be obtained. The final CH_3NH_3I (MAI) ammonium salt is dried in vacuum overnight. After the drying procedure, the final salt is stored in the nitrogen filled glove box because the salt is hygroscopic.

The CH_3NH_3Br Synthesis

The synthesis is similar to the CH_3NH_3I synthesizing procedure. Typical quantities were 12 ml methylamine, 4.3 ml hydrobromic acid and 50 ml ethanol. Keep the reacting flask stirring in an ice bath for 2 hours. Crystallization of methylammonium bromide (CH_3NH_3Br) was achieved using a rotary evaporator at 50 Celsius for 1 hour. A white colour powder was formed indicating successful crystallization.

It is difficult to distinguish if the powder is pure or not, because both of the CH_3NH_2 and the HBr are colourless. Comparing to the CH_3NH_3I, diethyl ether was used to wash the CH_3NH_3Br salt to remove the residual reagents (maybe the methylamine) in the salt. After washing the salts at room temperature, the final CH_3NH_3Br (MABr) salt was dried in vacuum overnight and stored in a nitrogen filled glove box.

2.1.2 Perovskite thin film preparation

After the synthesis, the dry ammonium salts are used to prepare perovskite samples. In this stage, we introduce 2 routes to prepare the perovskites: (1) single step from solution and (2) two steps. The two-step route has a further two-fold ramification in two different methods, as the perovskite could be synthesized by evaporating organic group or spin-coating organic group.

In general, this reaction can be described by the chemical formula 2.2:

$$R - NH_3X + MX_2 \Rightarrow R - NH_3MX_3 \quad (2.2)$$

where the R- is organic group, the X- is halide element and the M is metal cation. In this thesis, the M part is always Lead (Pb). The formula indicates that the ammonium salts could be reacted with Pb halide to generate perovskite. To explain the perovskite film preparation, I will take the $CH_3NH_3PbI_3$ as the example in the following description.

2.1.2.1 Perovskite prepared with single step solution deposition

To obtain the $CH_3NH_3PbI_3$ precursor solution, CH_3NH_3I ammonium salt and lead halide PbI_2 are dissolved in anhydrous N, N-Dimethylformamide (DMF) in a 3:1 molar ratio of CH_3NH_3I to PbI_2, with final concentrations 2.64M ammonium salts and 0.88M lead halide. The solution is then put in ultrasonic bath until the solutes are totally dissolved and the solution appears limpid.

Our thin film samples are realized by spin-coating, by which the perovskite form 2D crystals through a self-organization process [3, 4]. The spin-coating method is a technique used to apply uniform thin films to flat substrates. A small amount (20μl) of solution is dropped on the substrate which is fixed on the spin-coater, and then the substrate is rotated at high speed in order to spread the solution by centrifugal force to form a thin film.

Before spin-coating procedure, the substrates and the perovskite precursor are warmed up to 70 Celsius. To form the perovskite layer for applications and measurements, the precursors are spin-coated, not necessarily in stoichiometric ratio (for instance 3 CH_3NH_3I to 1 PbI_2), on the flat substrate at 3000rpm for 30 minutes in glove box. After spin-coating, the fresh $CH_3NH_3PbI_3$ films are annealed on hotplate at 100 ℃ for 60 minutes. For the optical measurements, when the perovskite film would not be covered by other functional layers and needs protection from ambient air, a top layer is deposited via spin-coating 10mg/ml chlorobenzene solutions of

poly(methylmethacrylate) (PMMA; Sigma-Aldrich) at 3000 rpm in glove box.

As it will be shown later in this thesis, the perovskite prepared by this method takes the form of needle-shaped crystal and the resulting film is not homogeneous, probably because the stacking of adjacent needles cannot be controlled. In order to get a homogeneous flat film on substrate, which is more desirable for a planar solar cell, we introduce the two-step method.

2.1.2.2 Perovskite prepared with two steps in solution

To obtain the $CH_3NH_3PbI_3$ film with two-step method, the PbI_2 film should be deposited first on the substrates, and then the perovskite layer crystallizes upon either evaporating the CH_3NH_3I ammonium salt in N_2 or spin-coating the CH_3NH_3I from solution. Let us first address the procedure involving spin coating as second step [5].

Before spin-coating procedure, the PbI_2 is dissolved in anhydrous N,N-Dimethylformamide with 1M concentration and the ammonium salts are dissolved in anhydrous isopropanol with concentration 10mg/ml. Both of the two solutions should be kept in strong stirring at 70 ℃ for 2 hours. After warming the PbI_2 solution and the substrates to 70 Celsius for 20 minutes, we can spin coat the PbI_2 at 7000rpm for 30 seconds to get a very uniform film. The fresh PbI_2 film is dried on the hotplate at 70 Celsius for 10 minutes. The ammonium salts should be spin-coated on the PbI_2 film at 3000rpm for 30 seconds. Annealing at 100 Celsius on hotplate for 1 hour is necessary to get a perovskite crystal. The colour changing from light yellow to dark brown indicates a perovskite film is generated.

After the synthesis, there should be a small amount of ammonium salt residues in the perovskite film, which could be removed by rinsing the film in isopropanol solvent. After rinsing with isopropanol, washing again with isopropanol is necessary when the substrate is rotating. Annealing another 1 hour could make sure we have a perovskite thin film.

The film from this method is better in uniformity than solution method, but there is always a wave ring shape in the film, which makes the film thickness very different at different region. So we can choose another two-step method to avoid this problem.

2.1.2.3 Perovskite prepared with vapour assisted two-step method by evaporating ammonium salts

The vapour assisted two-step method is similar to the solution method. To get the $CH_3NH_3PbI_3$ film with this method, the PbI_2 film should be prepared at first (figure 2.2 part A).

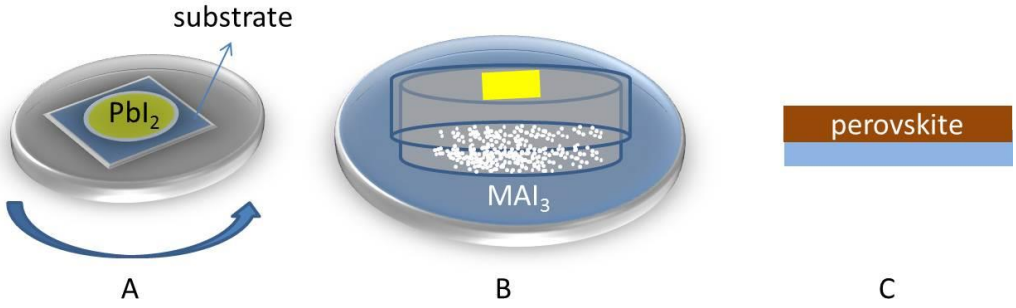

Figure 2.2| *Scheme of the evaporation procedure.* *From left to right: first a layer of lead halide salt is deposited by spin coating a salt solution on the substrate; then the hybrid salt (methylammonium iodide in this case) is warmed up in a petri dish and evaporated on the lead salt; finally the reaction occurs on the substrate and a crystalline perovskite film forms.*

The other preparation procedures [6] are illustrated in figure 2.2. The CH_3NH_3I ammonium salts could be evaporated to the PbI_2 film in nitrogen filled glove box. The substrate with the PbI_2 film is in the centre of a petri dish, where ammonium salts (about 200 mg) are placed in powder form on the bottom. The petri dish is kept at 150 Celsius overnight. The colour of the film in the first hour looks a little yellow. The colour turns to be darker as time goes on. 15 hours later, the film becomes black, which means the perovskite is ready.

To make sure there is no excess ammonium salt on the perovskite film, the isopropanol washing is necessary. Annealing on hotplate at 100 Celsius for 1 hour after the washing procedure to eliminate the solvent in the film produces good quality

perovskite crystals.

2.2 Characterization techniques

2.2.1 X-ray Diffraction

X-ray diffraction is a technique used for identifying the structure of a crystal, in which the crystal atoms cause a beam of incident X-rays to diffract into specific directions. By measuring the angles and intensities of these diffracted beams, a crystallographer can produce a three-dimensional picture of atoms within the crystal, determining the mean positions of the atoms, as well as their chemical bonds, their disorder and various other pieces of information [7].

With a steady X-ray source, diffraction can be determined by Bragg's law (formula 2.3):

$$2\mathrm{d}\sin\theta = n\lambda \tag{2.3}$$

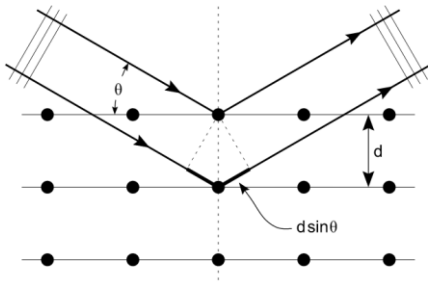

Figure 2.3| *The X-ray diffraction scheme.*

As the Figure 2.3 shows, d is the spacing between diffracting planes, θ is the incident angle, n is any integer, and λ is the wavelength of the beam. These specific directions appear as spots on the diffraction pattern called reflections. Thus, X-ray diffraction results from an electromagnetic wave (the X-ray) impinging on a regular array of scatters (the repeating arrangement of atoms within the crystal).

The organometal halide perovskite has an ABX_3 structure [8]. Figure 2.4 shows that in the centre of crystal unit is an ammonium cation; the Pb cations locate around

the organic group and form a cube structure; the halide anions are located between the Pb cations and form an octahedron with the Pb in the centre. [9, 10]

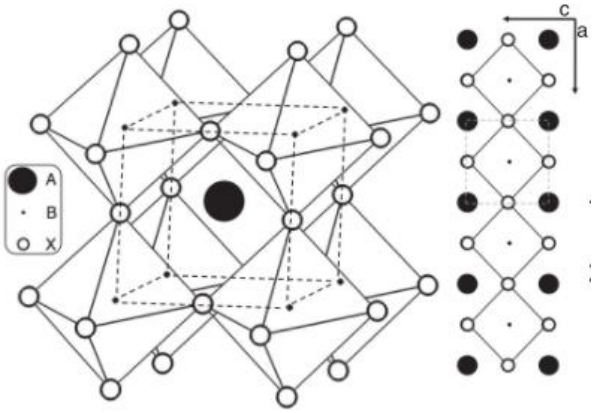

Figure 2.4| *Left: Three-dimensional schematic representation of perovskite structure ABX_3 ($A = CH_3NH_3^+$, $B = Pb^{2+}$, and X = Cl, Br, I). Right: Two-dimensional schematic illustrating the perovskite unit cell. [8]*

The X-ray diffraction (XRD) patterns were recorded by a Bruker D8-Discover diffractometer for thin films with parallel beam geometry and Cu Kα wavelength. Symmetric ω-2θ scans were obtained using a step size of 0.02 °and time per step of 4s.

Figure 2.5 shows the XRD patterns of the $CH_3NH_3PbI_3$ and $CH_3NH_3PbBr_3$ perovskites. The films were prepared by spin coating from different solutions of precursors: stoichiometric 1:1 mixture of CH_3NH_3I of PbI_2 in DMF to obtain the $CH_3NH_3PbI_3$ (Panel B); stoichiometric 1:1 mixture of CH_3NH_3Br and $PbBr_2$ to promote the formation of the $CH_3NH_3PbBr_3$ (Panel A). For $CH_3NH_3PbI_3$ perovskite film, all Bragg peaks were indexed as (hh0) Bragg reflections on a tetragonal I4/mcm cell with $a=b\cong\sqrt{2}a_c$, $c\cong 2a_c$ indicating a highly oriented growth, with films having the phase of the cubic perovskite cell (with lattice parameter) parallel to the deposition plane.

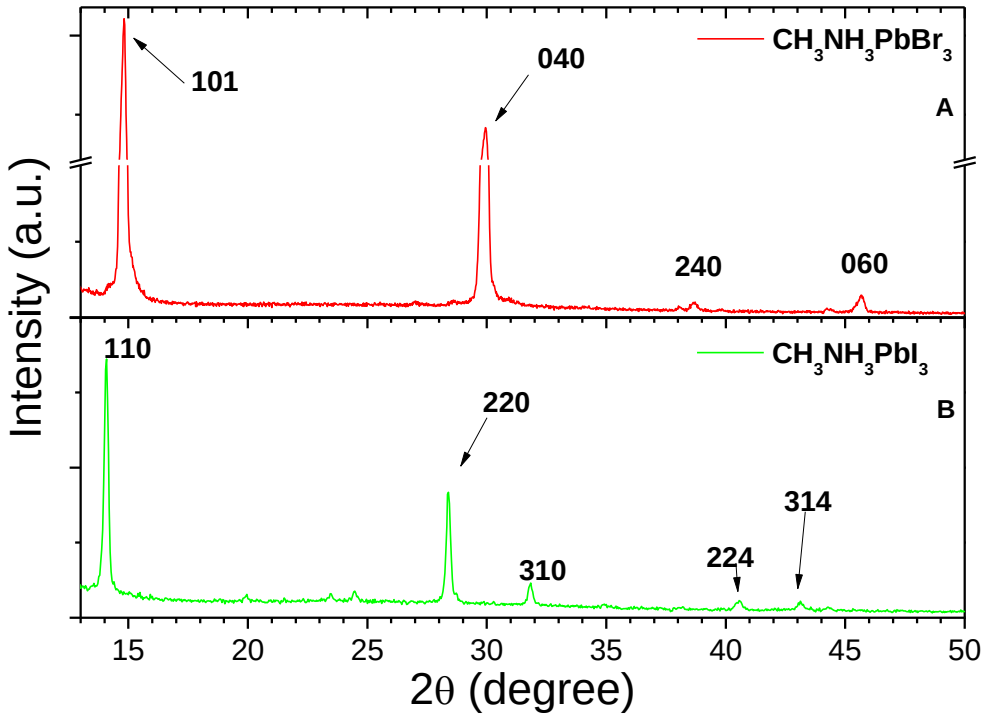

Figure 2.5| ***X-ray Diffraction patterns of $CH_3NH_3PbI_3$ (Bottom panel) and $CH_3NH_3PbBr_3$ (Top panel).*** *The samples are spin-coated on glass substrates and annealed at 100 ℃ before being measured.*

XRD patterns for $CH_3NH_3PbI_3$ thin film (figure 2.5 panel B) shows two strong diffraction peaks at 2θ angles 14.1° and 28.4°, which could be assign to (110) and (220) planes in the tetragonal lattice. And there are another 3 weak peaks at 2θ angles 31.8 °, 40.6 ° and 43.1 °, which could be assigned to (310), (224) and (314) planes for the tetragonal phase, respectively. The tetragonal perovskite structure with lattice parameters a=b=8.872 Å and c =12.637 Å, similar to the $CH_3NH_3PbI_3$ previously reported [9, 11-13].

The XRD analysis for $CH_3NH_3PbBr_3$ thin film (figure 2.5 panel A) also shows two strong diffraction peaks, which locate at 2θ angles 14.8° and 30.0°, which could be assign to (101) and (040) planes in the cubic lattice. And there are another 2 weak peaks at 2θ angles 38.7° and 45.7 °, which could be assigned to (240), (060) planes for the cubic lattice, respectively [9, 13-17]. Gary Hodes et al. [14] reported that $CH_3NH_3PbBr_3$ perovskite cubic lattice should have many XRD peaks

(PDF#01-076-2758), most of which did not appear in the diffraction patterns. And this could be explained by preferred orientation in the (101) and (240) directions.

2.2.2 Atomic force microscopy measurement

Atomic force microscopy (AFM) is a very high-resolution type of scanning probe microscopy, with demonstrated resolution on the order of fractions of a nanometer, more than 1000 times better than the optical diffraction limit. The AFM is one of the foremost tools for imaging, measuring, and manipulating matter at the nanoscale. The information is gathered by "feeling" the surface with a mechanical probe. Piezoelectric elements that facilitate tiny but accurate and precise movements on (electronic) command enable the very precise scanning. In some variations, electric potentials can also be scanned using conducting cantilevers and currents can be passed through the tip to probe the electrical conductivity or transport of the underlying surface [18].

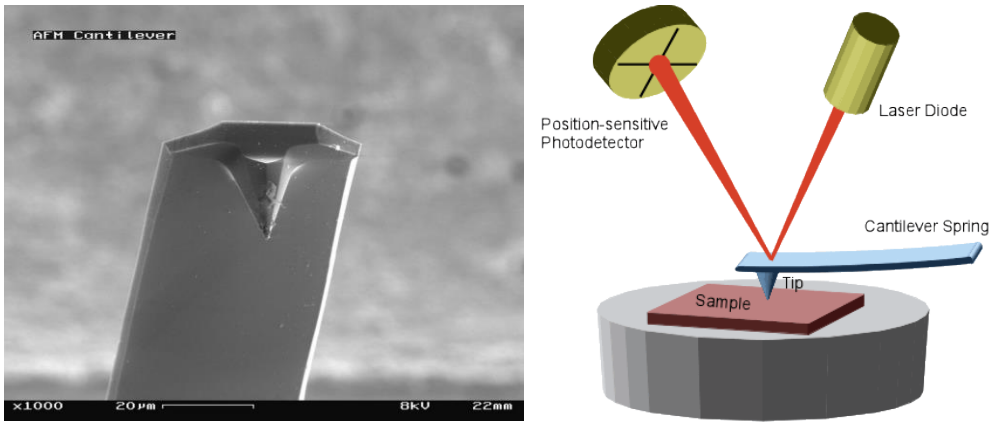

A B

Figure 2.6| *(A) The cantilever with tip of AFM; (B) bending detection.*

The AFM consists of a cantilever with a sharp tip (probe) at its end that is used to scan the specimen surface, shown in figure 2.6. The cantilever is typically silicon or silicon nitride with a tip radius of curvature on the order of nanometers. When the tip is brought into proximity of a sample surface, forces between the tip and the sample lead to a deflection of the cantilever according to Hooke's law [19]. Depending on the

situation, forces that are measured in AFM include mechanical contact force, van der Waals forces, capillary forces, chemical bonding, electrostatic forces, magnetic forces, Casimir forces, solvation forces, etc. Along with force, additional quantities may simultaneously be measured through the use of specialized types of probes. Typically, the deflection is measured using a laser spot reflected from the top surface of the cantilever into an array of photodiodes. Other methods that are used include optical interferometry, capacitive sensing or piezoresistive AFM cantilevers. These cantilevers are fabricated with piezoresistive elements that act as a strain gauge. Using a Wheatstone bridge, strain in the AFM cantilever due to deflection can be measured, but this method is not as sensitive as laser deflection or interferometry.

Basically, we can get thickness information, the morphology pictures and the roughness of the film from the AFM measurement

Figure 2.7 presents some surface images of a perovskite film. These samples are prepared by spin-coating/evaporating on glass substrates. The thickness of the films is about 100 nm.

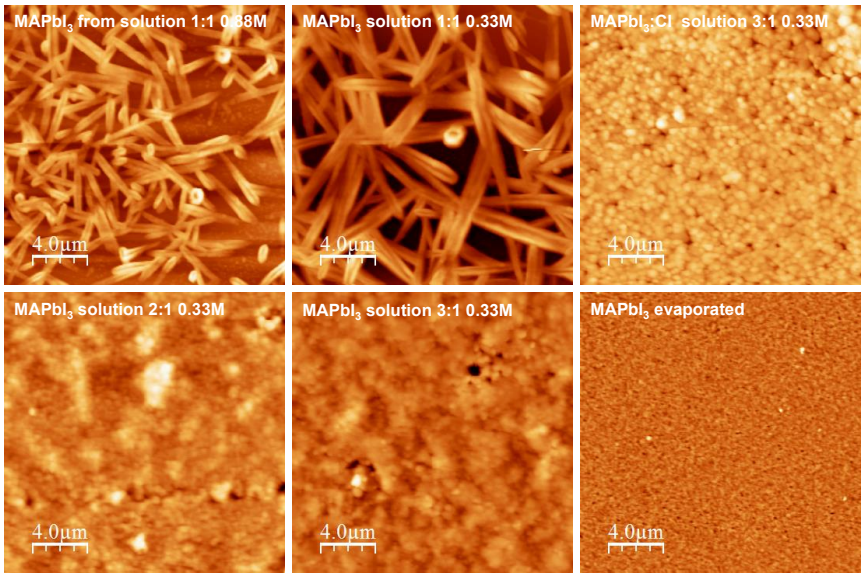

Figure 2.7| *AFM images to investigate the morphology of perovskite films.*

Standard synthesis of $CH_3NH_3PbI_3$ is obtained by mixing CH_3NH_3I and PbI_2 in solution, then spin coating on the substrate and letting the solvent evaporate; needle-shaped crystals are formed, with size dependent on the solution concentration

(first two images form left on top row). Mixing instead CH_3NH_3I and $PbCl_2$ produces essentially the same $CH_3NH_3PbI_3$ perovskite, just with some I atoms replaced by Cl; such small content of Cl atoms does not seem to alter the electronic structure, but the effects on film morphology are evident, as a smoother film with smaller grains is produced (third image from left on top row). Similar effects can be produced by change the proportion of CH_3NH_3I and PbI_2 in solution, without addition of $PbCl_2$ (first two images from left in bottom row). The smoothest film by far is however obtained with evaporation in nitrogen atmosphere (third image from left on bottom row); evaporation is realized according to the work of Yang Yang's group [21], but the difference is we put the sample face to the methyl ammonium salt instead of in the salt (Figure 2.2 part B).

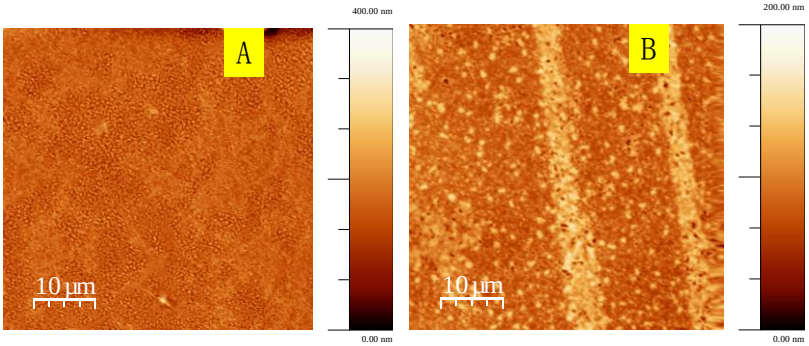

Figure 2.8| AFM images of $CH_3NH_3PbBr_3$. *Panel A shows the result $CH_3NH_3PbBr_3$ prepared from two-step spin-casting from $PbBr_2$ and CH_3NH_3Br. Panel B shows the same measurement on $CH_3NH_3PbBr_3$ with $PbAc_2$ as Pb source.*

Figure 2.8 shows the AFM measurement on $CH_3NH_3PbBr_3$. Panel A shows the result performed on the sample prepared with two-step method. The CH_3NH_3Br and $PbBr_2$ were dissolved in DMF and isopropanol, respectively. Panel B shows the AFM of perovskite prepared with two-step method too. But the Pb source is $PbAc_2$, not $PbBr_2$. The molar concentration of $PbBr_2$ and $PbAc_2$ solutions are the same, of 0.5 M. The $CH_3NH_3PbBr_3$ based on $PbBr_2$ shows crystals dispersed on the substrate; the shape of the perovskite is small dot. The $CH_3NH_3PbBr_3$ based on $PbAc_2$ shows a smooth film but with many pin-holes. That means the $PbAc_2$ would react with

CH_3NH_3Br to form a smooth perovskite film. We think the smooth film is generated by the weak van der Waals' force among the organic Ac^- groups, which makes the $PbAc_2$ always close to each other, leading to a smooth $PbAc_2$ film. And the perovskite formed from this Pb source will grow with the same trend when annealed on hotplate. It implies that it has the potential by changing the concentration of the $PbAc_2$ and the preparing conditions to get a smooth film [20].

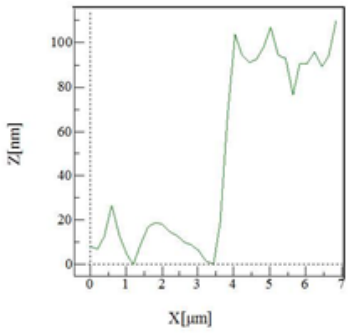

Figure 2.9| *Thickness of perovskite films with AFM data.*

The figure 2.9 shows us that the thickness of the perovskite film is around 90 nm with the roughness of 20nm. (D. Marongiu et al., in preparation.)

2.2.3 Absorption and photoluminescence spectroscopy measurement

Absorbing light is a primary property of a semiconductor material. The absorption spectrum is always used to express the absorbance process, which is the interaction between electromagnetic waves and material. In principle, we can get the band gap and the molecular structure information from the absorption spectra. For instance, the absorption spectrum can indicate the rotation and vibration information in the molecular.

The measurement is always expressed with Lamber-Beer Law (Formula 2.4):

$$A = \varepsilon lc$$

(2.4)

In the formula 2.4, the A is absorbance, ε is the attenuation coefficient of the material, l is the distance of the light travels through the material and the c is the concentration of the material.

In our lab, the absorbance spectra of perovskite films are measured with a UV/Visible Perkin Elmer Lambda 950 spectrometer (Figure 2.10 left). The wavelength range of it is from 175nm to 3300nm. That means we can investigate the UV/visible/near infrared optical properties of the material with this instrument. In this spectrometer, there are two lamps and two monochromators to generate single wavelength source light. There are two types of gratings in the spectrometer: one is 1440 grooves/mm for UV/Vis light; another one is 360 grooves/mm for near infrared light. The chopper is special designed for this spectrometer, called CSSC(Chopper Segment Signal Correction) which is utilizing four segments, one Sample, one Reference, and two Dark portions (Figure 2.10 right). The operating speed of the chopper is very high (20 millisecond measurement phase).

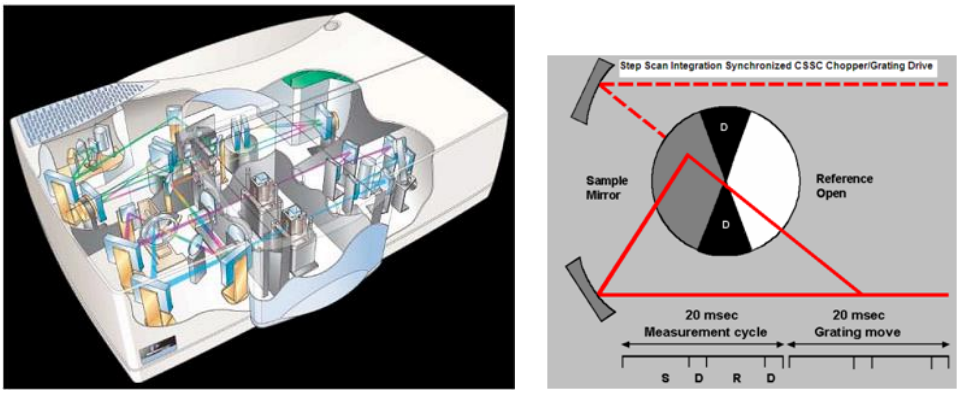

Figure 2.10 | *The diagram of Lambda 950 spectrometer (Left). The CSSC chopper in the spectrometer (Right).*

To measure the absorbance property of the perovskite thin film, we prepared $CH_3NH_3PbI_3$ and $CH_3NH_3PbBr_3$ films on quartz substrate. Clean the quartz substrate with soap water in ultrasonic bath for 5 minutes and clean with deionized water in ultrasonic bath for 5 minutes. Rinse the substrate with acetone and isopropanol and boil it in H_2O_2 for 15 minutes. Rinse with deionized water and blow with dry air. Then

prepare the $CH_3NH_3PbI_3$ sample as vapour assisted two-step method. Typical PbI_2 solution is with 0.5 M concentration in DMF, for the 1M solution always results in a ~300 nm perovskite film which is too thick for the absorbance measurement. The absorbance intensity of a thick film is always over the range of the spectrometer.

20μl poly(methylmethacrylate) (PMMA) in anhydrous chlorobenzene with concentration of 30 mg/ml was spin casted (3000 rpm, 30 s) on the $CH_3NH_3PbI_3$ film to protect the perovskite from being oxidized. The sample absorbance property was characterized with Perkin Elmer Lambda 950 with reference of a blank quartz substrate.

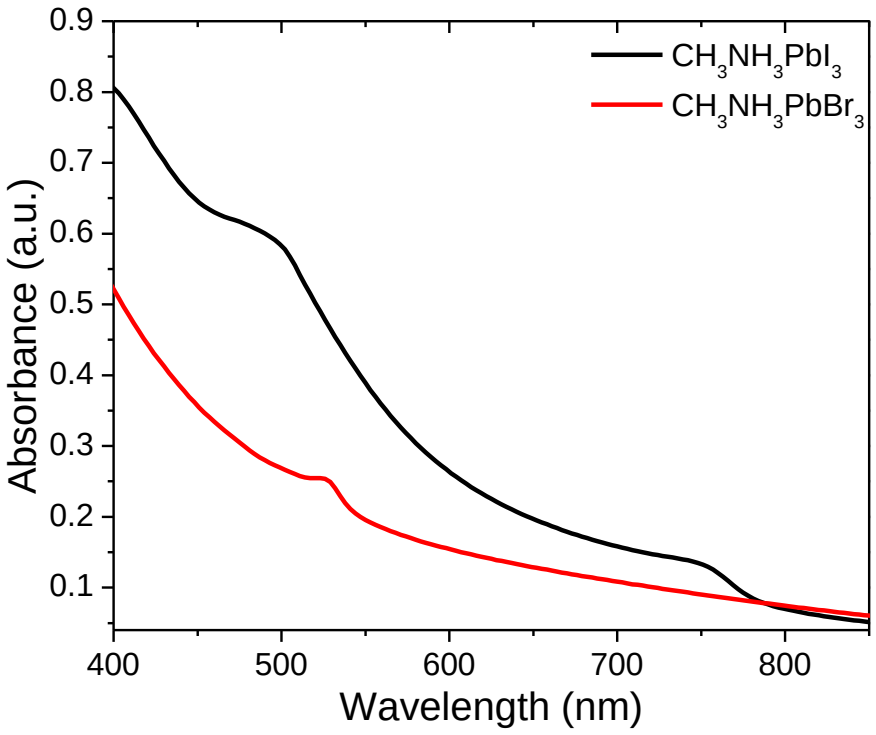

Figure 2.11| *The absorbance of $CH_3NH_3PbBr_3$ (red line) and $CH_3NH_3PbI_3$ (black line) films on quartz substrates.*

The $CH_3NH_3PbBr_3$ film was prepared according to two steps from solution. The $PbBr_2$ was dissolved in DMF to generate a 0.5M solution. 10 mg/ml CH_3NH_3Br isopropanol was used as the second spin-casting material.

Figure 2.11 shows us the result of the absorbance measurements on $CH_3NH_3PbI_3$

and $CH_3NH_3PbBr_3$ films. The $CH_3NH_3PbI_3$ result (black line) indicates that the absorption edge is 756 nm. So we can conclude that the optical band gap of the $CH_3NH_3PbI_3$ film is 1.64 eV, which is a little higher than 1.55eV reported in other works [22 - 24]. The result also shows that the absorbance is very strong even near the absorption edge, and the absorption is especially strong when the wavelength is shorter than 500 nm. If the thickness of film increases to 300nm (the thickness of $CH_3NH_3PbI_3$ perovskite film in a solar cell), the absorbance should be more efficient.

The $CH_3NH_3PbBr_3$ result (red line) indicates that the absorption edge is 535 nm, which means that the optical band gap is around 2.32 eV. This value is much higher than the calculation result which is 1.80 eV for a cubic $CH_3NH_3PbBr_3$ crystalline film performed with periodic DFT calculation [15]. But it coincides with the DFT+D2 calculation result which is 2.34 eV [16]. The same measurement performed by other groups shown the similar results.

2.2.4 FET measurement

The field effect transistor (FET) is used in our daily electronic tools. The new semiconductors applied on FET have a huge family now. And there is a standard technology to characterize the FET material.

In our lab, the measurement on FET is performed on the I-V testing system. In this system, the Keithley 2400 source meter and Keithley 6487 Pico-ampere meter are used for voltage applier and current meter respectively. The range of the gate voltage supplied by Keithley 2400 is from -100 V to 100 V. The lowest current value we can get from Keithley 6487 is ~10^{-12} A, but the current we get was always much higher than the limited.

Figure 2.12 shows the schematic diagram of a FET measurement. The perovskite was prepared on an interdigitated electrode which is gold with the height of 50 nm. The electrodes are deposited on a dielectric SiO_2 substrate, with the SiO_2 of 100nm. The gate substrate is n-type Si. The FET interdigitated substrate was protected by a layer of photo resist. So we need to rinse it with acetone and isopropanol two times

before depositing perovskite film. The depositing method was vapour assisted two-step from spin-casting 0.3M PbI_2 in DMF solution and evaporating CH_3NH_3I salt. The needle probes were used to apply voltage and measure the current between drain and source.

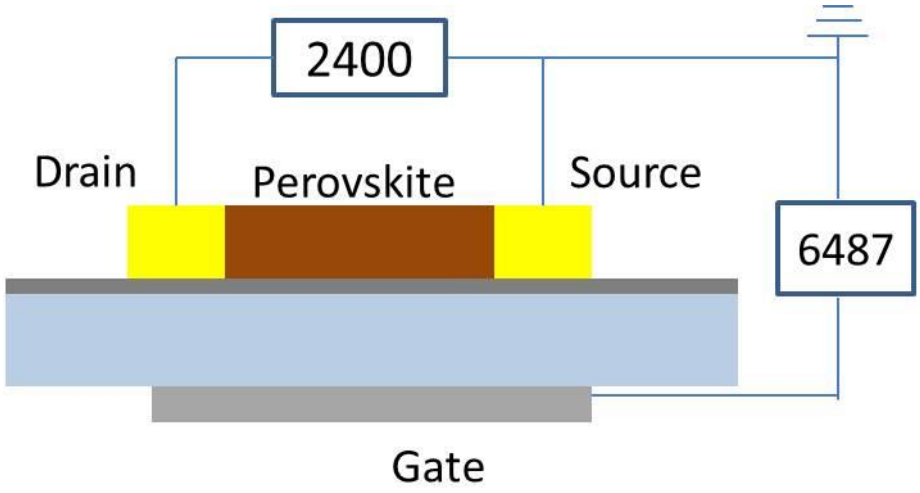

Figure 2.12| FET schematic diagrams. *The drain and source electrodes are made of gold with the height of the gold contacts is 50 nm. The dielectric layer is 100nm SiO_2. Gate material is n-doped Si. The distance between the drain and source are 2.5μm, 5μm, 10μm, and 20μm, differently.*

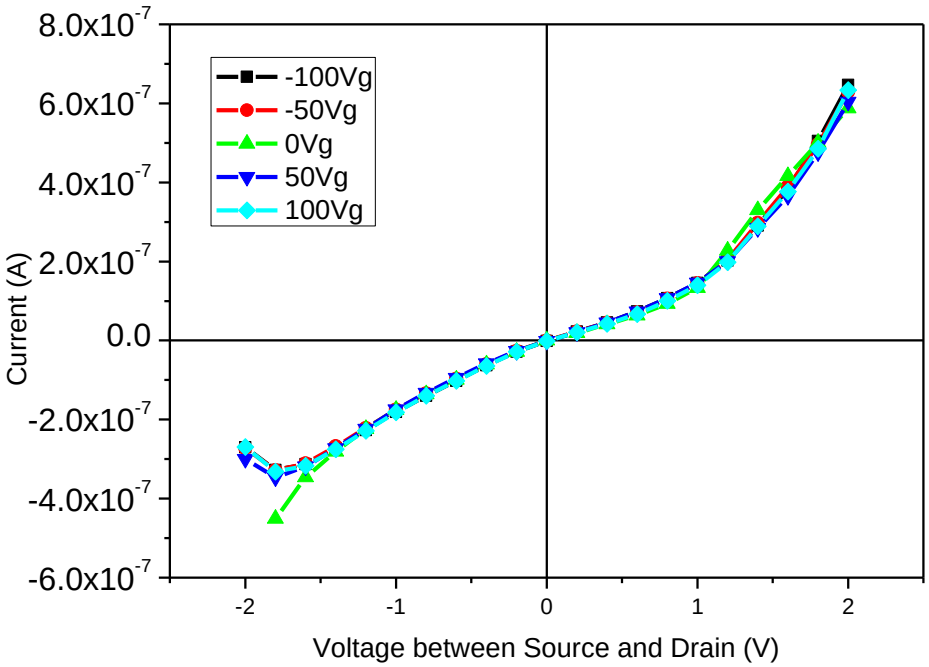

Figure 2.13| FET measurements on perovskite. *The distance between the drain and source is 10μm.*

Figure 2.13 shows the FET measurement result on perovskite. Unfortunately, we cannot get any information from this kind of measurement. The current between the drain and source is stable with the gate variation.

Reference

[1]. Xing, N. Mathews, S. Sun, S. S. Lim, Y. M. Lam and M. Grätzel; "Long-Range Balanced Electron- and Hole-Transport Lengths in Organic-Inorganic $CH_3NH_3PbI_3$", ***Science,*** 2013, 342, 344.

[2]. J. J. Choi, X. Yang, Z. M. Norman and S. J. L. Bilinge; "Structure of Methylammonium Lead Iodide within Mesoporous Titanium Dioxide: Active Material in High-Performance Perovskite Solar Cells", **Nano Lett.** 2014, 14, 127.

[3]. B. Conings, L. Baeten, and C. Dedobbelaere; "Perovskite‐Based Hybrid Solar Cells Exceeding 10% Efficiency with High Reproducibility Using a Thin Film Sandwich Approach", ***Adv. Mater.*** 2014, 26, 2041.

[4]. J. T. Wang, J. M. Ball, E. M. Barea and A. Abate et al, "Low-temperature processed electron collection layers of Graphene/TiO_2 nanocomposites in thin film perovskite solar cells", ***Nano Lett.*** 2014, *14*, 724

[5]. Z. Xiao, Q. Dong, C. Bi, Y. Shao, Y. Yuan and J. Huang; "Solvent Annealing of Perovskite‐Induced Crystal Growth for Photovoltaic‐Device Efficiency Enhancement", ***Adv. Mater.*** 2014, 26, 6503.

[6]. T. Baikie, Y. Fang, J. M. Kadro, M. Schreyer, F. Wei, S. G. Mhaisalkar, M. Grätzel and T. J. White, "Synthesis and crystal chemistry of the hybrid perovskite (CH_3NH_3) PbI_3 for solid-state sensitised solar cell applications", ***J. Mater. Chem. A***, 2013, 1, 5628.

[7]. Richard Tilley; "Crystals and crystal structures", Chapter 6 "Diffraction and crystal structures", John Wiley & Sons Ltd, 2006.

[8]. Lee M. M, Teuscher J, Miyasaka T, Murakami T. N. and Snaith H. J.; "Efficient Hybrid Solar Cells Based on Meso-Superstructured Organometal Halide Perovskites", ***Science,*** 2012, 338,643.

[9]. A. Poglitsch and D. Weber; "Dynamic disorder in methylammoniumtrihalogeno-plumbates (II) observed by millimeter‐wave spectroscopy", ***J. Chem. Phys.*** 1987, 87, 6373.

[10]. Park N.-G. "Organometal Perovskite Light Absorbers. Toward 20% Efficiency Low-Cost Solid-State Mesoscopic Solar Cell", ***J. Phys. Chem. Lett.*** 2013, 4, 2423.

[11]. Jeng J. Y., Chiang Y. F., Lee M. H. and Peng S. R.; "$CH_3NH_3PbI_3$ Perovskite/ Fullerene Planar‐Heterojunction Hybrid Solar Cells", ***Adv. Mater.*** 2013, 25, 3727.

[12]. J. H. Im, C.R. Lee, J. W. Lee, S. W. Park and N. G. Park; "6.5% efficient perovskite quantum-dot-sensitized solar cell", ***Nanoscale***, 2011, 3, 4088.

[13]. J. Qiu, Y. Qiu, K. Yan, M. Zhong, C. Mu, H. Yan and S. Yang; "All-solid-state hybrid solar cells based on a new organometal halide perovskite sensitizer and one-dimensional TiO_2 nanowire arrays", ***Nanoscale***, 2013, 5, 3245.

[14]. E. Edri, S. Kirmayer, D. Cahen, G. Hodes, "High Open-Circuit Voltage Solar Cells Based on Organic–Inorganic Lead Bromide Perovskite", ***J. Phys. Chem. Lett.*** 2013, 4, 897.

[15]. E. Mosconi, A. Amat, M. Nazeeruddin, M. Grätzel, F. Angelis, "First-Principles Modeling of Mixed Halide Organometal Perovskites for Photovoltaic Applications", ***J. Phys. Chem. C***, 2013, 117,13902.

[16]. J. Feng, B. Xiao, "Crystal Structures, Optical Properties, and Effective Mass Tensors of $CH_3NH_3PbX_3$ (X= I and Br) Phases Predicted from HSE06", ***J. Phys. Chem. Lett.*** 2014, 5, 1278.

[17]. J. Noh, S. Im, J. Heo, T. Mandal, S. Seok, "Chemical Management for Colorful, Efficient, and Stable Inorganic-Organic Hybrid Nanostructured Solar Cells", ***Nano Letters***. 2013, 13, 1764.

[18]. P Eaton and P West, "Atomic force microscopy" Oxford University Press, 2010

[19]. B. Binnig, C. F. Quate, and C. Gerber, "Atomic force microscope", ***Phys. Rev. Lett.*** 1986, 56, 930.

[20]. a) A. Buin, P. Pietsch, J. Xu, O. Voznyy, A.H. Ip, R. Comin, E.H. Sargent, "Materials Processing Routes to Trap-Free Halide Perovskites", ***Nano Lett.*** 2014, 14, 6281.

b) S. Stranks, P. Nayak, W. Zhang, T. Stergiopoulos, H. Snaith, "Formation of

Thin Films of Organic–Inorganic Perovskites for High‐Efficiency Solar Cells", ***Angew. Chem. Int. Ed.*** DOI: 10.1002/anie.201410214.

[21]. Q. Chen, H. Zhou, Z. Hong, S. Luo, H. Duan, H. Wang, Y. Liu, G. Li and Y. Yang; "Planar Heterojunction Perovskite Solar Cells via Vapour-Assisted Solution Process", ***J. Am. Chem. Soc.*** 2014, 136,622.

[22]. Y. S. Kwon, J. Lim, H. J. Yun, Y. H. Kim, and T. Park, "A diketopyrrolopyrrole-containing hole transporting conjugated polymer for use in efficient stable organic–inorganic hybrid solar cells based on a perovskite ", ***Energy Environ. Sci.*** 2014, 7, 1454.

[23]. P. W. Liang, C. C. Chueh, X. K. Xin, F. Zuo, S. T. Williams, C. Y. Lial, and A. K.-Y. Jen, "High-Performance Planar-Heterojunction Solar Cells Based on Ternary Halide Large-Band-Gap Perovskites", ***Adv. Energy Mater.*** 2015, 5, 1400960.

[24]. N. Kitazawa, Y. Watanabe, Y. Nakamura, "Optical Properties of $CH_3NH_3PbX_3$ (X= Halogen) and Their Mixed-Halide Crystals", ***Journal of Materials Science***. 2002, 37, 3585.

CHAPTER 3
Basic properties of organo-lead halide perovskite

The study of the basic properties of methylammonium lead halide perovskites, which demonstrate excellent photovoltaic performance in solar cells, helps to understand their charge photogeneration and recombination mechanisms and unravels their potential for other optoelectronic applications. In this chapter, we investigate the basic properties of the $CH_3NH_3PbI_3$ ($MAPbI_3$) perovskite, including the morphology of the films from different preparing method, the XRD analysis in the reacting stages and the photophysical properties, to improve the device performance and develop new applications.

3.1 Introduction

Organic-inorganic hybrid perovskites are a technologically important class of materials, offering the possibility of combining useful properties of both organic and inorganic components within a single crystalline molecular scale composite. The outstanding optical and electrical properties of perovskites make it attractive on a number of applications, such as lasing effects [1-5], light-emitting devices [6,7], field effect transistors [8-10], and especially applied on solar cells as absorbers [11-22]. In the past 5 years, the solar cells based on organo-lead halide perovskites have been put on record for power conversion efficiencies (PCE) from 3.8% to certified 20.1% (Datum is collected by National Renewable Energy Laboratory (NREL) "best research-cell efficiencies" chart). So, the perovskite solar cell is the fastest-advancing solar technology to date. The best performance of the perovskite solar cells even exceeds the best performance of multicrystalline silicon solar cell whose best performance is 20.4%. In the organometal halide perovskite family, $CH_3NH_3PbI_3$ is the most popular one and great efforts to research on $CH_3NH_3PbX_3$ (X=Cl, I, Br) are made in many groups [11, 21, 23]. However, the understanding of the mechanisms underlying such exceptional performance has not grown at the same pace.

Writing in Science, the group of Snaith [24] at the University of Oxford reported a perovskite based solar cell with a structure of FTO/compact TiO_2/mesoporous Al_2O_3 (or TiO_2)/$CH_3NH_3PbI_2Cl$/spiro-OMeTAD/Ag. They obtained a PCE of 10.9% for the mesoporous Al_2O_3 based device and a PCE of 7.6% for the mesoporous TiO_2 based device. They investigated the XRD patterns with the $CH_3NH_3PbI_2Cl$ perovskite, resulted a similar structure as $CH_3NH_3PbI_3$ perovskite. In later research [25, 26], they reported a planar architecture (FTO/PEDOT:PSS/$CH_3NH_3PbI_{3-x}Cl_x$/PCBM/TiO_x/Al) with PCE up to 10%. Detailed analytical investigations on various device architectures found the ratio of the chlorine in the perovskite inconsistent with and much lower than the value of one third prescribed by the formula $CH_3NH_3PbI_2Cl$. The Cl deficit could be explained as follows: Cl atoms from $PbCl_2$ could react with the methylammonium iodide and the methylammonium chloride easily evaporated and is

lost from the film while annealed at 100 Celsius. In most perovskite films, the chlorine content was even less than 1% in the halide element [27]. For such reason the XRD patterns for $CH_3NH_3PbI_{3-x}Cl_x$ are very similar to $CH_3NH_3PbI_3$ ones. Zhao's group articulated that the chlorine content present in $CH_3NH_3PbI_{3-x}Cl_x$ should be very low because the lattice distortion induced by Cl atoms will cause shift and broadening of the XRD peaks if the Cl ratio is too high in the perovskite film. That indicates the chlorine element should be only a small amount in the perovskite to ensure the lattice crystalline [28].

To understand the underlying mechanism that leads to such exceptional performance of solar cells, the time-resolved photoluminescence study by Snaith et al. [29] and Mathews, Sum and collaborators [30] independently report on diffusion-length measurements performed on hybrid perovskites, which shed light on the dynamics of photo excited species (excitons or charge carriers) in these materials. Both teams obtain diffusion lengths exceeding 100 nm for electrons and holes in $CH_3NH_3PbI_3$ films. And especially, the research of Snaith group investigated the mixed halides perovskite indicating that the $CH_3NH_3PbI_{3-x}Cl_x$ perovskite films prepared from the $CH_3NH_3I/PbCl_2$ precursors exhibit longer charge carrier diffusion lengths (around 1 micrometre) as compared to those films prepared from the CH_3NH_3I/PbI_2 (around 100nm). Huang J. et al. [32] report in Science that the diffusion lengths in $CH_3NH_3PbI_3$ single crystals grown by a solution-growth method can exceed 175 μm under 1 sun illumination and exceed 3 mm under weak light for both electrons and holes. The long-range diffusion length ensures the possibility to fabricate devices with optically thick active layers, where the absorption of light can be increased without affecting the collection efficiency of the generated charges [25, 33].

For the fundamental aspects of the organometal halide perovskites, Listorti and his collaborators [34] reported a function of Cl element in $CH_3NH_3PbI_{3-x}Cl_x$ perovskite. Although the perovskite lattice and band gap remains unchanged with respect to $CH_3NH_3PbI_3$, the Cl doping dramatically improves the charge transport within the perovskite layer, explaining the outstanding performances of

meso-superstructured solar cells based on $CH_3NH_3PbI_{3-x}Cl_x$ perovskite. In our group, Saba et al. use photoluminescence and transmission spectroscopy to show that photoexcitations give rise to conducting plasma of unbound but Coulomb-correlated electron-hole pairs at all excitations of interest for light-energy conversion [35], which ensures efficient charge separation and ambipolar transport in solar cells. And it provides a low threshold for light amplification and justifies a favourable outlook for the demonstration of an electrically driven laser.

In this chapter, I will introduce some basic properties of the $CH_3NH_3PbI_3$ perovskite, including the morphology of the films from different preparing method, the XRD analysis in the reacting stages and the photophysical properties, to improve the device performance and develop new applications.

3.2 Experimental

3.2.1 Sample preparation

The $CH_3NH_3PbI_3$ ($MAPbI_3$) perovskite samples in the experiments were prepared in our lab. The perovskite could be fabricated by 3 different methods from methylamine iodide (MAI) and PbI_2 (or $PbCl_2$). CH_3NH_3I and $CH_3NH_3PbI_3$ were synthesized according to the formula 3.1 and 3.2, respectively.

$$CH_3NH_2 + HI = CH_3NH_3I \tag{3.1}$$

$$CH_3NH_2I + PbI_2 = CH_3NH_3PbI_3 \tag{3.2}$$

The details of preparing procedures were described in chapter 2.1. Specifically, the organic salt MAI was purified before being used to synthesize perovskite, by heating at 150 ℃ in N_2 filled glove box. After 14 hours heating process, the salt was truly white without any yellow colour left.

3.2.2 X-ray diffraction and Atomic force microscopy

Structural characterization was carried out by analysing the X-ray diffraction patterns recorded by a Bruker D8-Discover diffractometer for thin films with parallel beam geometry and Cu Kα wavelength. Symmetric ω-2θ scans were obtained using a step size of 0.02 ° and time per step of 4 s. The samples for XRD measurement are prepared on glass or silicon substrate. We prepare some different samples for the measurements. The simplest one is $MAPbI_3$ film prepared on a glass substrate with single step spin-casting method. The MAI and PbI_2 (molar ratio of 3:1) mixing solution in DMF with final lead iodide concentrations of 0.88M is used for single step spin-casting method. The two-step solution method and vapour assisted two-step method are used to prepare the samples. Especially, samples from vapour assisted two-step method are investigated systemically. The samples from vapour assisted two-step method should be heated at 150 ℃ about 14 hours on hotplate. We investigate the PbI_2 film in different intermediate heating time. The sample without rinsed with isopropanol is investigated by XRD to check the function rinsing treatment.

Film thickness and surface morphology were obtained by AFM with a NT-MDT Solver P47H-Pro in semicontact mode by a high-resolution non-contact silicon tip. Especially, samples from vapour assisted two-step method are investigated systemically. The RMS roughness of PbI_2 and $CH_3NH_3PbI_3$ are quite different from different conditions.

3.2.3 Absorption and photoluminescence

The samples for linear absorption and photoluminescence are prepared on 15×20mm glass substrates whose thickness is 1 mm.

Absorbance spectra of perovskite films are measured with a UV/Visible Perkin Elmer Lambda 950 spectrometer, which has the adequate spectral range for $CH_3NH_3PbI_3$ perovskites with 1.55eV bandgap [24, 35]. The wavelength range we choose for perovskite is from 400nm to 850nm (~1.45eV). An alternate setup was

employed to monitor optical absorption as a function of temperature in the spectral region near the optical gap: films were kept in vacuum inside a cold finger cryostat and illuminated by an incandescent tungsten lamp through parabolic mirror optics. An optical chopper was used to modulate the light intensity in time. The transmitted light was dispersed with a grating spectrometer (Acton 2300 series with a 50 g mm^{-1}, 600 nm blaze grating) and detected by a diode and a lock-in amplifier tuned to the optical chopper frequency. The temperature was varied using liquid nitrogen as a coolant.

Contrary to the absorption process, the luminescence is a phenomenon when the materials transit from high energy state to lower energy state emitting ultraviolet, visible or infrared photons. The emission spectrum is always used to express this process [36].

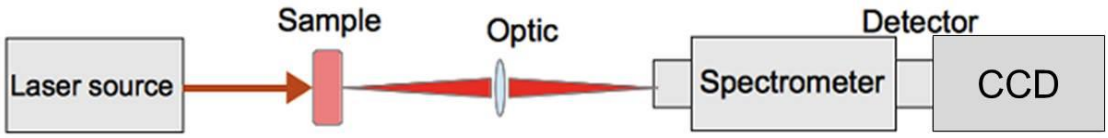

Figure 3.1| *Schematic diagram of the photoluminescence setup.*

In the photoluminescence experiment, the set-up is a custom-made system (figure 3.1) in our laboratory. A Nd:Yag cw laser (Spectra Physics Millennia series), 532 nm in wavelength, is used as the excitation source for the photoluminescence setup. The laser light was sent by means of an optical system that allows focusing on the sample in the study. When the electron-hole pair recombined between the excited state and the ground state after excited, photons would be emitted by the sample. The photoluminescence was collected by an appropriate optical configuration and acquired by the detection system. The detection system is composed of a grating spectrometer (Acton 2500 series, 600 g mm^{-1} grating, 500 nm blaze) coupled to a liquid nitrogen cooled CCD camera (Princeton Instruments). The spectrometer spectrally resolves the optical signal while the streak camera temporally resolves the optical signal.

3.2.4 Ultrafast optical spectroscopy

Ultrafast optical spectroscopy is a technique for probing and characterizing the electronic and structural properties of short-lived excited states. From the different process of the material, we can divide the ultrafast optical spectroscopy techniques we have employed into transient absorption spectroscopy and time-resolved photoemission spectroscopy.

Time-resolved photoluminescence spectroscopy

Time-resolved photoluminescence uses a pulsed laser source to promote electrons from the ground state to an excited state. The system stays in an excited state after absorbing the laser pulse; and then the system relaxes emitting optical radiation or photoluminescence. The photoluminescence signal provides a lot of information on the electronic and optical properties of the nano-crystal. Part of the information is derived from the spectral analysis, the wavelength of optical emission is correlated with band gap and consequently with the size of the nano crystal also we can investigate the different excitonic states and trap states which correspond to significant shifts in wavelength. Another part of the information is derived from the temporal analysis of the photoluminescence. In fact, the decay time of the light signal is different with different excitonic states and trap states, so we can investigate the dynamics of the charges processes.

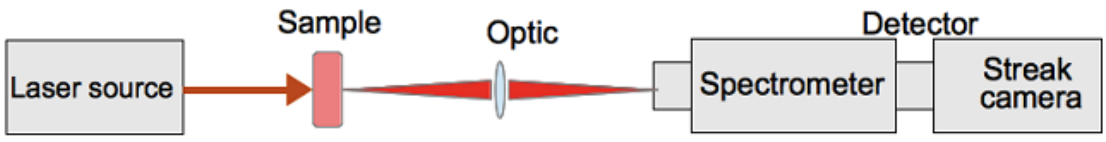

Figure 3.2| *Schematic diagram of the time-resolved photoluminescence setup. A streak camera was used as detector.*

Figure 3.2 shows the schematic diagram of experimental setup for time-resolved photoluminescence. This setup is similar to the linear luminescence setup with a

streak camera instead of CCD. A laser pulse train from laser source is sent by means of an optical system that allows an appropriate focusing on the sample in the system. Each pulse is absorbed in a very short time and provides energy and creates an excited state in the sample. Photoluminescence emitted by the sample between one pulse and the next is collected by an appropriate optical configuration and acquired by the detection system. The detection system is composed of a spectrometer coupled with a streak camera. The spectrometer spectrally resolves the optical signal while the streak camera temporally resolves the optical signal. And the final result is obtained a spectrogram with the spectral and temporal properties of nano crystals under investigation.

3.3 Results

3.3.1 Structure research with XRD

Figure 3.3 shows the XRD patterns of the perovskite films. All the films in this figure are prepared by standard methods we demonstrated before. A is prepared with vapour assisted two-step method. 1M PbI_2 is used to prepare PbI_2 film, and MAI is evaporated to PbI_2 film under N_2 atmosphere. After the evaporation procedure, 2-propanol is utilized to rinse the film, and then thermal treated at 100 Celsius. B is prepared with two-step method from 1M PbI_2 in DMF solution and 10mg/ml MAI in anhydrous isopropanol. C is prepared with single spin-casting the mixing solution of MAI: PbI_2=3:1 in DMF. In the figures, we can see 3 strong peaks located at the 2θ angles 14.08 °, 28.36 ° and 31.84 °, which can be assigned to (110), (220), (310) planes of $MAPbI_3$ tetragonal structure [25, 28, 38]. In the figure A and figure C, we cans see 3 weak peaks at 2θ angles of 19.96 °, 23.44 °, 24.48 ° and 40.56 °, which can be assigned to (112), (211), (202) and (224) planes of $MAPbI_3$ tetragonal structure. The results indicate that we can get tetragonal $MAPbI_3$ perovskite from any method.

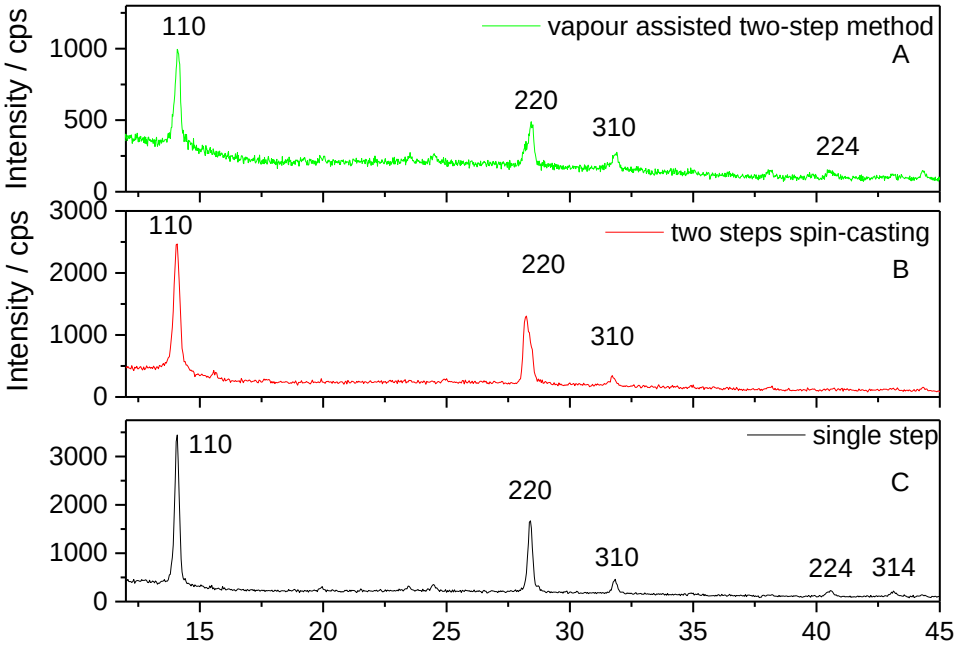

Figure 3.3| XRD patterns of the perovskite films. *A is the perovskite prepared with vapour assisted two-step method. B is prepared with two steps spin-casting from solution. C is prepared with single spin-casting method from a mixing solution of MAI and* PbI_2.

Figure 3.4 shows the XRD patterns of perovskite films prepared with vapour assisted two-step method. Simultaneously, The PbI_2 film heated in MAI atmosphere only 2 hours，the PbI_2 film heated in MAI atmosphere 14 hours without isopropanol washing and the MAI powder are investigated with XRD ether. The cyan line (top) in the figure 3.4 is the XRD patterns of the MAI powder. The data show us that there are two strong peaks at 2θ angle 19.66 °and 29.64 °, and 3 weak peaks between 2θ angle of 10 °and 35 °. We know that there is a strong peak at 2θ angle of 12.6 °in the PbI_2 XRD patterns [39-42]. The PbI_2 film heated 2 hours in MAI atmosphere at 150 ℃ (blue line) shows a strong PbI_2 peak at 2θ angle of 12.6 °, and two weak peaks at 14.08 ° and 31.76 °which can be assigned to $MAPbI_3$ perovskite. The result indicates that 2 hours in MAI atmosphere is not enough to make PbI_2 film react with MAI completely, but we can see some of PbI_2 have reacted with MAI to form $MAPbI_3$ perovskite. The sample that heated in MAI atmosphere for 14 hours without rinsing with anhydrous

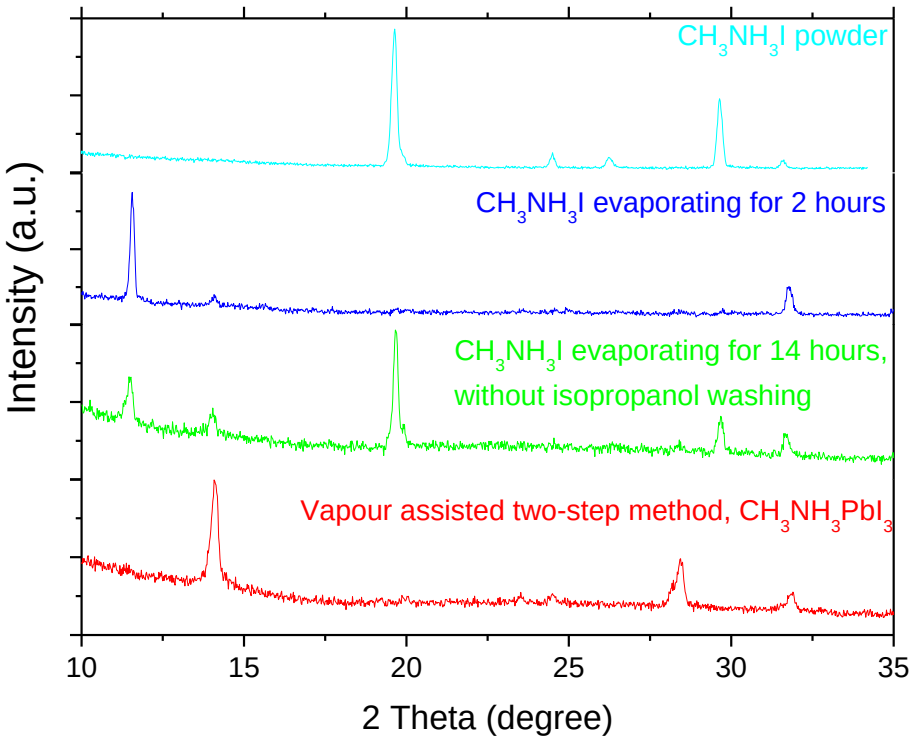

Figure 3.4| XRD patterns of the perovskite films. *The samples are prepared with vapour assisted two-step method. The cyan line is CH_3NH_3I powder on glass substrate. The blue line is the PbI_2 film heated in CH_3NH_3I petri dish at 150 ℃ for 2 hours. The green line is the PbI_2 film heated in CH_3NH_3I petri dish at 150 ℃ for 14 hours, without rinsing with isopropanol. The red line is a $CH_3NH_3PbI_3$ perovskite prepared with our standard vapour assisted two-step method. The black star means the peak is assigned to PbI_2. The blue pentagram and red cross mean the peaks are assigned to CH_3NH_3I and $CH_3NH_3PbI_3$, respectively.*

isopropanol (green line) shows a weak PbI_2 peak and a strong MAI peak at 19.66°. Two weak peaks assigned to perovskite could be found in the green line, which indicates that there are MAI, PbI_2 and $MAPbI_3$ perovskite in this sample. The red line shows an XRD pattern of a sample prepared with our standard vapour assisted two-step method, which means the sample is rinsed with anhydrous isopropanol and annealed at 100 ℃ for 1 hour. In this XRD pattern, we can see only perovskite XRD peaks without PbI_2 and MAI peak, which means that all the PbI_2 in the sample are

reacted with MAI to for perovskite, and the excess MAI are removed by isopropanol. The blue line tells us that the MAI cannot react with PbI_2 completely without the isopropanol rinsing even heated in MAI for 14 hours. So we can explain as the isopropanol can dissolve the MAI powder on top of PbI_2 film to form a MAI/isopropanol solution which could be infiltrated to the PbI_2 position. After the annealing procedure, the excess MAI and isopropanol in the film are taken away, leading a pure perovskite on the substrate.

3.3.2 Morphology research with AFM

Figure 3.5 shows the AFM measurement results on perovskite films. Part A shows the AFM measurement on perovskite prepared from full solution spin-casting. The mixing of MAI and PbI_2 in DMF was utilized to prepare a perovskite film by spin-casting at 3000 rpm. After annealing at 100 ℃ for 1 hour, needle-shaped crystals are produced, forming a partial surface coverage and limited conductivity, leading to the morphology not proper for a planar solar cell. The two steps from solution method is based on spin casting a PbI_2 film first, then spin cast a CH_3NH_3I solution on top of the PbI_2 layer, creating the perovskite upon reaction of the two compounds. The result is a film with smaller grains and more uniform coverage than film from single step (figure 3.5 B). But we can see some unexpected aggregation on top of the film, which could take fatal defects to the device [43-45]. Finally, the vapour assisted method, where a PbI_2 film is first obtained by spin-casting from solution, then evaporation of CH_3NH_3I occurs for several hours in N_2 atmosphere. A very smooth perovskite film is obtained after rinsing the film with isopropanol and annealing (figure 3.5 C), with a RMS roughness of 38 nm. Within the vapour assisted method we study how different PbI_2 solution temperature can affect the final perovskite film morphology. We used standard 70 ℃ PbI_2 solution and different intermediate temperature until we reached a metastable room temperature transparent solution. With the room temperature PbI_2 deposition we can achieve a perovskite film with a RMS roughness lower than 25 nm with a very low pin-hole density that can improve the cell efficiency within the planar

architecture (figure 3.5 D) [46, 47].

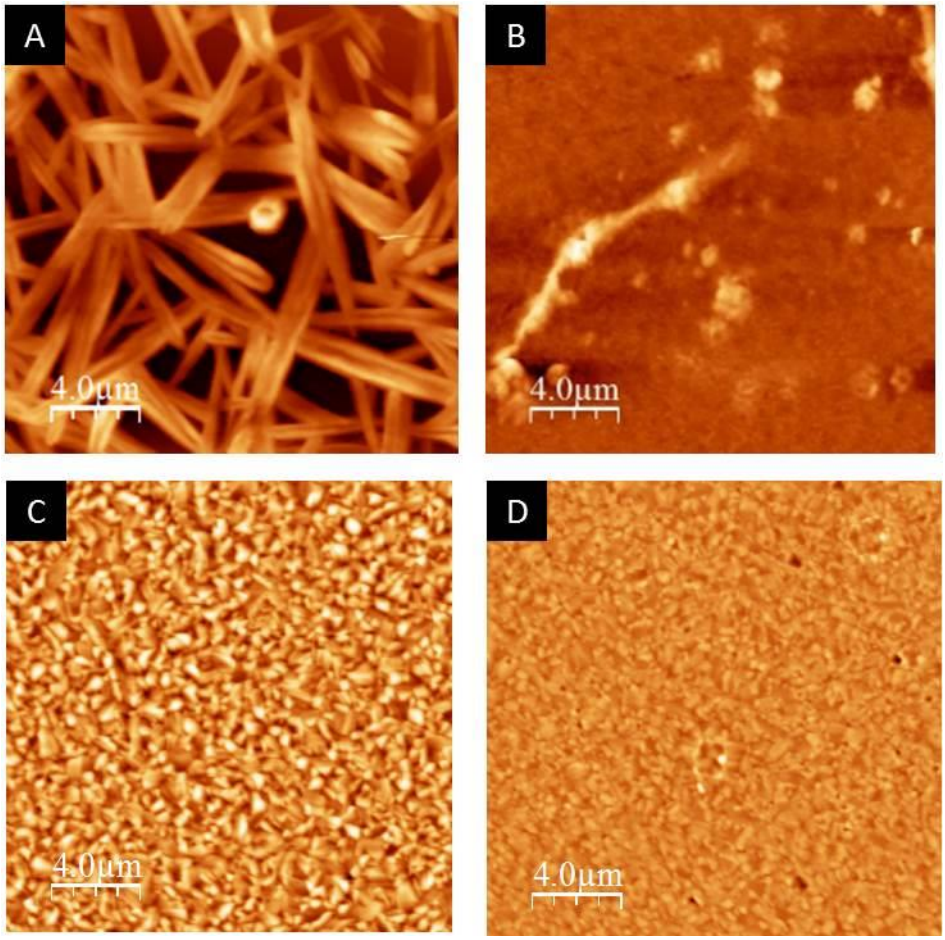

Figure 3.5| AFM measurements on perovskite films. *A): the needle-shaped perovskite crystal obtained from full solution spin-casting. B): the perovskite film fabricated by two steps from solution. C): the uniform perovskite film prepared from vapour assisted two-step method. D): the uniform perovskite film prepared from vapour assisted method with PbI_2 film deposited at room temperature.*

The solar cells based on $CH_3NH_3PbI_3$ perovskite prepared with different methods are shown in chapter 4. In general, the devices with great performance are always based on the perovskite from vapour assisted two-step method. The investigation on PbI_2 film prepared at room temperature is only starting; we will realize the device application in the follow-up work.

3.3.3 The visible/near-infrared absorption

Figure 3.6 shows the visible/near-infrared absorption spectra of $MAPbI_3$ perovskite films on glass substrate at room temperature. The samples are prepared with different methods. The single step spin-casting method was used to prepare a film from a mixing solution. The ratio of MAI: PbI_2 was 3:1 in the DMF solvent, and the PbI_2 concentration was 1M in the solution. The concentration of PbI_2 used to prepare PbI_2 film was 1M in anhydrous DMF, which was utilized for vapour assisted method either. Samples from vapour assisted two-step method were heated in MAI atmosphere at 150 ℃ for 14 hours.

PbI_2 film absorbance is shown in figure 3.6 (black line), indicating that the optical band gap is around 2.48 eV, which should be higher than 2.31 eV reported in other group [48-51].

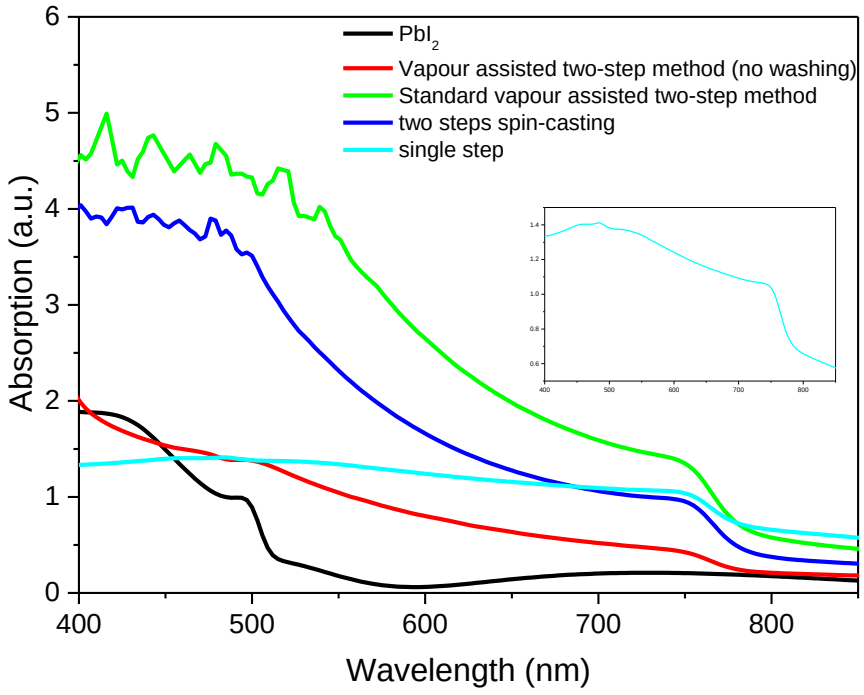

Figure 3.6| Visible/near-infrared absorption of perovskite films. *The samples are prepared with different method. The black, red, green, blue and cyan lines are the absorption of PbI_2 film, perovskite with vapour assisted method without isopropanol*

rinsing, the perovskite with our standard vapour assisted method, the perovskite prepared with two steps spin-casting method, and the perovskite prepared with single spin-casting of mixing solution, respectively.

The cyan line in figure 3.6 shows absorbance of a sample prepared with single step spin casting method. It indicates that a sharp absorption edge at 752nm which belongs to a $MAPbI_3$ optical band gap [35]. We can see a long-wavelength tail from this absorbance curve, which can be explained from the scattering of the film. This result coincides with the AFM measurement on a similar sample from single step method, which shows the bad coverage on the substrate (figure 3.5 part A). The measurements on the samples prepared with two steps spin casting method (blue line) and vapour assisted two-step method (green line) indicate that the optical band gap of $MAPbI_3$ is around 1.6 eV and, for the thicknesses we realized, the absorption coefficient of the perovskite is always higher than 10^5 cm^{-1} while the wavelength shorter than 500nm and the absorption coefficient is $\sim 4 \times 10^4$ cm^{-1} even at the absorption edge. That is to say, the perovskites from both methods could be used for photovoltaic devices according to the absorption properties. Measurement performed on a sample prepared with vapour assisted two-step method without isopropanol rinsing shows the similar result as XRD measurement (chapter 3.3.1). The absorbance (red line) of this sample shows perovskite absorption property and PbI_2 property together, and the absorption assigned to perovskite is much weaker than the washing one.

3.3.4 Transient photoluminescence spectroscopy

The perovskite is a hybrid, partly organic and partly inorganic compound; it is not clear in principle whether the excited-state dynamics will be dominated by excitonic effects, as in organic semiconductors [52], or by an electron–hole plasma, as happens in the inorganic compounds. And it is an important issue to understand the excited-state properties of perovskite [53, 54]. Here we investigate the nature of the

excited state in organometal halide perovskites with transient photoluminescence spectroscopy.

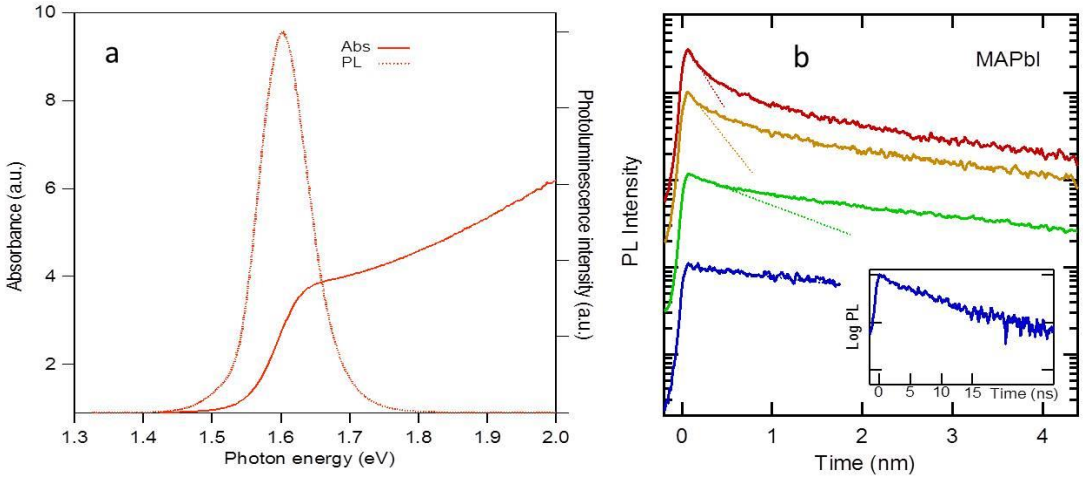

Figure 3.7| Absorption and photoluminescence spectra and transient photoluminescence spectroscopy in trihalide perovskite films. *(a) Visible–near-infrared absorption (continuous line) and luminescence (dashed line) spectra of a $MAPbI_3$ film (thickness, 800 nm) recorded at 300 K. Spontaneous emission was excited by a green laser (λ=532 nm) operating in continuous wave (cw). (b) Transient photoluminescence signal as a function of the injected electron-hole pair density at the film surface (n_0). Straight lines in the semi-logarithmic plot represent an exponential fit to the initial decay of the photoluminescence signal. Photoluminescence was excited by 150-fs-long laser pulses with a repetition rate of 1 kHz and 3.18eV photon energy. At this light wavelength, the perovskite absorption coefficient is 1.2×10^5 cm^{-1}.*

Figure 3.7 (a) shows the absorption and photoluminescence spectra in trihalide perovskite films, which is the absorbance spectrum of a $MAPbI_3$ film near the optical gap at 300 K. The PL spectrum consists of a single line slightly shifted to the red with respect to the excitonic absorption peak. We can explain the energy shift is mostly caused by self-absorption due to the finite thickness of the film. The shape of the emission corrected for self-absorption and the emission in thinner films is almost coincident with the excitonic resonance, while the shape is slightly asymmetric towards the higher energy side. These results point to the intrinsic nature of the

emitting species [35].

Figure 3.7 (b) reports the PL decays of perovskite films excited by sub-picosecond laser pulses and detected by a streak camera. With the ultrafast optical spectroscopy, particularly the time-resolved PL, we can investigate the effect of excitonic correlations on the excited- state relaxation dynamics. The PL decay traces measured with the streak camera for the $MAPbI_3$ perovskite films. Following excitation, carriers quickly thermalize to the extremes of the conduction and valence bands. The optically injected electron–hole pair density n_0 at the film surface was estimated by multiplying the laser pulse photon fluence times the film absorption coefficient and ranged from ~10^{16} to ~10^{19} cm^{-3}. In this carrier density range, the transient emission spectrum is always peaked at the exciton resonance, $\hbar\omega=E_X$. However, the exciton binding energy is small, and the high-energy side of the PL spectrum overlaps with the expected energies of band-to-band transitions. Under all excitation conditions and for all samples, the PL signal rises instantaneously; if an exciton population is formed, this process takes place within the temporal resolution of our experimental set-up, ~60 ps.

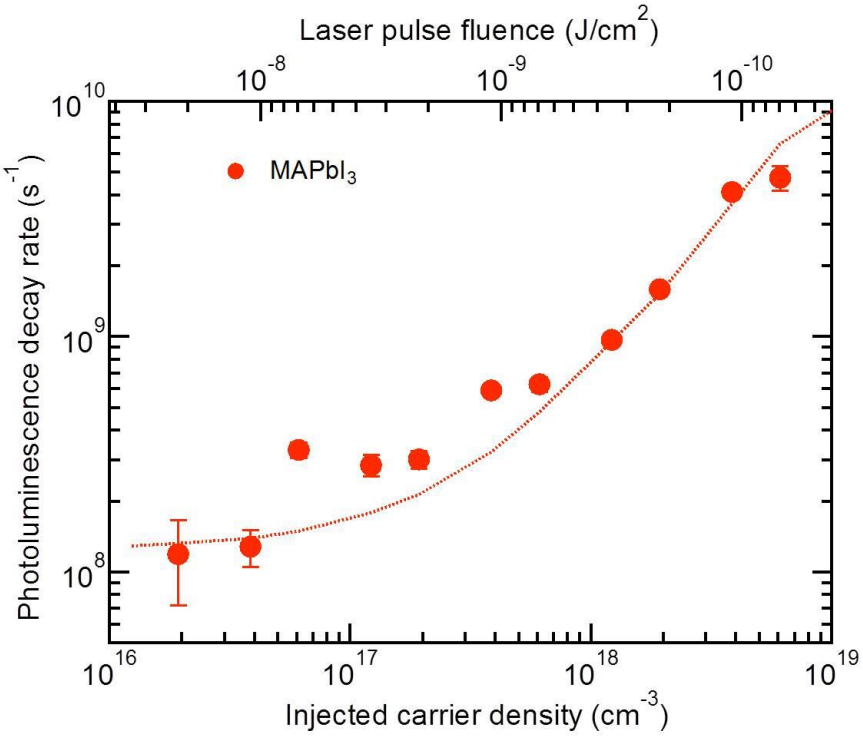

Figure 3.8| Photoluminescence decay rates. *The decay rates for the transient photoluminescence signal decays are plotted as a function of the injected carrier density (or laser pulse fluence on top axis). The rates, defined as* $K_{PL} = \left[\frac{1}{PL}\frac{dPL}{dt}\right]_{t=0}$ *are extracted from the data in Figure 3.7 b. Such rates represent therefore the very initial decay and should not be mistaken for the average photoluminescence decay rate obtained by fitting the entire decay with an exponential function. The error bars represent the s.d. from a least square fit to an exponential decay and are reported only when they exceed the size of the marker. Remarkably, the rates are very similar for the two perovskites (although the average exponential decay rates are significantly different) and grow together for growing injected carrier densities. We infer that such rates measure the intrinsic density-dependent bimolecular and Auger recombination processes. The dotted lines represent the outcome of the rate equation model: also in this case the agreement with the experiment is satisfactory. Experimental and theoretical decay rates represent an exponential fit to the initial photoluminescence transients, carried out in the same time-window for experiments and simulations. The exponential spatial profile of the electron–hole density created by laser pulses is accounted for in the model simulations*.

PL decay rates are also investigated. Figure 3.8 shows the initial decay rates $K_{PL} = \left[\frac{1}{PL}\frac{dPL}{dt}\right]_{t=0}$ of the PL signal, extracted from the decays in Figure 3.7 b. The PL signal becomes faster for increasing n_0, indicating the activation of density-dependent recombination mechanisms. k_{PL} shows a remarkable increase for injected population densities $>10^{17}$ cm^{-3}. For n_0 $\sim10^{19}$ cm^{-3}, k_{PL} $\sim10^{10}$ s^{-1}. It should be noted that $\frac{1}{k_{PL}}$ differs from the average PL lifetime τ obtained by fitting the PL decay with a single exponential. We found that τ= 80 ns for $MAPbI_3$ perovskite. These findings indicate that the initial density-dependent decay of the PL signal is caused by intrinsic nonlinear processes, while the longer-time decay is dictated by extrinsic effects, such as traps and defects. Although lifetime is obtained by laser stimulation, as long as the film is processed in such a way that the mean PL lifetime exceeds several

nanoseconds at sun illumination, carrier mobility is sufficiently high to guarantee efficient charge collection in the photovoltaic device [53].

3.4 Conclusion

In summary, structural characterization was carried out by analysing the X-ray diffraction patterns. The result shows that it is not difficult to get a $CH_3NH_3PbI_3$ perovskite from different method. The reaction time of the vapour assisted two-step method is important for forming a perovskite, and part of the PbI_2 would be left in the perovskite if the heating time is short.

The morphology investigation was performed by an AFM. The images show us significant difference morphology from the samples prepared with different method. The single step method will supply a needle-shaped crystal, partial surface coverage on the substrate, which is not proper for planar solar cell. The two-step spin-casting method show us a smooth film except an unexpectedly mountain in the flat plain. The final best films are fabricated by vapour assisted two-step method, the RMS roughness of the sample could be around 35 nm (on the TiO_2) while the RMS roughness could be smaller if we improve the processing details.

The transient photoluminescence spectroscopy analysis show that the lifetime of the excitons could be as high as τ = 80 ns under a laser stimulation. Nevertheless, as long as the film is processed in such a way that the mean PL lifetime exceeds several nanoseconds at sun illumination, carrier mobility is sufficiently high to guarantee efficient charge collection in the photovoltaic device.

Reference

[1]. F. Deschler, M. Price, S. Pathak, L. Klintberg, D.-D. Jarausch, R. Higler, S. Hüttner, T. Leijtens, S. Stranks, H. Snaith, M. Atatüre, R. Phillips, R. Friend, "High Photoluminescence Efficiency and Optically Pumped Lasing in Solution-Processed Mixed Halide Perovskite Semiconductors", ***J. Phys. Chem. Lett.*** 2014, 5, 1421.

[2]. Q. Zhang, S. Ha, X. Liu, T. Sum, Q. Xiong, "Room-Temperature Near-Infrared High-Q Perovskite Whispering-Gallery Planar Nanolasers", ***Nano Lett.*** 2014, 14, 5995.

[3]. T. Kondo, T. Azuma, T.Yuasa, R.Ito, "Biexciton Lasing in the Layered Perovskite-Type Material $(C_6H_{13}NH_3)_2PbI_4$", ***Solid State Communications***. 1998, 105, 253.

[4]. B. R. Sutherland, S, Hoogland, M. M. Adachi, C. Wong, and E. H. Sargent, "Conformal Organohalide Perovskites Enable Lasing on Spherical Resonators", ***ACS nano***, 2014, 8, 10947.

[5]. G. Xing, N. Mathews, S. Lim, N. Yantara, X. Liu, D. Sabba, M. Grätzel, S. Mhaisalkar, T. Sum, "Low-Temperature Solution-Processed Wavelength-Tunable Perovskites for Lasing", ***Nature Mater.*** 2014, 13, 476.

[6]. Z. Tan, R. S. Moghaddam, M L. Lai, P. Docampo, R. Higler, F. Deschler, M. Price, A. Sadhanala, L. M. Pazos, D. Credgington, F. Hanusch, T. Bein, H. J. Snaith, and R. H. Friend, "Bright light-emitting diodes based on organometal halide perovskite", ***Nat. Nanotech.*** 2014, 9, 687.

[7]. K. Chondroudis and D. B. Mitzi, "Electroluminescence from an Organic−Inorganic Perovskite Incorporating a Quaterthiophene Dye within Lead Halide Perovskite Layers", ***Chem. Mater.*** 1999, 11, 3028.

[8]. D. B. Mitzi, C. D. Dimitrakopoulos, L. L. Kosbar, "Structurally Tailored Organic- Inorganic Perovskites: Optical Properties and Solution-Processed Channel Materials for Thin-Film Transistors", ***Chem . Mater.*** 2001, 13, 3728.

[9]. Z. Xu, D.B. Mitzi, C.D. Dimitrakopoulos and K. R. Maxcy, "Semiconducting

Perovskites (2-$XC_6H_4C_2H_4NH_3)_2SnI_4$ (X= F, Cl, Br): Steric Interaction between the Organic and Inorganic Layers", ***Inorg. Chem.*** 2003, 42, 2031.

[10]. C. R. Kagan, D. B. Mitzi, C.D. Dimitrakopoulos, "Organic-Inorganic Hybrid Materials as Semiconducting Channels in Thin-Film Field-Effect Transistors", ***Science.*** 1999, 286, 945.

[11]. E. Edri, S. Kirmayer, D. Cahen, G. Hodes, "High Open-Circuit Voltage Solar Cells Based on Organic–Inorganic Lead Bromide Perovskite", ***J. Phys. Chem. Lett.*** 2013, 4, 897.

[12]. G. Eperon, V. Burlakov, A. Goriely, H. Snaith, "Neutral Color Semitransparent Microstructured Perovskite Solar Cells", ***ACS Nano.*** 2014, 8, 591.

[13]. N. J. Jeon, H. G. Lee, Y. C. Kim, J. Seo, J. H. Noh, J. Lee, and S. I. Seok, "O-Methoxy Substituents in Spiro-OMeTAD for Efficient Inorganic–organic Hybrid Perovskite Solar Cells", ***J. Am. Chem. Soc.*** 2014, 136, 7837.

[14]. F. Hao, C. Stoumpos, D. Cao, R. Chang, M. Kanatzidis, "Lead-Free Solid-State Organic-Inorganic Halide Perovskite Solar Cells", ***Nature Photon.*** 2014, 8, 489.

[15]. J. M. Frost, K. T. Butler, F. Brivio, C. H. Hendon, "Atomistic Origins of High-Performance in Hybrid Halide Perovskite Solar Cells", ***Nano Lett.*** 2014, 14, 2584

[16]. J.-H. Im, I.-H. Jang, N. Pellet, M. Grätzel, N.-G. Park, "Growth of $CH_3NH_3PbI_3$ Cuboids with Controlled Size for High-Efficiency Perovskite Solar Cells", ***Nat. Nanotech.*** 2014, 9, 927.

[17]. C. S. Ponseca Jr, T. J. Savenije, M. Abdellah, K. Zheng, A. Yartsev, T. Pascher, T. Harlang, P. Chabera, T. Pullerits, A. Stepanov, J.-P. Wolf, and V.Sundström "Organometal Halide Perovskite Solar Cell Materials Rationalized: Ultrafast Charge Generation, High and Microsecond-Long Balanced Mobilities, and Slow Recombination", ***J. Am. Chem. Soc.*** 2014, 136, 5189.

[18]. J. Lee, D. Seol, A. Cho, N. Park, "High‐Efficiency Perovskite Solar Cells Based on the Black Polymorph of $HC(NH_2)_2PbI_3$", ***Adv. Mater.*** 2014, 26, 4991.

[19]. W. Nguyen, C. Bailie, E. Unger, M. McGehee, "Enhancing the Hole-Conductivity of Spiro-OMeTAD without Oxygen or Lithium Salts by

Using Spiro(TFSI)$_2$ in Perovskite and Dye-Sensitized Solar Cells", ***J. Am. Chem. Soc.*** 2014, 136, 10996

[20]. K. Wojciechowski, M. Saliba, T. Leijtens, A. Abate, H. Snaith, "Sub-150 ℃ Processed Meso-Superstructured Perovskite Solar Cells with Enhanced Efficiency", ***Energy Environ. Sci.***, 2014, 7, 1142.

[21]. Q. Chen, H. Zhou, Z. Hong, S. Luo, H.-S. Duan, H.-H. Wang, Y. Liu, G. Li, Y. Yang, "Planar Heterojunction Perovskite Solar Cells via Vapor-Assisted Solution Process", ***J. Am. Chem. Soc.*** 2014, 136, 622.

[22]. H. Zhou, Q. Chen, G. Li, S. Luo, T. Song, H.-S. Duan, Z. Hong, J. You, Y. Liu, Y. Yang, "Interface Engineering of Highly Efficient Perovskite Solar Cells", ***Science.*** 2014, 345, 542.

[23]. N. Jeon, J. Noh, Y. Kim, W. Yang, S. Ryu, S. Seok, "Solvent Engineering for High-Performance Inorganic–organic Hybrid Perovskite Solar Cells", ***Nat. Mater.*** 2014, 13, 897.

[24]. M. Lee, J. Teuscher, T. Miyasaka, T. Murakami, H. Snaith, "Efficient Hybrid Solar Cells Based on Meso-Superstructured Organometal Halide Perovskites", ***Science***, 2012, 338, 643.

[25]. M. Liu, M. Johnston, H. Snaith, "Efficient Planar Heterojunction Perovskite Solar Cells by Vapour Deposition", ***Nature.*** 2013, 501, 395.

[26]. P. Docampo, J. Ball, M. Darwich, G. Eperon, H. Snaith, "Efficient Organometal Trihalide Perovskite Planar-Heterojunction Solar Cells on Flexible Polymer Substrates", ***Nat. Comm.*** 2013, 4, 2761.

[27]. H. Yu, F. Wang, F. Xie, W. Li, J. Chen, N. Zhao, "The Role of Chlorine in the Formation Process of '$CH_3NH_3PbI_{3-x}Cl_x$' Perovskite", ***Adv. Funct. Mater.*** 2014, 24, 7102.

[28]. Y. Zhao, K. Zhu,"CH3NH3Cl-Assisted One-Step Solution Growth of $CH_3NH_3PbI_3$: Structure, Charge-Carrier Dynamics, and Photovoltaic Properties of Perovskite Solar Cells", ***J. Phys. Chem. C,*** 2014, 118, 9412.

[29]. S. Stranks, G. Eperon, G. Grancini, C. Menelaou, M. Alcocer, T. Leijtens, L. Herz, A. Petrozza, H. Snaith, "Electron-Hole Diffusion Lengths Exceeding 1

Micrometer in an Organometal Trihalide Perovskite Absorber", ***Science***. 2013, 342, 341.

[30]. G. Xing, N. Mathews, S. Sun, S. Lim, Y. Lam, M. Grätzel, S. Mhaisalkar, T. Sum, "Long-Range Balanced Electron- and Hole-Transport Lengths in Organic-Inorganic $CH_3NH_3PbI_3$", ***Science.*** 2013, 342, 344.

[31]. D. Shi, V. Adinolfi, R. Comin, M. Yuan, E. Alarousu, A. Buin, Y. Chen, S. Hoogland, A. Rothenberger, K. Katsiev, Y. Losovyj, X. Zhang, P.A. Dowben, O.F. Mohammed, E.H. Sargent, and O.M. Bakr, "Solar Cells. Low Trap-State Density and Long Carrier Diffusion in Organolead Trihalide Perovskite Single Crystals", ***Science***. 2015, 347, 519.

[32]. Q. Dong, Y. Fang, Y. Shao, P. Mulligan, J. Qiu, L. Cao, J. Huang, "Electron-Hole Diffusion Lengths >175 μm in Solution Grown $CH_3NH_3PbI_3$ Single Crystals", ***Science.*** 2015, DOI: 10.1126/science.aaa5760.

[33]. G. Eperon, V. Burlakov, P. Docampo, A. Goriely, H. Snaith, "Morphological Control for High Performance, Solution-Processed Planar Heterojunction Perovskite Solar Cells", ***Adv. Funct. Mater.***,2014, 24, 151.

[34]. S. Colella, E. Mosconi, P. Fedeli, A. Listorti, F. Gazza, F. Orlandi, P. Ferro, T. Besagni, A. Rizzo, G. Calestani, G. Gigli, F. Angelis, R. Mosca, "$MAPbI_{3-x}Cl_x$ Mixed Halide Perovskite for Hybrid Solar Cells: The Role of Chloride as Dopant on the Transport and Structural Properties", ***Chem. Mater.*** 2013, 25, 4613.

[35]. M. Saba, M. Cadelano, D. Marongiu, F. Chen, V. Sarritzu, N. Sestu, C. Figus, M. Aresti, R. Piras, A. Lehmann, C. Cannas, A. Musinu, F. Quochi, A. Mura, G. Bongiovanni, "Correlated Electron–hole Plasma in Organometal Perovskites", ***Nat. Comm.***, 2014, 5,5049.

[36]. Bernard Valeur, <Molecular Fluorescence: Principles and Applications>, Wiley-VCH Verlag GmbH, 2001.

[37]. M. Saba, M. Aresti, F. Quochi, M. Marceddu, M.A. Loi, J. Huang, D.V. Talapin, A. Mura, G. Bongiovanni, "Light-Induced Charged and Trap States in Colloidal Nanocrystals Detected by Variable Pulse Rate Photoluminescence

Spectroscopy", ***ACS Nano.*** 2013, 7, 229.

[38]. T. Baikie, Y. Fang, J. Kadro, M. Schreyer, F. Wei, S. Mhaisalkar, M. Graetzel, T. White, "Synthesis and Crystal Chemistry of the Hybrid Perovskite $(CH_3NH_3)PbI_3$ for Solid-State Sensitized Solar Cell Applications", ***J. Mater. Chem. A.*** 2013, 1, 5628.

[39]. D.S. Bhavsar, "Structural Studies of Vacuum Evaporated Lead Iodide Thin Films", ***Adv. Appl. Sci. Res.*** 2011, 2, 407.

[40]. Y. Dang, Y. Liu, Y. Sun, D. Yuan, X. Liu, W. Lu, G. Liu, H. Xia, X. Tao, "Bulk Crystal Growth of Hybrid Perovskite Material $CH_3NH_3PbI_3$", ***Cryst. Eng. Comm.*** 2015, 17, 665.

[41]. M. Shkir, H. Abbas, Siddhartha, Z. R. Khan, "Effect of Thickness on the Structural, Optical and Electrical Properties of Thermally Evaporated PbI_2 Thin Films", ***Journal of Physics and Chemistry of Solids***, 2012, 73, 1309.

[42]. Y. Zhao, K. Zhu, "Optical Bleaching of Perovskite ($CH_3NH_3PbI_3$) through Room-Temperature Phase Transformation Induced by Ammonia", ***Chem. Commun.*** 2014, 50, 1605.

[43]. J.-H. Im, H.-S. Kim, N.-G. Park, "Morphology-Photovoltaic Property Correlation in Perovskite Solar Cells: One-Step versus Two-Step Deposition of $CH_3NH_3PbI_3$", ***APL Mater.*** 2014, 2, 081510.

[44]. M. Ramesh, K.M. Boopathi, T.-Y.Y. Huang, Y.-C.C. Huang, C.-S.S. Tsao, C.-W.W. Chu, "Using an Airbrush Pen for Layer-by-Layer Growth of Continuous Perovskite Thin Films for Hybrid Solar Cells", ***ACS Appl Mater Interfaces.*** 2015, 7, 2359.

[45]. Y. Xu, L. Zhu, J. Shi, S. Lv, X. Xu, J. Xiao, J. Dong, H. Wu, Y. Luo, D. Li, Q. Meng, "Efficient Hybrid Mesoscopic Solar Cells with Morphology-Controlled $CH_3NH_3PbI_{3-x}Cl_x$ Derived from Two-Step Spin Coating Method", ***ACS Appl Mater Interfaces.*** 2015, 7, 2242.

[46]. W. Zhang, M. Saliba, D. Moore, S. Pathak, M. Hörantner, T. Stergiopoulos, S. Stranks, G. Eperon, J. Alexander-Webber, A. Abate, A. Sadhanala, S. Yao, Y. Chen, R. Friend, L. Estroff, et al., "Ultra smooth Organic–inorganic Perovskite

Thin-Film Formation and Crystallization for Efficient Planar Heterojunction Solar Cells", ***Nat. Commun.*** 2015, 6, 6142.

[47]. L. Zuo, Z. Gu, T. Ye, W. Fu, G. Wu, H. Li, H. Chen, "Enhanced Photovoltaic Performance of $CH_3NH_3PbI_3$ Perovskite Solar Cells through Interfacial Engineering Using Self-Assembling Monolayer", ***J. Am. Chem. Soc.*** 2015, DOI: 10.1021/ja 512518r.

[48]. D. Ahlawat, "Study Of Band Gap Energy And Thermal Properties Of PbI_2 By Photoacoustic Spectroscopy", ***Mod. Phys. Lett. B.*** 2012, 26, 1250098.

[49]. R. Ahuja, H. Arwin, A. Silva, C. Persson, J. Osorio-Guillén, J. Almeida, C. Araujo, E. Veje, N. Veissid, C. An, I. Pepe, B. Johansson, "Electronic and Optical Properties of Lead Iodide", ***J. Appl. Phys.*** 2002, 92, 7219.

[50]. J. Robertson, "Electronic Structure of SnS_2, $SnSe_2$, CdI_2 and PbI_2", ***J. Phys. C: Solid State Phys.***, 1979, 12, 4735.

[51]. D. A. Silva, N. Veissid, C.Y. An, I. Pepe, "Optical Determination of the Direct Bandgap Energy of Lead Iodide Crystals", ***Appl. Phys. Lett.***1996, 69, 1930.

[52]. F. Quochi, G. Schwabegger, C. Simbrunner, F. Floris, M. Saba, A. Mura, H. Sitter, G. Bongiovanni, "Extending the Lasing Wavelength Coverage of Organic Semiconductor Nanofibers by Periodic Organic–Organic Heteroepitaxy", ***Adv. Optical Mater.*** 2013, 1, 117.

[53]. C. Wehrenfennig, G. Eperon, M. Johnston, H. Snaith, L. Herz, "High Charge Carrier Mobilities and Lifetimes in Organolead Trihalide Perovskites", ***Adv. Mater.*** 2014, 26, 1584.

[54]. D. S. Wolf, J. Holovsky, S. J. Moon, P. Löper, "Organometallic Halide Perovskites: Sharp Optical Absorption Edge and Its Relation to Photovoltaic Performance", ***J. Phys. Chem. Lett***. 2014, 5, 1035.

CHAPTER 4
Planar $CH_3NH_3PbI_3$ perovskite solar cells

Recent advances in solar photovoltaics based on organometal trihalide perovskites have triggered intensive research into the morphology and interfaces of perovskite films that affect their charge transport characteristics. In this chapter, we will discuss the function of compact TiO_2 morphology in a planar solar cell; and the effect of modifying the interface between metal contact and hole transport layer. X-ray diffraction (XRD) was used to assure that crystallinity was preserved for the perovskite in the solar cell; atomic force microscope (AFM) was used to investigate the solar cell structure and the morphology. The modification of MoO_3 and LiF show a positive function to the solar cell performance.

4.1 Introduction

Organometal trihalide perovskite materials are currently among the most competitive candidates as absorber materials to be used for thin-film photovoltaic (PV) applications [1-5]. Within the past 6 years, remarkable improvements in perovskite solar cells efficiencies have been reported, from initial marks around 3.8% [7] to as much as ~19.3% [6]. This rapid increase in power conversion efficiency (PCE) may be related to the perovskite materials possessing most of the properties required for solar cells: appropriate band gap, high absorption coefficient, excellent carrier transport, and tolerance to defects [8]. As we all know, the cost of the perovskite materials is very low and they are easy to synthesize. So perovskite materials are easy to tune on composition and structure by adjusting the metal halide framework and the organic species [9].

The first attempt on solar cell was in dye-sensitized solar cells based on mesoporous structures (shown as Figure 4.1), and the efficiency was not satisfactory [7]; in the later works, the perovskites have been gradually found to assume all of the principal roles of PV operation [11], and PV devices with planar structure have been demonstrated.[12,13]

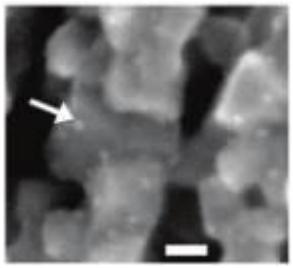

Figure 4.1| *SEM image of $CH_3NH_3PbBr_3$ deposited on TiO_2 surface. The scale bar shows 10nm. [7]*

In most initial reports on perovskite solar cells, the device structure could be described as in Figure 4.2, based on mesoporous architectures (Figure 4.2 A). On the transparent substrate, usually glass, is a layer of transparent conductive oxide (TCO) which could be Indium tin oxide (ITO) or fluorine doped tin oxide (FTO). To

transport the electron from the active layer to the electrodes and to act as a hole blocking layer, a thin layer of compact TiO_2 was deposited on top of the TCO layer. The compact TiO_2 layer could be prepared by spin-casting or spraying pyrolysis of compact TiO_2 precursor. The mesoporous scaffold layer is typically made of ZnO, TiO_2, Al_2O_3, because they are transparent and conductive when they were thin enough (around 500 nm ~ 600 nm). The mesoporous layer is fabricated by spin-casting the diluted porous paste and then sintering at 550 Celsius in air for around 30 minutes. The perovskite layer could be deposited on the mesoporous layer when the scaffold layer was cooled down to room temperature. The hole transporting material (HTM) should be spin-casted on top of the perovskite layer before evaporating the metal contact.

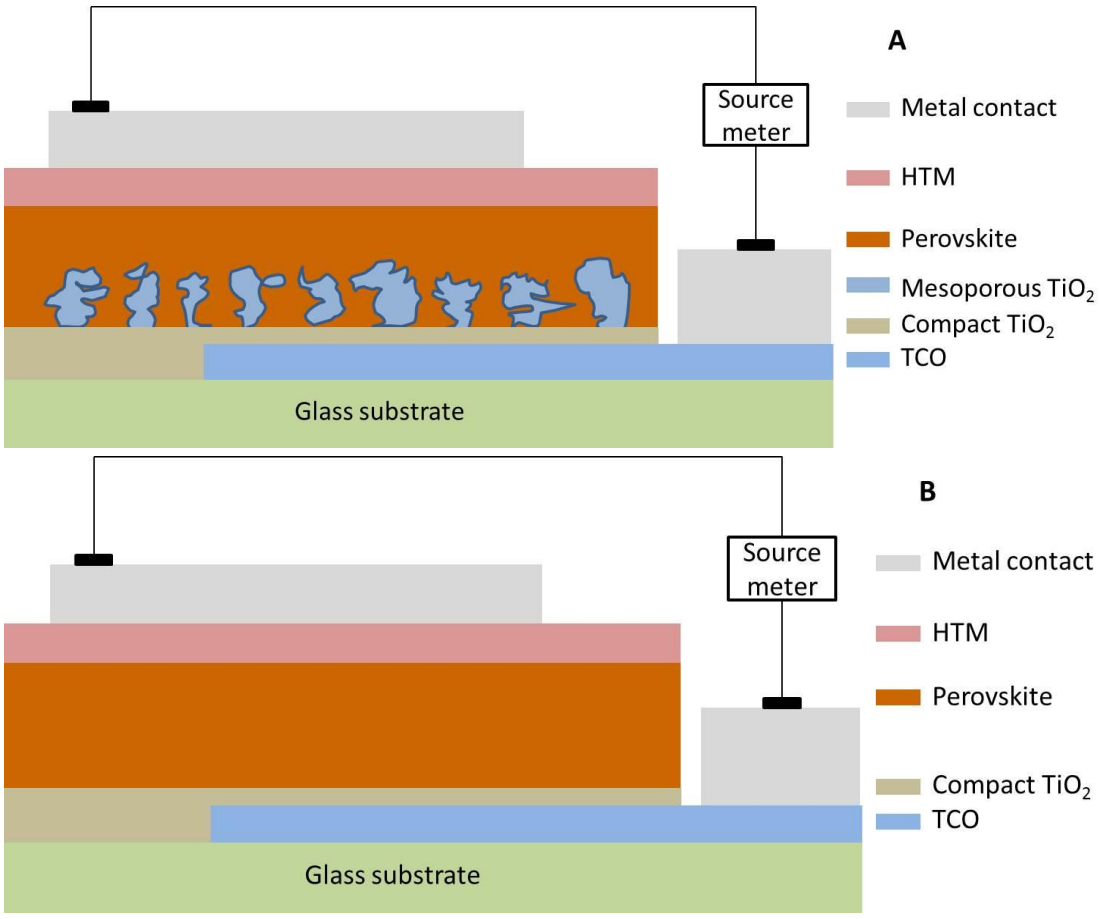

Figure 4.2| *The basic structures of the perovskite solar cell. Part A is a solar cell based on mesoporous structure (top). Part B is a planar solar cell (bottom).*

Planar structure solar cell provides more flexibility for device optimization, multijunction construction, and investigation of the underlying device physics. Hence, the planar structure turns out to be very attractive for basic research purposes. As the figure 4.2 part B shows, the difference from the mesoporous structure is that no scaffold layer in the solar cell. Inside the device based on this structure, for example, in an organic solar cell, only the charge separation occurs at the boundary between two materials where photo-generated electron–hole pairs are separated into charge carriers. Because of the low mobility in organic material, the photo-generated electron-hole pairs far away from the interface cannot diffuse to the boundary, leading to an invalid separation or recombination. Efficient solar cell relies on the separation and collection of charge carriers before they lose their photo-generating energy through recombination. Hence, the diffusion length of the charge carriers is an important property affecting the performance of a solar cell [11]. Recent research result shows that an electron-hole diffusion length is longer than 100 nm in $CH_3NH_3PbI_3$ layers [31], which is comparable or larger than the light propagation depth, indicating that the absorber thickness requirement to achieve complete absorption of solar irradiation is satisfied.

The perovskite film is deposited on the compact TiO_2 layer directly. Additional efforts are required to fabricate high-quality perovskite films. Spin-casting and vacuum evaporation are very useful techniques currently employed to prepare good quality planar films. Especially, vacuum evaporation is one of the most promising techniques to construct high quality thin films for planar structure. In Snaith's group, perovskite films were prepared with co-evaporation of two precursors ($PbCl_2$ and CH_3NH_3I), and the films exhibit satisfactory coverage and uniformity within expectations [12]. However, this technique demands high vacuum, which is energy consuming and relatively more difficult than other techniques. Solution-based techniques have also been employed to fabricate thin films, in which a mixture of two precursors is used to form the perovskite film. Due to the lack of proper solvents that could dissolve both components, and the high reaction rate of the perovskite component, this process often results in thin films with pinhole formation and

incomplete surface coverage, which deteriorates the film quality and hampers the device performance [1]. As a variation to this method, a two-step approach was demonstrated to fabricate efficient PV devices by dipping previously deposited inorganic precursor films into solutions containing organic ammonium salt [13]. The method, however, has been successful used to prepare perovskite films with scaffold structure, but it is not optimal for planar devices: when we put the pre-prepared inorganic precursor films into another solution, even with a dip coater, the reaction occurs at different times on different parts of the surface, which results a film with a wave like fluctuation and enhanced surface roughness [14]. Concluding all the cases, Yang's group used a vapour assisted solution process (VASP) to fabricate perovskite thin films and subsequently PV devices with planar geometry [15]. In their works, they could prepare a high quality perovskite film. The key step was film growth via in situ reaction of the as-deposited film of PbI_2 with CH_3NH_3I vapour. The pre-prepared inorganic film was put in a petri dish with CH_3NH_3I surrounded and the petri dish was put on the hotplate to heat at 150 Celsius. All the operation could be performed under N_2, the vacuum condition was not necessary. In our work, we adopt and slightly modify the two steps method from Yang's group (figure 2.2). We put the pre-prepared PbI_2 film on the lid of the petri dish, making the inorganic film facing to the ammonium salt when the petri dish was heated. This method provides films with well-defined grain structure, full surface coverage, and small surface roughness, suitable for PV applications. Devices based on films prepared by this two steps method achieved a best PCE of 6%.

4.2 Experimental

4.2.1 TiO_2 and perovskite solar cell preparation

Here, I would describe the detailed procedure to prepare the whole device, which is from the bottom compact TiO2 to the end metal contact. All the materials were bought from Sigma-Aldrich Company except ammonium salt.

4.2.1.1 Compact TiO_2 preparation

All the precursors to prepare TiO_2 are diluted from a titanium diisopropoxide bis(acetylacetonate) (bought from Sigma-Aldrich) in isopropanol solution.

At first, a fluorine-doped tin oxide (FTO) coated glass (bought from Dyesol Company) with 15 Ω/□ resistivity was patterned by etching with Zn powder and 2M HCl diluted in water. The FTO glass was cut into 15×15 mm square pieces. Plastic tape was used to protect the area not to be etched. The FTO glasses in HCl solution about 30 seconds were enough for etching. The etched substrate was then cleaned with 2% soap water with 5 minutes sonicating bath, and then sonicated with deionized water about 5 minutes again to remove the soap. At last, they should be rinsed with acetone and ethanol and dried with clean dry air. The substrate underwent a H_2O_2 boiling treatment for 10 minutes prior to prepare TiO_2.

The titanium diisopropoxide bis(acetylacetonate) was diluted into 0.3M and 0.15M with anhydrous isopropanol as TiO_2 precursor, then the two solutions were transferred into two syringes. A 450 nm diameter filter was used to remove the impurities. TiO_2 deposition occurred with the FTO glass substrates and the syringes with filter inside a dry box, purged with dry air to adjust the humidity to a controlled value. At first, the 0.15M TiO_2 precursor was dropped onto the substrate and spin-cast at 3000rpm about 30 seconds. Then the 0.3M TiO_2 precursor was dropped onto the same substrate again and spin-cast at 3000rpm about 30 seconds; this procedure was repeated two times (shown as figure 4.3). After the spin-casting procedure, the substrate with TiO_2 precursor film was put in an oven to be sintered.

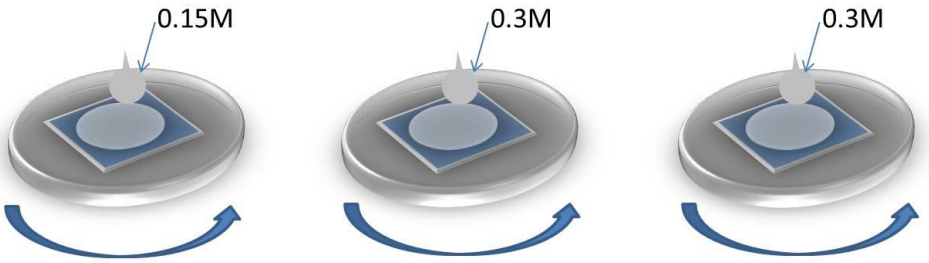

Figure 4.3| Compact TiO_2 preparations. *From left to right, TiO_2 precursor was spin casted on the FTO substrate 3 times according to the different concentration. The spin-casting procedure was operated in a dry box in order to keep it in a steady humidity condition.*

The temperature was ramped from 0 Celsius to 125 Celsius in 10 minutes and kept at 125 Celsius about 10 minutes; then the temperature increased to 580 Celsius in 30 minutes and kept at 580 Celsius about 30 minutes.

The substrate was put in a petri dish when the oven was cool down. A 50mM concentration $TiCl_4$ in deionized water was added into the petri dish, which was then placed onto a hotplate to heat at 70 Celsius for about 30 minutes. The ramping time of the heating program was 10 minutes. After the $TiCl_4$ and warming treatment, the substrate was rinsed with deionized water and ethanol. The back side of the substrate was cleaned with ethanol.

The clean substrate was again put into the oven, where the $TiCl_4$ treated TiO_2 film would be sintered at 550 Celsius about 30 minutes. The ramping time was 30 minutes, again.

4.2.1.2 Perovskite solar cell preparation

The solar cell with a planar structure was prepared in N_2 filled glove box after the compact TiO_2 was ready. At first, 460mg lead (II) iodide (PbI_2) (99.999% Sigma-Aldrich 554359-5g) was dissolved in 1ml anhydrous N,N-Dimethylformamide (DMF) to form a 1 M concentration solution and left stirring at 80 Celsius overnight. The PbI_2 solution and the TiO_2 substrate were warmed up to 80 Celsius for 30 minutes before spin-casting. Around 20 μL PbI_2 solution was dropped onto the substrate, then

the spin-casting program started. The spinning speed was ramped to 7000 rpm in 5 seconds, and then kept constant for 30 seconds. After the spin-casting step, the PbI_2 film was place onto a hotplate to heat at 100 Celsius for a quick dry, lasting about 10 minutes. Then the PbI_2 film was attached onto the lid of a petri dish, and around 200mg CH_3NH_3I salt was dispersed on the bottom (the CH_3NH_3I synthesis route could be found in Chapter 2.1). The whole petri dish was put on a hotplate heated at 150 Celsius inside a N_2 filled glove box overnight (around 14 hours), in order to realize the vapour assisted evaporation procedure described in the former chapter. As the reaction between PbI_2 and CH_3NH_3I proceeded to form $CH_3NH_3PbI_3$ perovskite, we could see that the colour of the PbI_2 film gradually turned from light yellow to orange and then brown. After evaporation, the $CH_3NH_3PbI_3$ perovskite film was taken off of the lid. The perovskite film was rinsed with isopropanol to remove the excess CH_3NH_3I salt on the surface (note that PbI_2 and perovskite almost cannot be dissolved in isopropanol). Finally, the perovskite film was annealed at 105 Celsius for 1 hour.

Poly (3-hexylthiophene-2,5-diyl) (P3HT) was deposited on the $CH_3NH_3PbI_3$ perovskite layer as HTM. P3HT (Sigma-Aldrich 698989-250mg) was dissolved in anhydrous chlorobenzene with concentration of 2wt%. This solution was stirred at 80 Celsius for about 1 hour to dissolve all the P3HT. About 20μl P3HT solution was dropped onto the $CH_3NH_3PbI_3$ perovskite film and then spin-cast at 6000 rpm for 30 seconds with a ramping time of 5 seconds. The film with P3HT was annealed at 105 Celsius for 1 hour.

After annealing, the perovskite film with P3HT was taken inside a vacuum evaporator to deposit the metal contacts (figure 4.4 Panel C). A mask was placed in front of the film. The evaporation was operated at the vacuum of 8×10^{-6} mBar. We could adjust the current of the heating source to control the evaporation speed in the chamber. At the same time, the thickness of the evaporating film could be read from a thickness monitor. At last, about 100nm silver were deposited on the film as the final metal contact. Between the metal contact and the P3HT layer, a thin interfacial layer could be deposited with evaporation made of a few nm of MoO_3 or LiF.

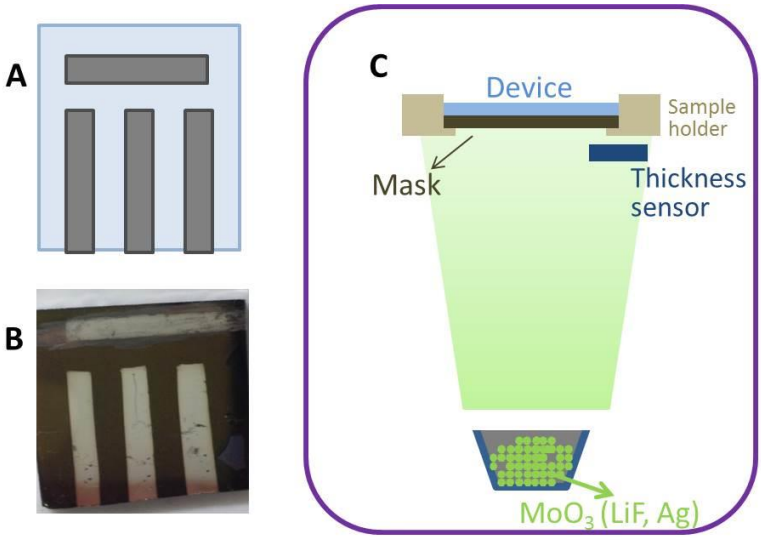

Figure 4.4| Metal and modification evaporating system sketch. *A) The schematic diagram of a solar cell. B) Photograph of a planar solar cell. C) Vacuum evaporating system, the material in the crucible could be Ag, LiF or MoO_3 according to different requirement.*

The final structure of the solar cell shown in figure 4.2 part B, with a structure of glass/FTO/compact TiO_2/$CH_3NH_3PbI_3$ film/P3HT/ (LiF:Ag). The appearance of the solar cell can be seen in the photo in figure 4.4.

4.2.2 XRD measurement

X-ray diffraction is a useful characterization method to research structure property of material. In our experiment, the XRD measurements were performed by the help of Prof. Alessandra Geddo Lehmann (University of Cagliari, Department of Physics) and Dr. Daniela Marongiu. The instrument is a D8 Discover Bruker. The samples for XRD measurement were prepared by using the same procedure as for solar cells, but without the P3HT and metal layers. For comparison, some other procedures were also employed to prepare perovskite films on a glass substrate by vapour assisted two-step method. A 0.88M PbI_2 solution in DMF was used to prepare a little thinner PbI_2 film and CH_3NH_3I powder was evaporated onto the PbI_2 film to form perovskite. The thickness of the final $CH_3NH_3PbI_3$ perovskite film was around

200nm.

Further XRD measurements on the compact TiO_2 and the perovskite film prepared on the compact TiO_2 film were performed when we fabricated solar cells. Even the perovskite in a solar cell was measured by the XRD to investigate the crystalline in different conditions. The XRD patterns cannot show us the TiO_2 peaks. But the morphologies of the TiO_2 were different in different samples (Figure 4.12).

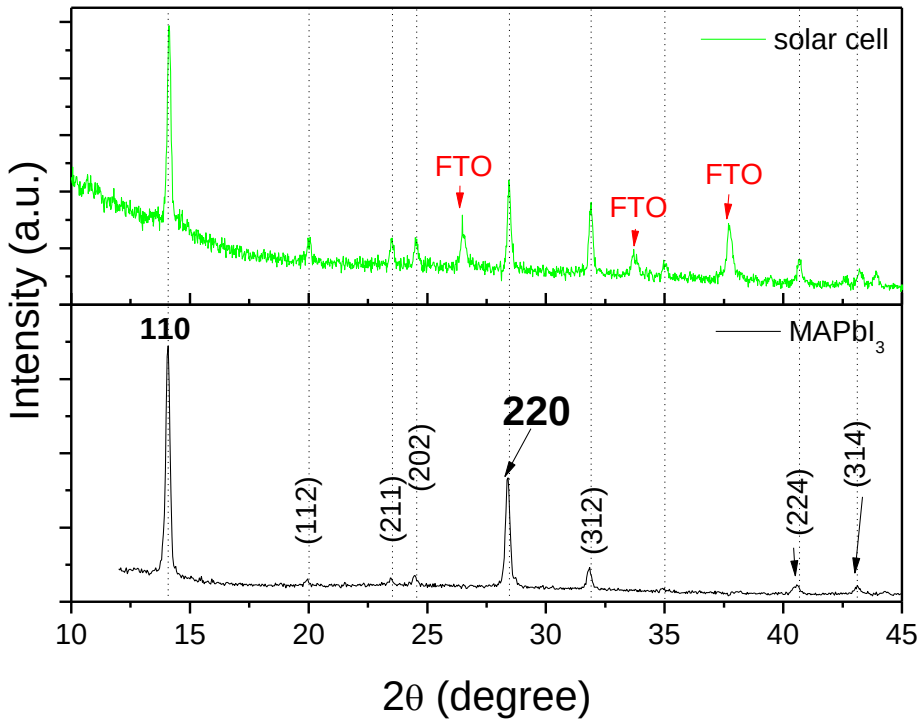

Figure 4.5| The XRD patterns of the samples. *The pattern on the top is the result of whole solar cell device. The bottom one is the result of $MAPbI_3$ film on glass.*

Figure 4.5 shows the XRD patterns of the solar cell. The measurement was performed on an integral solar cell. The solar cell structure is FTO/compact TiO_2/$MAPbI_3$/P3HT/MoO_3/Ag.

To understand the patterns of the solar cell clearer, we analyse the result with respect to the XRD on pure perovskite (figure 4.5 bottom). From the calculation and the literature [16], we can assign the peaks at the 2θ angles 14.08 °, 19.96 °, 23.44 °,

24.48 °, 28.36 °, 31.84 °, 40.56 ° and 43.12 ° to the tetragonal perovskite lattice (110), (112), (211), (202), (220), (312), (224) and (314), respectively. The pattern on the top is measured on a solar cell. In the pattern, it is not difficult to distinguish the peaks assigned to the $MAPbI_3$ tetragonal lattice. Almost all the peaks shown in a pure perovskite pattern could be found in the XRD pattern of the solar cell. Beside these peaks, there are 3 peaks at 2θ angles 26.48 °, 33.7 °, 37.74 °, which could be assigned to FTO substrate [17]. The analysis of the patterns indicates that the compact TiO_2 cannot be found with XRD, the reason maybe the TiO_2 in the solar cell is too thin to be found a clear signal in a high background noise. The peak P3HT XRD pattern should locate at 2θ angles 5 °[18], which cannot be shown in our measurement. That is to say, none of the XRD peaks in figure 4.5 is assigned to P3HT.

From the XRD patterns, we can conclude that the solar cell preparing procedures will not damage the $MAPbI_3$ perovskite structures. The perovskite synthesized by vapour assisted two-step method always shows a tetragonal lattice in the film.

4.2.3 Absorption and PL spectroscopy

4.2.3.1 Absorption of the perovskite film

Optical measurements on $CH_3NH_3PbI_3$ films were employed to optimize the fabrication procedures and make sure the resulting films have acceptable defect concentrations.

Uv-Vis absorbance measurements were performed with the help of Dr. Guido Mula, using a Perkin Elmer Lambda 950 spectrophotometer. More information about the spectrophotometer Perkin Elmer Lambda 950 could be found in chapter 2.2.3.

The samples for the absorption measurement were prepared by using the same procedure as for solar cells. The typical quantities of the solutions were 0.5M PbI_2 in DMF used to prepare a thin PbI_2 film, leading to a thin final perovskite film. The substrates were quartz and FTO glass in different measurement.

We just need to put the samples at the sample position, and put the blank substrate at the reference position (figure 4.6). To keep all the measurements as

similar as possible with the true solar cell, we measured a lot of samples on the FTO glass. And keep the reference substrate the same as the solar cell, which means we used blank FTO glass as the reference.

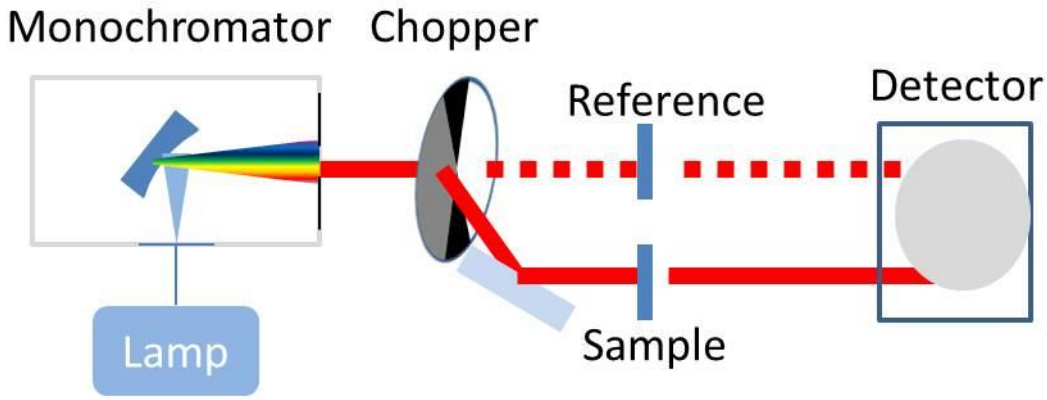

Figure 4.6| Schematic diagram of a spectrometer. *The monochromator has two types of gratings for UV/Vis and near infrared respectively. The CSSC chopper is special designed for Lambda 950 series spectrometer. The reference position and the sample position are in a same black chamber.*

4.2.3.2 Photoluminescence of the perovskite film

Photoluminescence (PL) is one of the most remarkable properties of 2D layered perovskites. Most perovskites mainly lose energy by spontaneous emission after being promoted to an excited state by absorbing photons. The energy position and intensity of photoluminescence peaks depend on the nature of the organic and inorganic components. The PL spectra allow collecting information on the electronic band structure and the study of PL peaks intensity as a function of illumination time allows evaluating the photo-stability of the perovskites.

Figure 4.7 shows the PL experiment set-up, the laser source for the photoluminescence setup was a Ti:Sapphire passively mode-locked femtosecond laser (Spectra Physics Tsunami, pumped by a diode-pumped, frequency-doubled Nd:YAG laser, Spectra Physics Millennia), emitting at 780 nm in wavelength, with a 80 MHz repetition rate and 100 fs pulse duration and the continuum white light was a Xenon

lamp. A train of laser pulses from laser source was sent by means of an optical system that allows an appropriate focusing on the sample in the study. The exciting light was absorbed by the samples, provided energy and created an excited state in the sample. When the electron-hole pair recombined between the excited state and the ground state after excited, photons would be emitted by the sample. The photoluminescence was collected by an appropriate optical configuration and acquired by the detection system. The detection system is composed of a spectrometer coupled with a streak camera. The spectrometer spectrally resolves the optical signal while the streak camera temporally resolves the optical signal. This setup is similar as the time resolved photoluminescence spectroscopy.

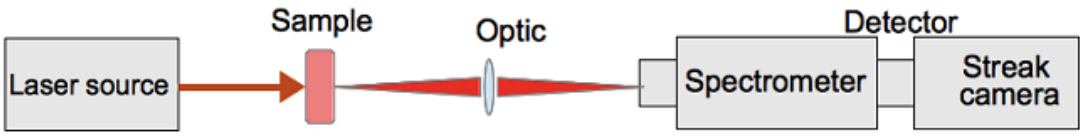

Figure 4.7| *Schematic diagram of the photoluminescence setup.*

The absorption and PL measurement results on the $CH_3NH_3PbI_3$ films at room temperature are shown in Figure 4.8. The samples were prepared on glass slide. The absorption edge of the film is about 752 nm, which means that the absorption edge is around 1.65 eV. From the image, we can see an absorption tail at the wavelength region longer than 770 nm, which could be explained in terms of a Urbach tail or just dielectric scattering by crystal grain boundaries [19]. The PL spectrum consists of a single peak at 773 nm slightly shifted to the red with respect to the excitonic absorption peak. The energy shift is mostly caused by self-absorption due to the finite thickness of the film [20].

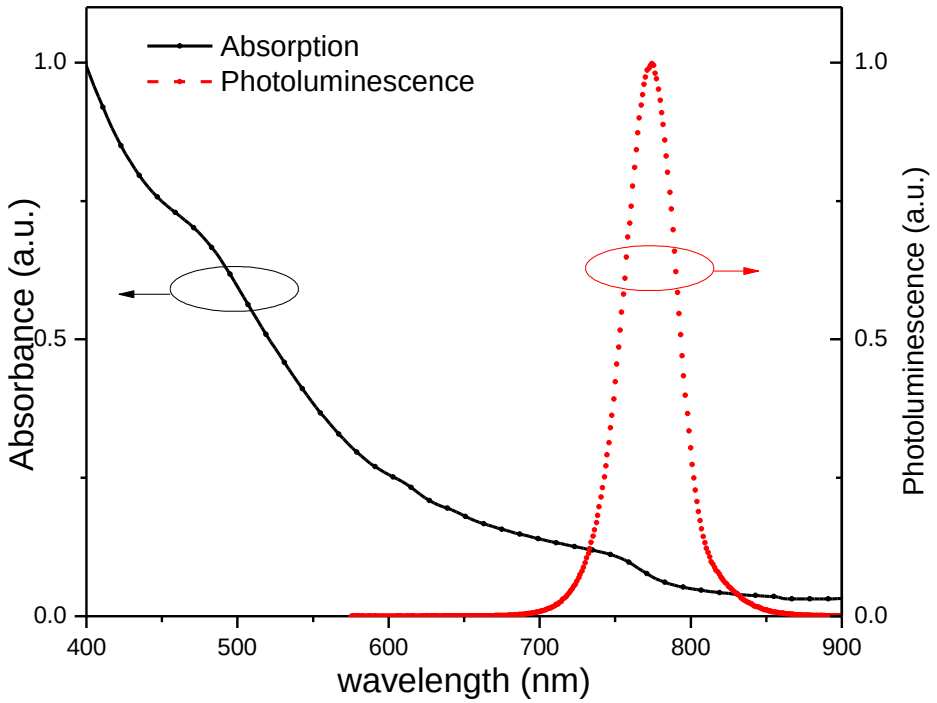

Figure 4.8| Absorption and photoluminescence spectra of $CH_3NH_3PbI_3$ films. *Visible – near infrared absorption (continuous line) spectrum of a $MAPbI_3$ film (thickness, 120nm) and luminescence (dashed line) spectrum of a $MAPbI_3$ film (thickness, 800nm) recorded at 300 K. Spontaneous emission was excited by a green laser ($\lambda = 532$ nm) operating in continuous wave (cw).*

4.2.4 Atomic force microscopy

The Atomic Force Microscopy (AFM) is a frequently-used tool that we employ to characterize the surface topography of 2D perovskites thin films. It provides us a way to evaluate surface roughness with quantified values. The average surface roughness Δ is defined as:

$$\Delta = \sqrt{\frac{1}{N}\sum_{i=1}^{N}(x_i - x_{ave})^2} \quad (4.1)$$

where N is the total number of pixels in each AFM image, x_i is the height at the ith pixel, and x_{ave} is the average height for each AFM image. AFM experiment is performed with a Solver 515 from NT-MDT Company and operated in non-contact mode. The samples were similar as perovskite in solar cell. Most $CH_3NH_3PbI_3$ films were prepared by vapour assisted two-step method. To compare the $CH_3NH_3PbI_3$ films roughness from different methods, samples prepared by a full spin-casting from solution and two-step spin-casting from solution were measured.

Figure 4.9 (left) presents a typical surface image of a perovskite film. This sample layer was prepared by vapour assisted two-step method on a compact TiO_2/FTO glass substrate, resulting in an about 300 nm thickness. Its RMS roughness is found to be 38 nm. From the image we observe irregular grain structures covering all over the surface, which is a common topography situation for most 2D organic-inorganic perovskites films from two-step preparation method. Figure 4.9 (right) shows an AFM image of a compact film prepared on FTO glass. The TiO_2 film was sintered at 550 Celsius for 45 minutes. And the relative humidity was 35% at 22 Celsius when we spin casted the TiO_2 precursor solution.

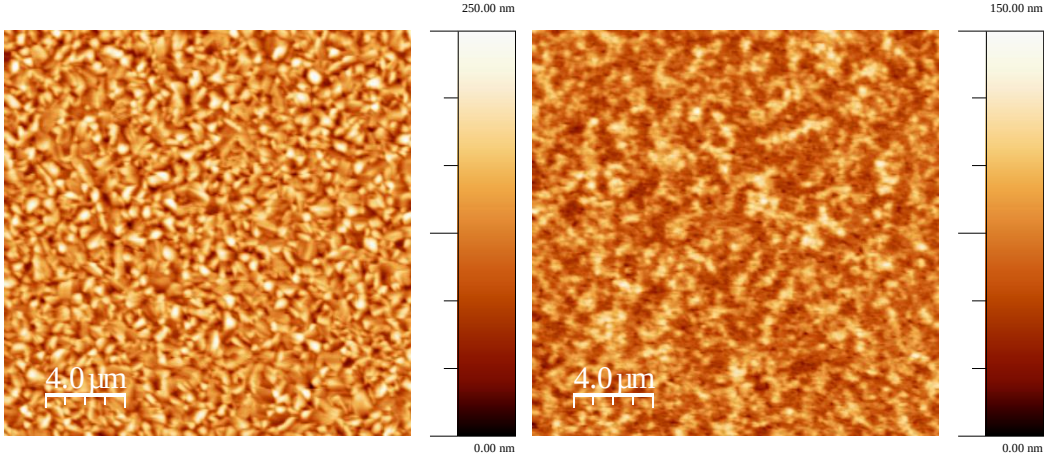

Figure 4.9| *AFM image of a vapour assisted two-step method (left). The compact TiO_2 prepared on FTO substrate (right).*

4.3 Results

4.3.1 Results of absorption and photoluminescence measurements

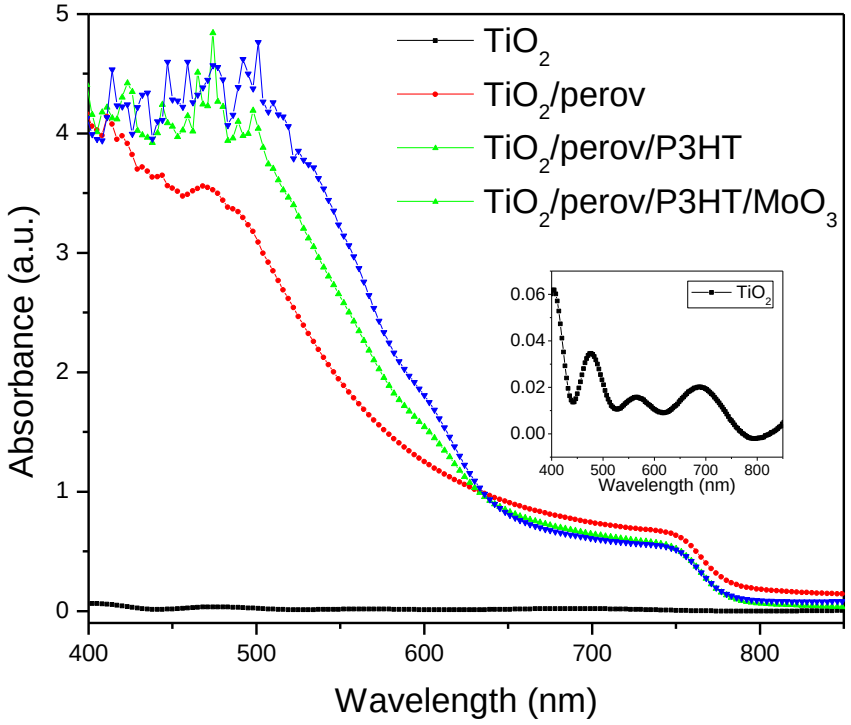

Figure 4.10| Absorption spectra of $CH_3NH_3PbI_3$ films in different structures on FTO glass substrate. *The black line is the absorbance spectrum of compact TiO_2 film on FTO glass. The red line is absorption spectrum of $MAPbI_3$ film prepared on compact TiO_2 film. The green and blue lines are spectra of perovskite films with P3HT layer and with $P3HT/MoO_3$, respectively.*

Figure 4.10 shows the absorption spectra of $CH_3NH_3PbI_3$ films on FTO glass substrates. The black line in the figure is the absorption spectrum of 100 nm compact TiO_2 film. The absorbance value is around 10^{-2} level, which means 99% of light pass through the TiO_2 film, almost no light absorbed by the compact TiO_2 layer. To room in the TiO_2 absorption spectrum, we can see the wave-like spectrum, which should be generated by the interference between the light reflected from the back side of the

TiO_2 and the incident light. It indicates that our TiO_2 film is very flat. The red line is the absorption spectrum of $CH_3NH_3PbI_3$ film on FTO glass substrate on which the compact TiO_2 film is pre-prepared. The absorption is similar as the perovskite film prepared on glass (Figure 4.8 absorption spectrum). The TiO_2 layer therefore does not affect the intrinsic structure of the perovskite. The absorption spectrum at the wavelength region shorter than 500 nm is not clear, because the thickness of the film is larger than 300 nm and the resulting absorbance hits the maximum range of the spectrophotometer. The A=1 appeared at λ=634 nm, and the A=0.6 at 752 nm. That means the perovskite film absorbance coefficient is higher than 0.3×10^5 (1/cm) when the energy is higher than 1.96eV (634nm). With our solar cells, more than 90% light could be absorbed when the wavelength shorter than 634 nm. Even at the edge of the absorption spectrum (λ=752nm), 75% of light would be absorbed. The green line is the absorption spectrum of the $CH_3NH_3PbI_3$ film covered with 100 nm P3HT layer. The spectrum indicates that there is no significant change to the light absorption of the perovskite due to P3HT. The absorption value is only a little higher than without P3HT. The spectrum of the perovskite film covered with 100 nm P3HT and 5 nm MoO_3 shows similar results. The main function of MoO_3 layer is not to affect the absorption property, but to modify the interface between the P3HT and metal contact.

4.3.2 Results of AFM

The compact TiO_2 layer is an important structure in dye sensitized solar cell to affect the charge transfer and the interface engineering [21 - 23]. We investigated the morphology of the compact TiO_2 film on FTO glass by AFM. The compact TiO_2 films were prepared under different conditions. All the samples were prepared from a titanium diisopropoxide bis(acetylacetonate) precursor in isopropanol. The preparation method was described in chapter 4.2.1.2. The substrates of all samples were FTO glass.

Table 4.1| *The RMS roughness of the compact TiO_2 film on FTO glass.*

	RH=20%	RH=35%	RH=45%
500 °C	21	18	23
550 °C	18	19	20
580 °C	20	19	21

Figure 4.11 shows the AFM result of compact TiO_2 prepared on FTO. The RMS roughness results are shown in table 4.1. The RMS roughness of every sample was around 20 nm. That means the compact TiO_2 film we prepared are very flat. The morphology images indicate that the TiO_2 films prepared under different conditions have only small differences. All the TiO_2 films fully covered the substrate with uniform grain size. Comparing the A, B and C images, A and B films look like some short rods (dumbbell shape) stacking together; the C film shows a small ball shape arranging on the surface. It means that the TiO_2 films prepared under RH=20% and RH=35% were a little more disordered than the film prepared under RH=45%. Even the RMS roughness of the C film was higher than other two films.

To compare the D, E and F films, the E film shows a little more ordered than others. D and F films look like A and B films disordered stacking together. The RMS roughnesses of the films are almost the same. The G, H and I films get a similar result, the H film shows a ball shape arrangement on the surface, the other two films are a little worse than it. The RMS roughnesses are in the same level. A little difference about the RMS results is that the H film is a little smoother than other two. From the preparing conditions of humidity comparison, we know that the ball shape film could be prepared under RH=45% and RH=35% condition.

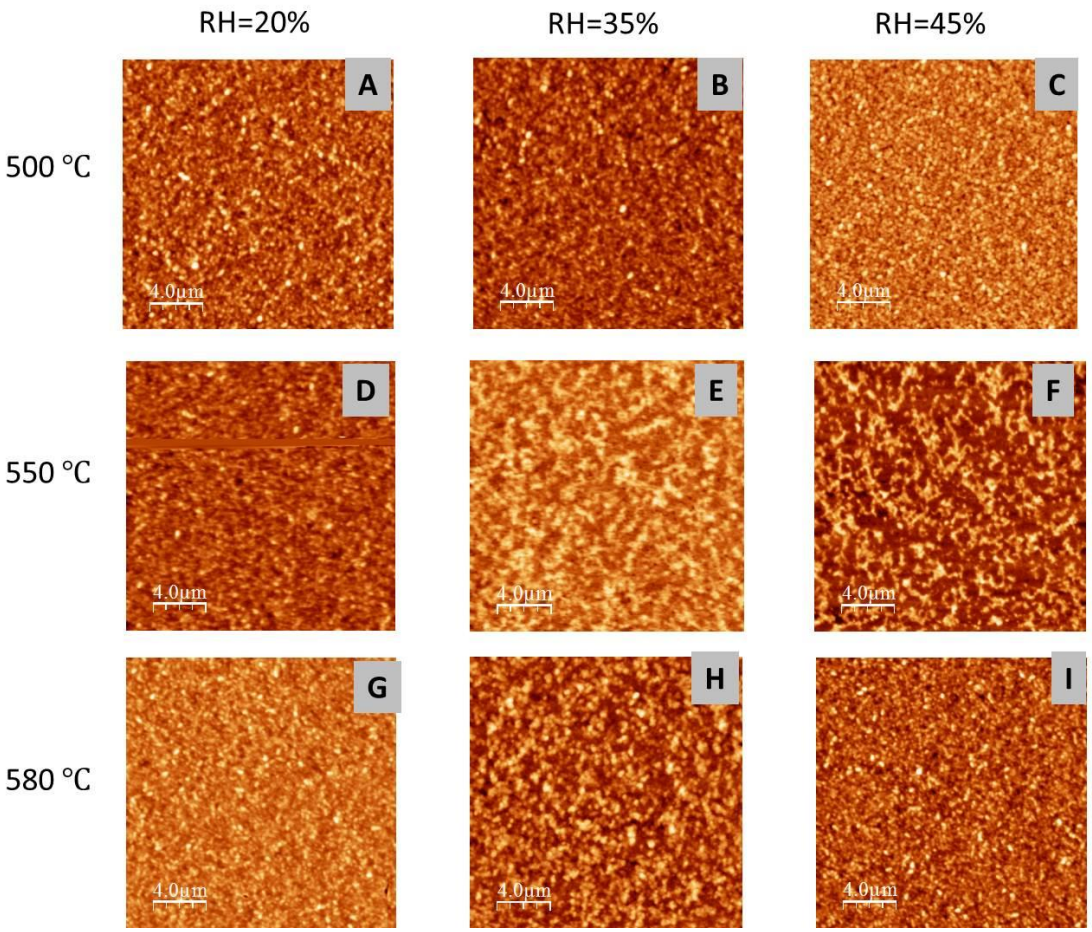

Figure 4.11| AFM measurements of compact TiO_2 films on FTO glass. *The films in the first horizontal row (A, B, C) are sintered at 500 Celsius. In the second (D, E, F) and third (G, H, I) row are sintered at 550 Celsius and 580 Celsius respectively. Corresponding to the sintering temperature, the samples in the left vertical line (A, D, G) are prepared under 20% relative humidity (RH) at room temperature. In the middle (B, E, H) and right vertical line (C, F, I) are prepared under RH=35% and 45% at room temperature, respectively. The TiO_2 precursor was diluted to 0.15M and 0.3M in isopropanol and spin cast at 3000 rpm for 30 seconds in a dry box. Sintered and treated with 0.05 M $TiCl_4$ solution in water.*

To analyse the relationship between the temperature conditions with the TiO_2 morphology, we can conclude that the temperature didn't show a clear effect on the TiO_2 films. Generally, we can get either ball shaped surfaces or rod shaped films under all the temperature we tried. The most important thing is that the reproducible

films require reproducible growth conditions. The TiO_2 precursor spin-casted to FTO glass under RH=35% at room temperature, and sintered at 550 Celsius or 580 Celsius could form a more ordered film. And the precursor spin-casted in RH=20% at room temperature, sintering at 500 Celsius could form a ball shape surface film.

Figure 4.11 shows the AFM measurement results of the perovskite films deposited on top of the TiO_2 layer. All the perovskite films in the picture were prepared by vapour assisted two-step method from spin-casting PbI_2 film and evaporating CH_3NH_3I salt. The substrates were the compact TiO_2 films on FTO glass. The conditions (RH and temperature) appeared in the picture were applied to prepare the corresponding TiO_2 film. Table 4.2 shows the RMS roughness of the perovskite films.

Figure 4.12 shows that the morphologies of all perovskite films are similar. For instance, the G perovskite film shows a full surface coverage, microscale grain size and uniform grain structure. The film suggests its promising applicability for PV devices. These characteristics could be due to the combination of the relative smoothness of the preformed PbI_2 film, the effective intercalation of CH_3NH_3I vapour into the inorganic framework [13, 24 and 25].

Table 4.2| *RMS roughness of the compact TiO_2 films.*

	RH=20%	RH=35%	RH=45%
500 °C	44	38	49
550 °C	50	38	48
580 °C	41	38	42

The perovskites were prepared on compact TiO_2. All the perovskite films were prepared under the same condition. The conditions of RH and temperatures in the table were applied to fabricate compact TiO_2.

The RMS roughness information indicates that the roughness difference among

perovskite films was more significant than on the underlying TiO_2 films. For example, RMS roughness of the perovskite films prepared on RH=35% TiO_2 films were smaller than perovskite films on RH=45% and RH=20% TiO_2 films. On the other hand, the perovskite film on a flat TiO_2 was a little smoother than the perovskite on a less flat TiO_2.

Generally, the RH=35% at room temperature is better than RH=20% and 45% to prepare a smooth TiO_2 film. The smoother TiO_2 substrate will affect the roughness of the perovskite film on top of it.

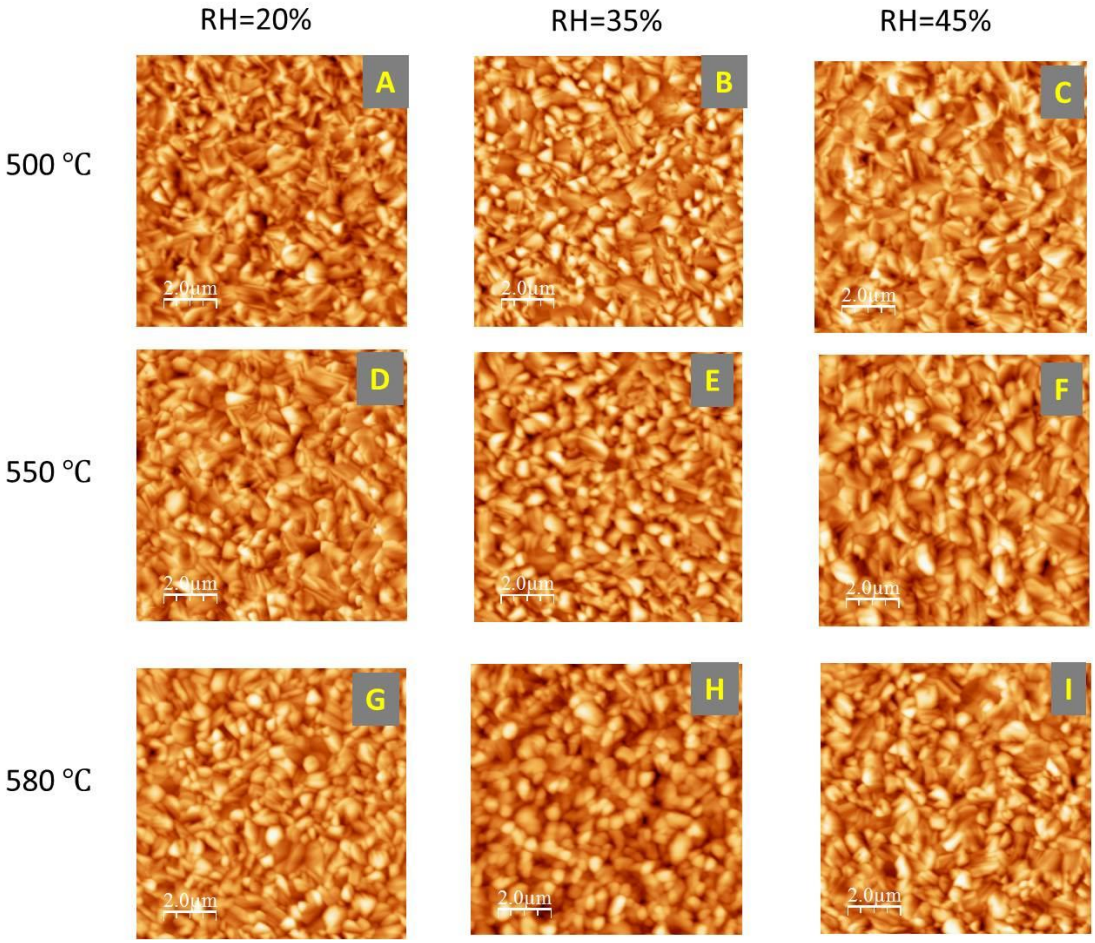

Figure 4.12| AFM measurements of $CH_3NH_3PbI_3$ films on compact TiO_2 films. *The temperature on the left side and the relative humidity on the top are the conditions to prepare the corresponding compact TiO_2 films. The perovskite films were prepared by vapour assisted two-step method.*

4.3.3 Efficiency of the cells with different TiO_2

A variety of performance indicators have been employed by the photovoltaic community to rate the performance of PV cells and modules [26, 27]. The solar cell measurement in our lab is a standard method in the modern research area. The performance of cells and modules can be described by their current versus voltage (I–V) and spectral response versus wavelength (S(λ)) characteristics. Measurement equipment and procedures are discussed for I–V and S(λ). The most common performance indicator is the photovoltaic (PV) efficiency under standard reporting conditions (SRC) (temperature, spectral irradiance, total irradiance). The efficiency (η) is the maximum electrical power (P_{max}) divided by the total irradiance (P_{in}) (Formula 4.2):

$$\eta = \frac{P_{max}}{P_{in}} \times 100\% = \frac{V_{max} \times I_{max}}{P_{in}} \times 100\% \quad (4.2)$$

Where V_{max} and I_{max} are the voltage and current value while power output (P_{out}) arrives to the highest power (P_{max}). Procedures for accurately determining the efficiency or the maximum power with respect to reference conditions are described. At the research level, an internationally accepted set of SRC is essential to prevent the researcher from adjusting the reporting conditions to maximize the efficiency. The procedures for measuring the performance with respect to SRC must be quick, easy, reproducible, and accurate for the research cell fresh out of the deposition system or for the module on a factory floor with production goals. In our lab, we just refer to the reference spectrum as AM1.5G, because the global reference spectrum actually integrates to exactly 1000 W*m^{-2}, and this reference spectrum is popular at modern research level.

The basic definitions to characterize the solar cell are short-circuit current (I_{SC}), open-circuit voltage (V_{OC}), P_{max}, and fill factor (FF), which are introduced as (Formula 4.3 and 4.4):

$$FF = \frac{P_{max}}{V_{oc}I_{sc}} = \frac{V_{max}I_{max}}{V_{oc}I_{sc}} \quad (4.3)$$

$$\eta = \frac{V_{oc}I_{sc}FF}{P_{in}} \quad (4.4)$$

where the short-circuit current (I_{SC}) is the current measured while the voltage between the solar cell electrodes is 0 V. Open-circuit voltage (V_{OC}) is the voltage in the solar cell while the current equals 0 A in the circuit. The fill factor (FF) is defined as the ratio of the maximum power from the solar cell to the product of V_{oc} and I_{sc} (Formula 4.3). These parameters allow the performance under standard reference conditions to be evaluated in an easy way.

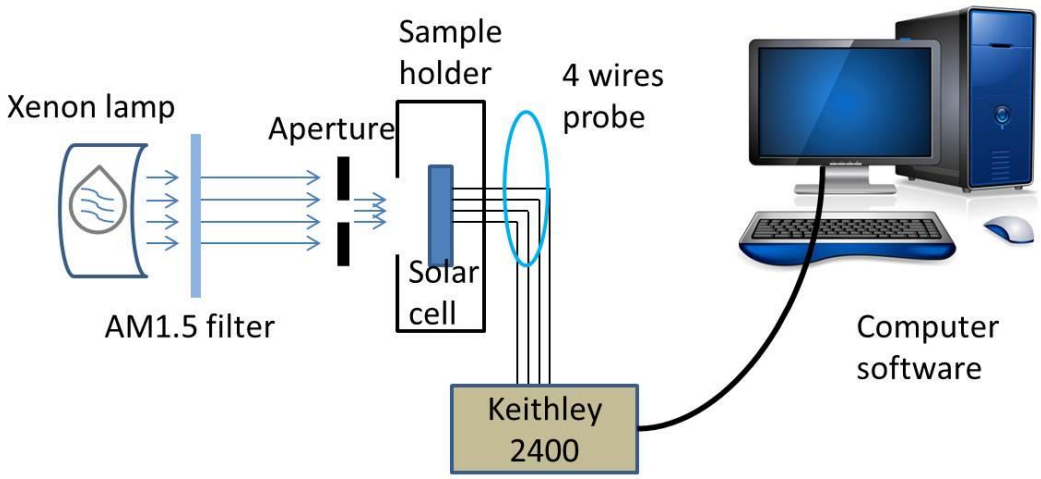

Figure 4.13| Schematic diagram of the solar cell measurement setup. *From left to right, a xenon lamp is placed in front of an AM 1.5 filter. An aperture is used to adjust the size of the light illuminated to the sample holder. 4 wires were connected to a Keithley 2400 source meter which is controlled with computer software.*

The measurement set-up in our lab is sketched in figure 4.13. The system is placed in a dark room with an air conditioner set to 25 Celsius. The light source is a Xenon lamp bought from Newport Company. An optical filter (also from Newport Company) is placed behind the lamp to generate an AM 1.5 spectrum. The light intensity is adjusted by the current output of the lamp driver and by neutral density

filters. An aperture is used to select a uniform waveform. The light area is around 1 cm^2 which is a little larger than solar cell surface area. A small mask for the measurement is placed in the sample holder. The area of the mask is fixed to 0.08 cm^2, which is a little smaller than the solar cell active region (the active area is around 0.09 cm^2). The sample holder has 4 wires connected to one solar cell at the same time to perform a four point probe to remove the effect of probe contact resistance. A Keithley 2400 source meter is used as voltage applier and current meter. The applied voltages were different according to different solar cells. The software would calculate FF and efficiency according to the formulae 4.3 and 4.4.

A two-step deposition technique is used for preparing $CH_3NH_3PbI_3$ perovskite solar cells. Using compact TiO_2 as electron transport layer and blocking layer, P3HT as a hole transport layer, constructing a planar structure, we obtain an efficiency of 7.1% solar cell under AM 1.5 illumination.

The compact TiO_2 is an important electron transport layer in photovoltaic device [28-30]. To investigate the relationship between the compact TiO_2 morphology and the solar cell performance, we construct a planar architecture solar cell. The structure is similar to figure 4.2 B part. In this part, the structure of the solar cell is fixed as FTO/compact TiO_2/$CH_3NH_3PbI_3$/P3HT/(LiF:Ag). The only variance in solar cell is compact TiO_2 was prepared under different conditions. The function of LiF in the solar cell is to modify the interface between the hole transport layer and the metal contact.

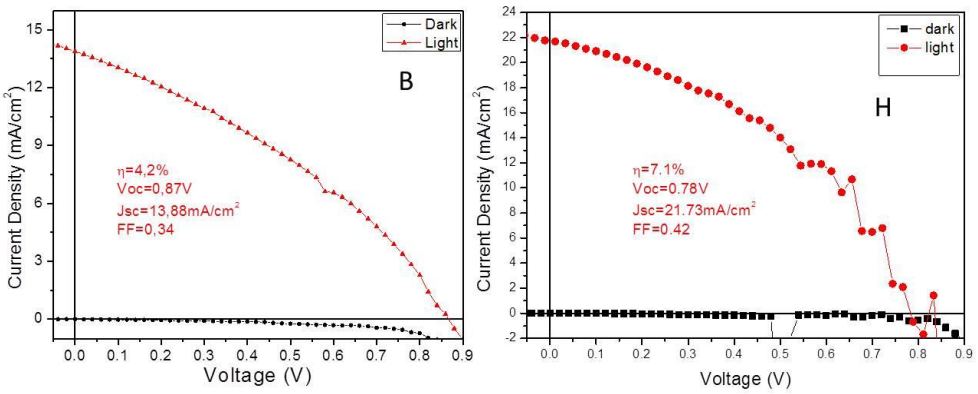

Figure 4.14| Photovoltaic device characterizations. *J–V curves for photovoltaic devices measured at a simulated AM1.5 solar irradiation (red line) and in the dark (black line). The panel B and H are related to the TiO_2 fabricating conditions which are shown in figure 4.11. All the solar cells in the figure have a same structure with* FTO/compact TiO_2/$CH_3NH_3PbI_3$/ P3HT/(LiF:Ag).

Figure 4.14 shows the J-V curves of the solar cells. The measurements were performed at a simulated AM1.5 solar illumination. The solar cells based on ball shape surface arrangement TiO_2 have better performance than solar cells based on disordered TiO_2. The figure shows that the performance of the solar cell under H condition is better than that of the solar cells under B condition.

Panel H in figure 4.14 shows that the power conversion efficiency arrives at 7.1% with the current density of 21.7 mA/cm^2, and panel B shows the efficiency of 4.2%, with the current density of 13.9 mA/cm^2. From these two results, the current density of the H condition is much better than B condition. We can assign it to a better transport property in compact TiO_2 fabricated under H condition, which results in a better PCE performance. The result indicates that the surface with a ball shape arrangement is more suitable than the surface with disordered dumbbell to improve the efficiency performance of the solar cell. Further statistic results are going on in the current works.

4.3.4 Solar cell performance with different modifying material

To investigate the modification layer function in the solar cell, we prepared 3 different type solar cells. First type was based on planar structure FTO/compact TiO_2/$MAPbI_3$/P3HT/ MoO_3/Ag, in which MoO_3 was used as a modification layer. The thickness of the MoO_3 in solar cell was only 5 nm (even less), which would modify the interface between the hole transporting layer P3HT and the metal electrode Ag. Second type was based on FTO/compact TiO_2/$MAPbI_3$/ P3HT/LiF/Ag structure, in which the LiF was utilized as modifying material. The third type was just a reference type without any modification material, to investigate how much can we change by modifying the interface between the electrode and hole transporting layer.

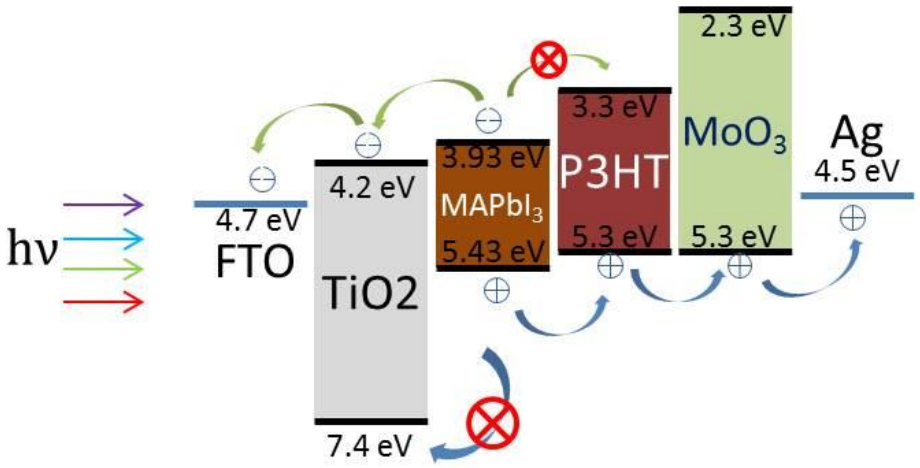

Figure 4.15| Schematic energy diagram of every component in the device. *This solar cell is used MoO_3 as modifying material.*

Figure 4.15 shows the schematic energy diagram of the solar cell with MoO_3 as modifying material. It shows us that the compact TiO_2 is a good electron transporting layer and hole blocking layer, because the conduction band is proper for electrons transporting from perovskite to FTO electrode and the valence band [32] of the TiO_2 is enough to block the holes to diffuse from perovskite toTiO_2. The P3HT is a good hole transporting layer judging from the HOMO of the material. But the LUMO [33] of P3HT is not so high to block the electron to diffuse to the Ag electrode. Hence, he MoO_3 is necessary between the P3HT and the Ag, because the lowest conduction band

[34-36] of the MoO_3 is high enough to block the electrons diffusing to Ag. At the same time, the MoO_3 is a p-type semiconductor, in which the electron cannot transport efficiently. On the other hand, the MoO_3 is a modifying material between the P3HT and Ag, which would decrease the metal work function, resulting a higher ability to transport the hole to the electrode.

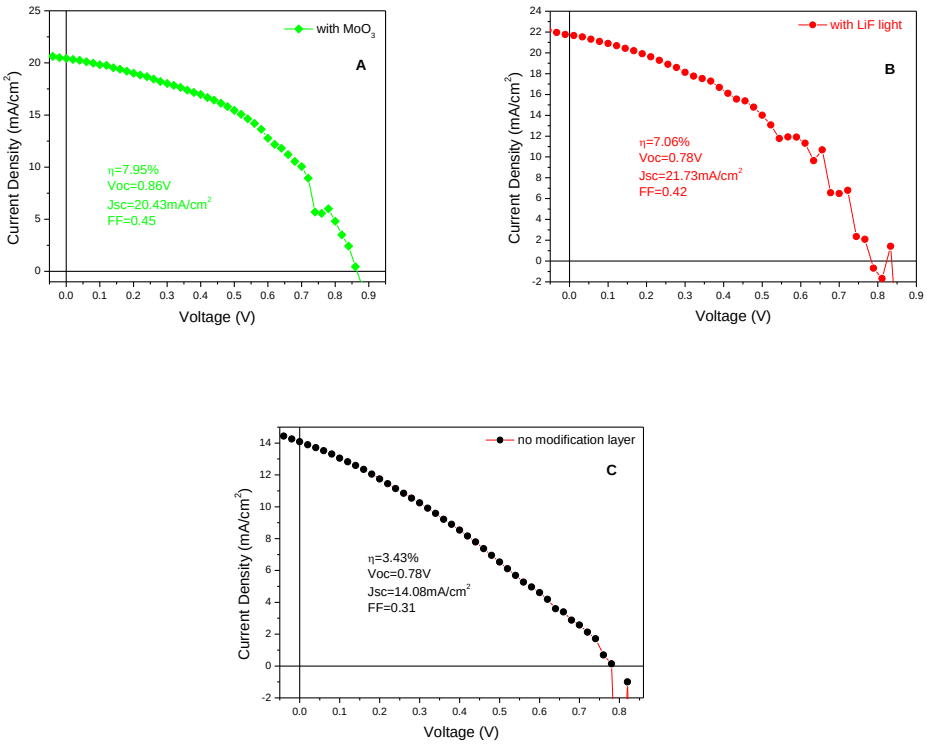

Figure 4.16| J–V characteristics of the perovskite solar cells. A is the *J–V curve of a solar cell with MoO_3. B* is the *J–V curve of a solar cell with LiF. C* is the *J–V curve of a solar cell with no modification material. The basic solar cell structure is fixed as FTO/compact TiO_2/ $MAPbI_3$/P3HT/modification layer /Ag. The measurements were performed under simulated AM 1.5 (100mW/cm^2) sun illumination.*

Similar to the MoO_3, LiF would modify the Ag electrode more effectively than MoO_3. The Ag electrode with LiF would have a lower work function, a little closer to the HOMO of the P3HT, which makes the charge carriers easy to conduct to electrode. And the LiF would modify the compatibility of the P3HT, which makes the metal

electrode contact with hole transport layer efficiently.

Figure 4.16 shows the *J-V* characteristics of the best solar cells under different conditions. Image A shows the *J-V* curve of a solar cell with MoO_3 as modifying material. The best performance shown efficiency (η), open circuit voltage (V_{oc}), short circuit current density (J_{sc}), and fill factor (FF) as 7.95%, 0.86V, 20.43 mA/cm^2 and 0.45, respectively. Figure B shows the *J-V* curve of a solar cell with LiF modification, the best performance of these solar cells shown η, V_{oc}, J_{sc}, and FF as 7.06%, 0.78V, 21.73mA/cm^2 and 0.42, respectively. The solar cells with MoO_3 as modifying material show a better result at efficiency, open circuit voltage and fill factor, but the J_{sc} is worse than another type of solar cell with LiF. And both of the two types of solar cells are better than the solar cell without modification layer in every parameter (η=3.43%, V_{oc}=0.78V, J_{sc}=14.08mA/cm$_2$, FF=0.31). The calculation of serious resistance and the shunt resistance of the solar cell with MoO_3 shows R_s=12.70 Ω and R_{sh}=1239.6Ω, which means we need to do more optimization to get a good solar cell.

4.3.5 Hysteresis in solar cells

As we know that device efficiencies are calculated from current−voltage (J−V) curves, which are usually obtained by measuring under AM 1.5 (100 mW cm^{-2}) irritation. In a common measurement, sweeping the applied bias from short circuit to open circuit (SC-OC) or from the open circuit to short circuit (OC-SC) will give the same behaviour, and the scanning rate will give a negligible effect to the solar cell performance. It indicates that the characteristics of the solar cell are almost irrespective to the sweeping direction and the speed. But the solar cells based on organometal trihalide perovskites are not usual. Kanatzidis et al. [37] reported a ferroelectric response from organometal trihalide perovskites, in which an applied bias dependent slow polarization may occur. Later, hysteresis phenomena in perovskite solar cells were reported [38, 39]. The hysteresis in solar cells is important because it will affect the solar cell performance directly, such as PCE, FF, and Voc.

Figure 4.17 shows the hysteresis property of perovskite solar cell. The

measurements were performed on a planar structure as FTO/CP TiO_2/$MAPbI_3$/P3HT/ MoO_3/Ag.

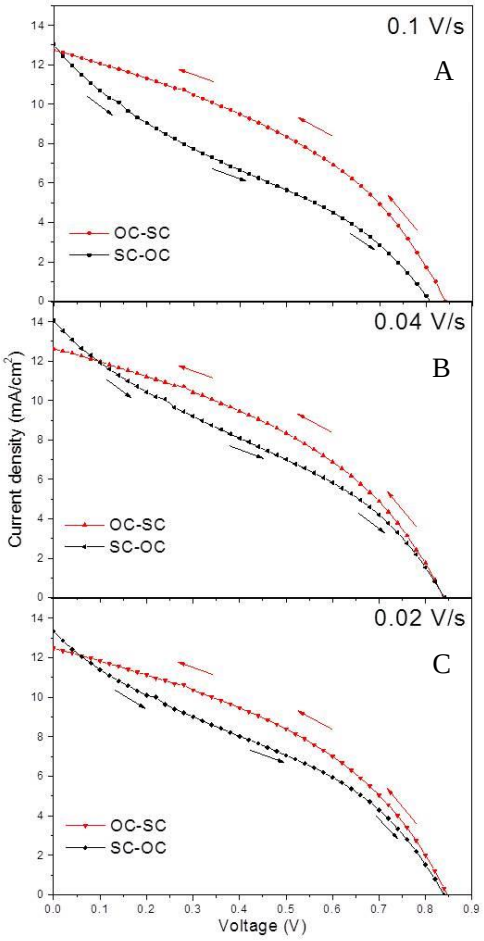

Figure 4.17| *Hysteresis on planar heterojunction perovskite solar cell current-voltage characteristics*. From open circuit to short circuit (OC-SC, red) and from short circuit to open circuit (SC-OC, black) current density−voltage curves for a vapour assisted two-step method processed planar perovskite solar cell measured under simulated AM1.5 (100 mW/cm^2) sun light at a range of scan rates from 0.1 to 0.02 V/s. The interval time between two measurements is 2 minutes.

If the scan rate is 0.1 V/s, it is possible to see significant hysteresis behaviour in the current-voltage curves. From panel A to panel C show the measurements with scan rates from 0.1 to 0.02 V/s. The OC-SC scan from high to low bias voltage showed almost no dependence on scan rate. On the other hand, the efficiency of the SC-OC scan from low to high bias voltage is velocity-dependent. By slowing down the scan rate, hysteresis gradually turns to weaker but will not disappear. The same trend is observed by Dualeh et al. in their work [39], they explained that the phenomenon is from some slow charged carriers involved in the current and voltage generation. The ion drift under electric field in perovskite layer was ascribed to a switchable characteristic in perovskite solar cells by Z. Xiao et al. [40]. In their works, no electron- or hole-transport layer was introduced to the structure, so the ions could drift to either side of the perovskite depending on the electric field applied to the cell, by

which they could get a switchable solar cell. In our case, the compact TiO_2 and P3HT are taken into the solar cells as electron- and hole-transport layer, respectively. Hence, the P-i-N or N-i-P structure will not emerge in our cell, which means we cannot observe a switchable effect from the J-V curve. However, the electric field generated by the bias voltage will affect the polarization property of the perovskite, leading to hysteresis behaviour in the measurement. The poling states would flip to converse direction, while the electric field applied to the solar cell is reversed. The SC-OC scanning should overcome the electric field generated by the solar cell, resulting a lower efficiency at the beginning stage of the measurement.

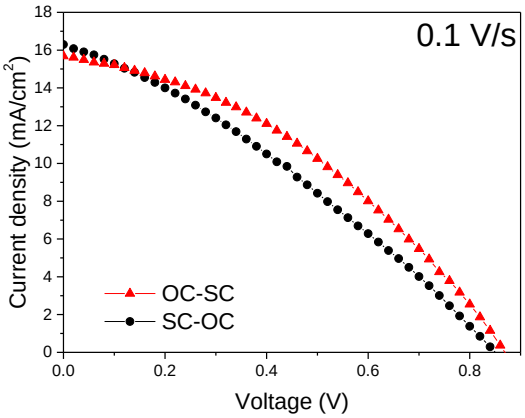

Figure 4.18| *Hysteresis characteristic in a planar structure with LiF as interfacial modifying material. The structure of the solar cell is FTO/CP TiO_2/$MAPbI_3$/P3HT/LiF:Ag. The measurement is performed under AM1.5 sun light simulator. The scan rate is realized by 0.02V scanning step with dwell time of 200ms.*

The similar behaviour is observed in another structure (figure 4.18) in our experiments. To get the "steady-state" efficiency, we need to keep applying the bias voltage around 30 minutes. But a quasi-"steady-state" efficiency could be obtained at 0.01 V/s scan rate.

The two types of solar cells show us the similar strong hysteresis characteristic, indicating the ion drift in the perovskite couldn't be ignored. And the scan rate could be slow enough to get a quasi- "steady state" J-V curve while performing the measurement.

4.3.6 IPCE measurement

The IPCE is an abbreviation of incident photon to charge carrier efficiency of Solar Cells. IPCE could be named quantum efficiency as well. In order to understand the conversion efficiency as a function of the wavelength of light illuminating on the cell, the IPCE measurement is important for materials research and cell design. With this data, the composition and morphology can be modified to optimize conversion over the broadest possible range of wavelengths.

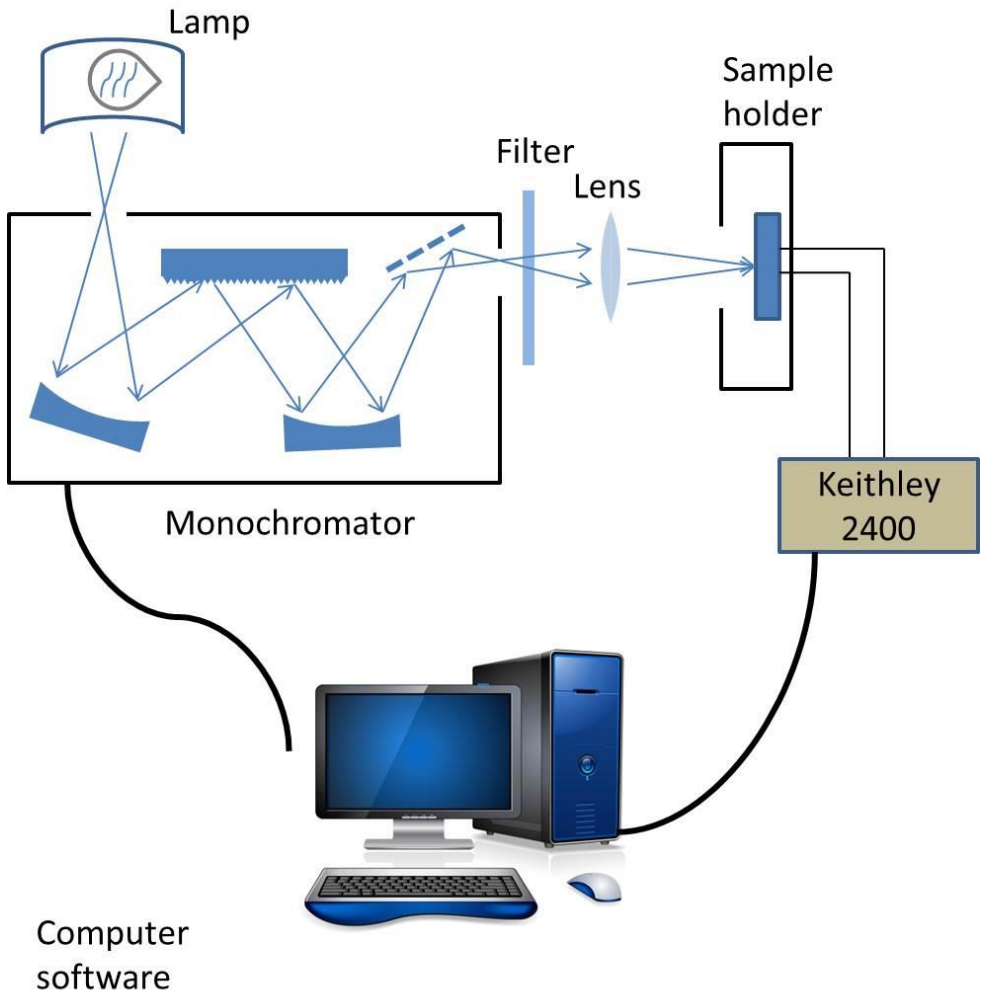

Figure 4.19| The IPCE measuring system. *The light source is a normal white light lamp. A monochromator which is controlled by software generates a single wavelength light to the sample. The data are collected by a Keithley 2400 which is driven by a computer.*

Figure 4.19 shows a schematic diagram of the IPCE measurement. The value of IPCE is the ratio of the number of charge carriers generated by the solar cell to the number of incident photons (Formula 4.5).

$$\text{Quantum efficiency} = \frac{number\ of\ carriers,\ n}{number\ of\ carriers, N} = \Phi \tag{4.5}$$

$$\mathrm{n} = \frac{\mathrm{I} * \Delta\mathrm{t}}{e}$$

$$\mathrm{N} = \frac{(\text{Incident Power, P}) * \Delta\mathrm{t}}{h\nu} = \frac{P * \Delta t}{h\frac{c}{\lambda}} \tag{4.6}$$

In the equation 4.6, the *e* is the fundamental unit of electrical charge. The unit of power P is always watt. The ν is the frequency of the incident light, λ is the wavelength of the incident light.

Substituting the value of n and N in equation 4.5,

$$\Phi = \frac{\frac{I * \Delta t}{e}}{\frac{P * \Delta t}{h\frac{c}{\lambda}}} = \frac{I}{P} \times \frac{hc}{e\lambda} \tag{4.7}$$

In the eq. 4.7, the unit of current I is ampere; the unit of wavelength λ is nm; the unit of light speed in vacuum c is m/s; the Planck constant h is $6.626 \times 10^{-34}\mathrm{J \cdot s}$; the value of e is $1.6 \times 10^{-19}C$.

$$\Phi = \frac{I_{sc}(A)}{P(Watt)} \times \frac{1240}{\lambda(nm)} = \frac{\frac{I_{sc}}{A(cm^2)}}{\frac{P}{A(cm^2)}} \times \frac{1240}{\lambda} = \frac{J_{sc}(mA/cm^2)}{P_A(mW/cm^2)} \times \frac{1240}{\lambda(nm)} \tag{4.8}$$

In the eq. 4.8, A is the area of the solar cell which is always in cm^2 in the measurement. J_{sc} is the short circuit current density. P_A is the power density of the incident light.

$$\text{IPCE}(\%) = \frac{I_{sc}(A)}{P_{\lambda}(W)} \times \frac{1240}{\lambda(nm)} \times 100 \quad (4.9)$$

In the measuring experiment, the parameters need to be recorded are the solar cell area A, the short circuit current $I_{sc}(\lambda)$ along the wavelength λ and incident power P_{λ} along λ. Then IPCE spectrum of the device could be calculated according to eq. 4.9 at different wavelength.

In our measuring system, the light source is just a normal incandescent lamp; the monochromator is from Princeton Instruments, "Acton Spectra Pro Monochromators", which was controlled by computer software and the data were collected by Keithley 2400 at the same time.

Figure 4.20 shows the IPCE spectrum with different wavelength. The measurement was performed in a dark room at room temperature. The IPCE shows a good responsibility to the incident light wavelength from 400-800 nm. To calculate the current density from the IPCE response spectrum, we get the J_{sc}(calculated)=12 mA/cm^2. The J_{sc} we measured was 20.4 mA/cm^2 which is higher than the calculated value from IPCE. Our low J_{sc} value from IPCE may be resulted from: 1) the degradation of the solar cell; and 2) the two-wire measurement took higher contact resistance.

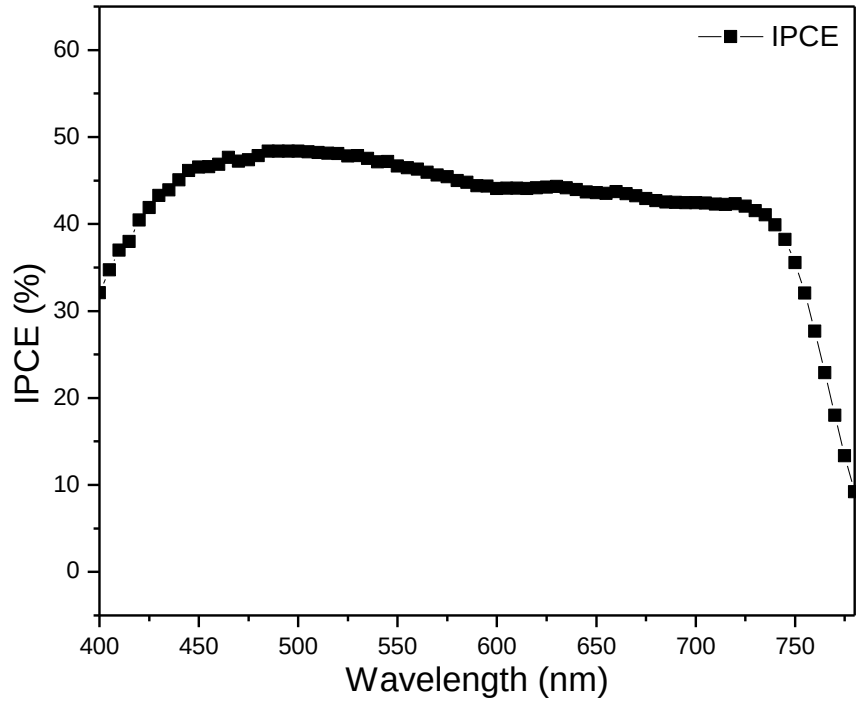

Figure 4.20| *IPCE spectrum of the perovskite solar cell with MoO_3 as modifying material at different wavelength.*

4.4 Conclusion and the prospect

In summary, planar solar cells based on $CH_3NH_3PbI_3$ perovskite have been constructed. The relationship between TiO_2 morphology and the solar cell performance has been discussed. The morphology of compact TiO_2 appear to be an important factor to influence the photovoltaic, which still need further understanding in order to obtain better performing devices. AFM is an old and classic but easy to use and efficient method to investigate the morphology in the material science.

The investigation on perovskite morphology indicates that the vapour assisted two-step deposition technique by spin-casting PbI_2 and evaporating methylammonium salt is useful for preparing perovskite films. The organic and inorganic components have an efficient reaction by vapour intercalating to the PbI_2 film, obtaining a full surface coverage, microscale grain size and uniform grain structure.

The compact TiO_2 prepared under RH=35% and sintered at 580 Celsius (condition G) shows a ball shape arranging surface with a low RMS roughness. The solar cell based on this compact TiO_2 shows a high current density property, which indicates that the morphology of the compact TiO_2 is an important factor to influence the charge transfer in the photovoltaic device.

The investigation on interfacial modification shows that the solar cell with MoO_3 as modification material has excellent performance with a PCE of 7.95%. And the solar cell with LiF as modification material has good performance with a J_{sc} of 21.73 mA/cm^2. Both of the two materials have positive affection to the solar cell. The MoO_3 is a proper material for modifying the interface between the electrode and hole transporting layer, which could replace the ITO in a heterojunction solar cell [36]. And the LiF could decrease the work function of the metal contact, which may increase the transporting ability and increase the compatibility of the metal electrode. The efficiency of the solar cells modified with MoO_3 and LiF increase by 2 times more than without modification solar cell.

The investigation implies that the interface engineering is very important to the device science. The transition metal oxide MoO_3 shows a good result to optimize the performance of the solar cell, we can try to use some other transition metal oxides to modify the interface near the hole transport layer.

Judging from the performance of solar cell with LiF, we are looking forward to the LiF as a promising material to modify the metal electrode in other electronic device.

Reference

[1]. G. E. Eperon, V. M. Burlakov, P. Docampo, A. Goriely, H. J. Snaith, "Morphological Control for High Performance, Solution‐Processed Planar Heterojunction Perovskite Solar Cells", ***Adv. Funct. Mater.*** 2014, 24, 151.

[2]. H. S. Kim, J-K. Lee, N. Yantara, P. P. Boix, S. A. Kulkarni, S. Mhaisalkar, M. Grätzel and N-G. Park, "High Efficiency Solid-State Sensitized Solar Cell-Based on Submicrometer Rutile TiO_2 Nanorod and $CH_3NH_3PbI_3$ Perovskite Sensitizer", ***Nano Lett.*** 2013, 13, 2412.

[3]. P. Docampo, J. M. Ball, M. Darwich, G. E. Eperon and H. J. Snaith "Efficient organometal trihalide perovskite planar-heterojunction solar cells on flexible polymer substrates", ***Nat. Commun.*** 2013, 4, 2761.

[4]. Y. Zhao, A. M. Nardes, and K. Zhu, "Solid-State Mesostructured Perovskite $CH_3NH_3PbI_3$ Solar Cells: Charge Transport, Recombination, and Diffusion Length" ***J. Phys. Chem. Lett.*** 2014, 5, 490.

[5]. S. Sun, T. Salim, N. Mathews, M. Duchamp, C. Boothroyd, G. Xing, T. C. Sumbce, and Y. M. Lam, "The origin of high efficiency in low-temperature solution-processable bilayer organometal halide hybrid solar cells", ***Energy Environ. Sci.*** 2014, 7, 399.

[6]. H. Zhou, Q. Chen, G. Li, S Luo, T-b. Song, H-S. Duan, Z. Hong, J. You, Y. Liu, and Y. Yang "Interface engineering of highly efficient perovskite solar cells", ***Science,*** 2014, 345, 542

[7]. A. Kojima, K. Teshima, Y. Shirai, and T. Miyasaka "Organometal Halide Perovskites as Visible-Light Sensitizers for Photovoltaic Cells", ***J. Am. Chem. Soc.*** 2009, 131,6050.

[8]. H. J. Snaith, "Perovskites: The Emergence of a New Era for Low-Cost, High-Efficiency Solar Cells", ***J. Phys. Chem. Lett.*** 2013, 4, 3623.

[9]. N. J. Jeon, J. H. Noh, W. S. Yang, Y. C. Kim, S. Ryu, J. Seo, and S. Seok, "Compositional engineering of perovskite materials for high-performance solar cells", ***Nature***, 2015, doi:10.1038/nature14133.

[10]. C. R. Kagan, D. B. Mitzi, and C. D. Dimitrakopoulos, "Organic-Inorganic Hybrid Materials as Semiconducting Channels in Thin-Film Field-Effect Transistors", ***Science***, 1999, 286, 945.

[11]. S. D. Stranks, G. E. Eperon, G. Grancini, C. Menelaou, M. J. P. Alcocer, T. Leijtens, L. M. Herz, A. Petrozza, and H. J. Snaith, "Electron-Hole Diffusion Lengths Exceeding 1Micrometer in an Organometal Trihalide Perovskite Absorber", ***Science***, 2013, 342,341.

[12]. M. Liu, M. B. Johnston, and H. J. Snaith, "Efficient planar heterojunction perovskite solar cells by vapour deposition", ***Nature***, 2013, 501, 395.

[13]. J. Burschka, N. Pellet, S. J. Moon, R. H. Baker, P. Gao, M. K. Nazeeruddin, and Michael Grätzel, "Sequential deposition as a route to high-performance perovskite-sensitized solar cells", ***Nature,*** 2013, 499, 316.

[14]. K. Liang, D. B. Mitzi, and M. T. Prikas, "Synthesis and Characterization of Organic-Inorganic Perovskite Thin Films Prepared Using a Versatile Two-Step Dipping Technique", Chem. Mater. 1998, 10, 403.

[15]. Q. Chen, H. Zhou, Z. Hong, S. Luo, H. S. Duan, H. H. Wang, Y. Liu, G. Li, and Y. Yang, "Planar Heterojunction Perovskite Solar Cells via Vapour-Assisted Solution Process", ***J. Am. Chem. Soc.*** 2014,136, 622

[16]. T. Baikie, Y. Fang, J. Kadro, M. Schreyer, F. Wei, S. Mhaisalkar, M. Graetzel, T. White, "Synthesis and Crystal Chemistry of the Hybrid Perovskite $(CH_3NH_3)PbI_3$ for Solid-State Sensitised Solar Cell Applications", ***J. Mater. Chem. A***. 2013, 1, 5628.

[17]. K. T. Lee, S. Y. Lu, "Porous FTO Thin Layers Created with a Facile One-Step Sn^{4+}-Based Anodic Deposition Process and Their Potential Applications in Ion Sensing", ***J. Mater. Chem.*** 2012, 22, 16259.

[18]. W. S. Shin, J. C. Lee,J. R. Kim,H. Y. Lee,S. K. Lee, S. C. Yoon, and S. J. Moon, "Effect of the Alkyl Chain Length of C_{70}-PCBX Acceptors on the Device Performance of P3HT: C_{70}-PCBX Polymer Solar Cells", ***J. Mater. Chem.*** *2011, 21, 960.*

[19]. Y. Yamada, Y. Nakamura, M. Endo, A. Wakamiya, and Y. Kanemitsu,

"Near-band-edge optical responses of solution-processed organic–inorganic hybrid perovskite $CH_3NH_3PbI_3$ on mesoporous TiO_2 electrodes", ***Appl. Phys. Express***, 2014, **7,** 032302.

[20]. M. Saba, M. Cadelano, D. Marongiu, F. Chen, V. Sarritzu, N. Sestu, C. Figus, M. Aresti, R. Piras, A. G. Lehmann, C. Cannas, A. Musinu, F. Quochi, A. Mura, and G. Bongiovanni, "Correlated electron–hole plasma in organometal perovskites", ***Nat. Commun.*** 2014, 5, 5049.

[21]. A. Burke, S. Ito, H. Snaith, U. Bach, J. Kwiatkowski, and M. Grätzel, "The Function of a TiO_2 Compact Layer in Dye-Sensitized Solar Cells Incorporating "Planar" Organic Dyes", ***Nano Lett.*** 2008, *8*, 977.

[22]. H. Yu, S. Zhang, H. Zhao, G. Will, and P. Liu, "An efficient and low-cost TiO_2 compact layer for performance improvement of dye-sensitized solar cells", ***Electrochim. Acta***, 2009, 54, 1319.

[23]. H. F. Wang, L. Y. Chen, W. N. Su, J. C. Chung, and B. J. Hwang, "Effect of the Compact TiO_2 Layer on Charge Transfer between N3 Dyes and TiO_2 Investigated by Raman Spectroscopy", ***J. Phys. Chem. C***, 2010, 114, 3185

[24]. D. Bi, A. M. El-Zohry, A. Hagfeldt, and G. Boschloo, "Improved Morphology Control Using a Modified Two-Step Method for Efficient Perovskite Solar Cells", ***Appl. Mater. Interfaces,*** 2014, 6, 18751.

[25]. D. Bi, S. J. Moon, L. Haggman, G. Boschloo, L. Yang, E. M. J. Johansson, M. K. Nazeeruddin, M Grätzel, and A. Hagfeldt, "Using a two-step deposition technique to prepare perovskite ($CH_3NH_3PbI_3$) for thin film solar cells based on ZrO_2 and TiO_2 mesostructures", ***RSC Advances,*** 2013, 3, 18762.

[26]. K. A. Emery, and C. R. Osterwald, "Solar cell efficiency measurements", ***Sol. Cells***, 1986, 17, 253.

[27]. S. Nann, and K. Emery, "Spectral effects on PV-device rating", ***Sol. Energy Mater. Sol. Cells***, 1992, 27, 189.

[28]. J. Burschka, A. Dualeh, F. Kessler, E. Baranoff, N. L. Cevey-ha, C. Yi, M. K. Nazeereddin, and M. Grätzel, "Tris(2-(1H-pyrazol-1-yl)pyridine)cobalt(III) as p-type dopant for organic semiconductors and its application in highly efficient

solid-state dyesensitized solar cells", ***J. Am. Chem. Soc.*** 2011, 133, 18042.

[29]. S. R. Jang, K. Zhu, M. J. Ko, K. Kim, C. Kim, N. G. Park, and A. J. Frank, "Voltage- enhancement mechanisms of an organic dye in high open-circuit voltage solid-state dye-sensitized solar cells", ***ACS Nano,*** *2011,* 5, 8267.

[30]. I. Chung, B. Lee, J. He, R. P. H. Chang, and M. G. Kanatzidis, "All-solid-state dye sensitized solar cells with high efficiency", ***Nature***, 2012, 485, 486.

[31]. G. Xing, N. Mathews, S. Sun, S.S. Lim, Y.M. Lam, M. Grätzel, S. Mhaisalkar, T.C. Sum, "Long-Range Balanced Electron- and Hole-Transport Lengths in Organic-Inorganic $CH_3NH_3PbI_3$", ***Science***. 2013, 342, 344.

[32]. J.-H. Huang, H.-Y. Wei, K.-C. Huang, C.-L. Chen, R.-R. Wang, F.-C. Chen, K.-C. Ho, C.-W. Chu, "Using a Low Temperature Crystallization Process to Prepare Anatase TiO_2 Buffer Layers for Air-Stable Inverted Polymer Solar Cells", ***Energy Environ. Sci.*** 2010, 3, 654.

[33]. Y. Sun, M. Wang, X. Gong, J. H. Seo, B. B. Y. Hsu, F. Wudlab and A. J. Heeger, "Polymer Bulk Heterojunction Solar Cells: Function and Utility of Inserting a Hole Transport and Electron Blocking Layer into the Device Structure", ***J. Mater. Chem.*** 2011, 21, 1365

[34]. J. Ajuria, I. Etxebarria, W. Cambarau, U. Munecas, R. Tena-Zaera, J. C. Jimenoc and R. Pacios "Inverted ITO-Free Organic Solar Cells Based on P and N Semiconducting Oxides. New Designs for Integration in Tandem Cells, Top or Bottom Detecting Devices, and photovoltaic windows", ***Energy Environ. Sci.*** 2011, 4, 453.

[35]. C. Girotto, E. Voroshazi, D. Cheyns, "Solution-Processed MoO_3 Thin Films as a Hole-Injection Layer for Organic Solar Cells", ***ACS Appl. Mater. Interfaces***, 2011, 3, 3244.

[36]. J. Yang, J. You, C.C. Chen, W.C. Hsu, H. Tan, X.W. Zhang, "Plasmonic Polymer Tandem Solar Cell", ***ACS nano,*** 2011, 5, 6210.

[37]. C. C. Stoumpos, C. D. Malliakas and M. G. Kanatzidis, "Semiconducting Tin and Lead Iodide Perovskites with Organic Cations: phase Transitions, High

Mobilities, and Near-Infrared Photoluminescent Properties", ***Inorg. Chem.*** 2013, 52, 9019.

[38]. H. J. Snaith, A. Abate, J. Ball, G. E. Eperon, T. Leijtens, N. K. Noel, S. D. Stranks, J. Tse-Wei Wang, K. Wojciechowski, and W. Zhan, "Anomalous Hysteresis in Perovskite Solar Cells", ***J. Phys. Chem. Lett.*** 2014, 5, 1511.

[39]. A. Dualeh, T. Moehl, N. Tetreault, J. Teuscher, P. Gao, M. K. Nazeeruddin, and M. Gratzel, "Impedance Spectroscopic Analysis of Lead Iodide Perovskite-Sensitized Solid-State Solar Cells", ***ACS Nano,*** 2014, 8, 362.

[40]. Z. Xiao, Y. Yuan, Y. Shao, Q. Wang, Q. Dong, C. Bi, P. Sharma, A. Gruverman, and J. Huang, "Giant switchable photovoltaic effect in organometal trihalide perovskite devices", ***Nature Materials,*** 2015, 14, 193.

CHAPTER 5
Conclusions

Solar energy is considered as one of the most promising techniques to meet the continuously increasing energy requirement. Although the conventional solar cells have high power conversion efficiency, the high-performance solar cells rely on semiconductors that must be grown at high temperatures in expensive fabrication facilities. Not so with organometal halide perovskites. The achievements obtained in the past 6 years push the perovskite towards being utilized in industry rapidly. Organic-inorganic hybrid perovskites which combine the properties of organic and inorganic semiconductors are hopeful candidates for future optoelectronic devices, not only for solar cells. The high absorption coefficient, tunable bandgap, high mobility and long range diffusion length are all very desirable properties. On the other hand, as "relatively" new materials, more research work is necessary to understand all the behaviours of perovskites. In this thesis, the main aim of this research work concerns the study of the optical properties of perovskites and the increase the PCE performance by interface engineering.

In the course of this thesis, the synthesis route of the methylammonium iodide (MAI) and methylammonium bromide (MABr) was developed. The Pb is chosen as the B-site metal element in the perovskite structure of ABX_3. $PbCl_2$, PbI_2 and $PbBr_2$ were used as precursors to synthesize pure halide perovskite $CH_3NH_3PbX_3$ (X=I, Br) or mix-halide perovskites $CH_3NH_3PbI_{3-x}Cl_x$ ($0< x <1$). The structure of the perovskites has been confirmed by XRD investigation. The XRD patterns results show that $CH_3NH_3PbI_{3-x}Cl_x$ has at most a negligible amount of chlorine and a $CH_3NH_3PbI_3$-like structure; $CH_3NH_3PbI_3$ shows a tetragonal structure with lattice parameters a=b=8.872 Å and c =12.637 Å. The XRD analysis to $CH_3NH_3PbBr_3$ shows that it has a cubic phase in film and the growth orientation in the (101) and (240) directions are dominant.

The quality of the $CH_3NH_3PbI_3$ films, which are prepared from simple solution

processing, two-step solution spin-casting and vapour assisted two-step solution spin-casting, have been investigated. The AFM measurements showed that solution spin-casting method produces needle-shaped crystals, leading to a partial surface coverage and limited conductivity, not the best morphology for a planar solar cell. The two-step from solution method was based on spin casting a PbI_2 film first, then spin cast a CH_3NH_3I solution on top of the PbI_2 layer, creating the perovskite upon reaction of the two compounds. The result is a film with smaller grains and more uniform coverage. Finally, the vapour assisted method, where a PbI_2 film is first spin-cast from solution, then evaporation of CH_3NH_3I occurs for several hours in N_2 atmosphere to form the perovskite. The efficiency of the solar cell from the vapour assisted method can exceed 7%. Within the vapour assisted method we study how different PbI_2 solution temperatures affect the final perovskite film morphology. We used standard 70℃ PbI_2 solution and different intermediate temperature until we reached a metastable room temperature transparent solution. With the room temperature PbI_2 deposition we can achieve a perovskite film with a RMS roughness lower than 25 nm with a very low pin-hole density that can improve the cell efficiency within the planar architecture.

The optical properties of the $CH_3NH_3PbI_3$ demonstrate a bandgap of it is 1.64 eV calculated from the absorption edge. The absorption coefficient exceeds ~10^5 cm^{-1} for incident wavelengths shorter than 500 nm. The transient photoluminescence spectroscopy analysis show that the lifetime of the excitons could be as high as τ= 80 ns under low excitation conditions. As long as the film is processed in such a way that the mean PL lifetime exceeds several nanoseconds at sun illumination, carrier mobility is sufficiently high to guarantee efficient charge collection in the photovoltaic device.

The solar cell performance in a planar structure is investigated. The planar solar cells based on $CH_3NH_3PbI_3$ perovskite have been constructed. The relationship between TiO_2 morphology and the solar cell performance has been discussed. The morphology of compact TiO_2 appears to be an important factor to influence the photovoltaic, which still needs further understanding in order to obtain better

performing devices.

The investigation on perovskite morphology indicates that the vapour assisted two-step deposition technique by spin-casting PbI_2 and evaporating methylammonium salt is useful for preparing perovskite films. The organic and inorganic components have an efficient reaction by vapour intercalating to the PbI_2 film, obtaining a full surface coverage, microscale grain size and uniform grain structure.

The compact TiO_2 prepared under RH=35% and sintered at 580 Celsius (condition G) shows a ball shape arranging surface with a low RMS roughness. The solar cell based on this compact TiO_2 shows a high current density property, which indicates that the morphology of the compact TiO_2 is an important factor to influence the charge transfer in the photovoltaic device.

The investigation on interfacial modification shows that the solar cell with MoO_3 as modification material has excellent performance with a PCE of 7.95%. And the solar cell with LiF as modification material has good performance with a J_{sc} of 21.73 mA/cm^2. Both of the two materials have positive effect to the solar cell. The MoO_3 is a proper material for modifying the interface between the electrode and hole transporting layer, which could replace the ITO in a heterojunction solar cell. And the LiF could decrease the work function of the metal contact, which may increase the transporting ability and increase the compatibility of the metal electrode. The efficiency of the solar cells modified with MoO_3 and LiF increase by 2 times more than without modification solar cell. The investigation implies that the interface engineering is very important to the device science.

Acknowledgement

I would like to express my appreciation to Prof. Michele Saba, for his kindly help during these 3 years, for the scientific discussions as well as in the life, and for giving me the opportunity to work with him even I made mistakes. And especially for the key guiding suggestion when nothing was working. I wish thank Prof. Giovanni Bongiovanni and Prof. Andrea Mura for giving me much useful guidance for the method and instruments to scientific work. I would thank Dr. Francesco Quochi for his helpful discussion in my work.

I would love to thank Dr. Daniela Marongiu for her help in the experiments and sharing the unpublished results. And thank Roberto Piras for his help for the synthesizing discussion and the advices to the reacting equipment. A special thanks to Michele Cadelano, Nicola Sestu and Valerio Sarritzu for their help on photophysical properties measurements and the discussion. And thank Dr. Cristiana Figus and Dr. Mauro Aresti for their help and discussion.

I am grateful for the equipment assistance provided by Dr. Guido Mula and Prof. Alessandra Geddo Lehmann.

I would also like to extend my thanks to the technicians of the department for their help in offering me the masks and the sample holders, and fixing the equipment used in my experiment.

I would like to acknowledge Ministero dell'Istruzione, dell'Università e della Ricerca for financial support.

Finally, I wish to thank my families for their support and encouragement throughout my study.